IEEE control systems MAGAZINE

JUNE 2012 VOLUME 32 NUMBER 3

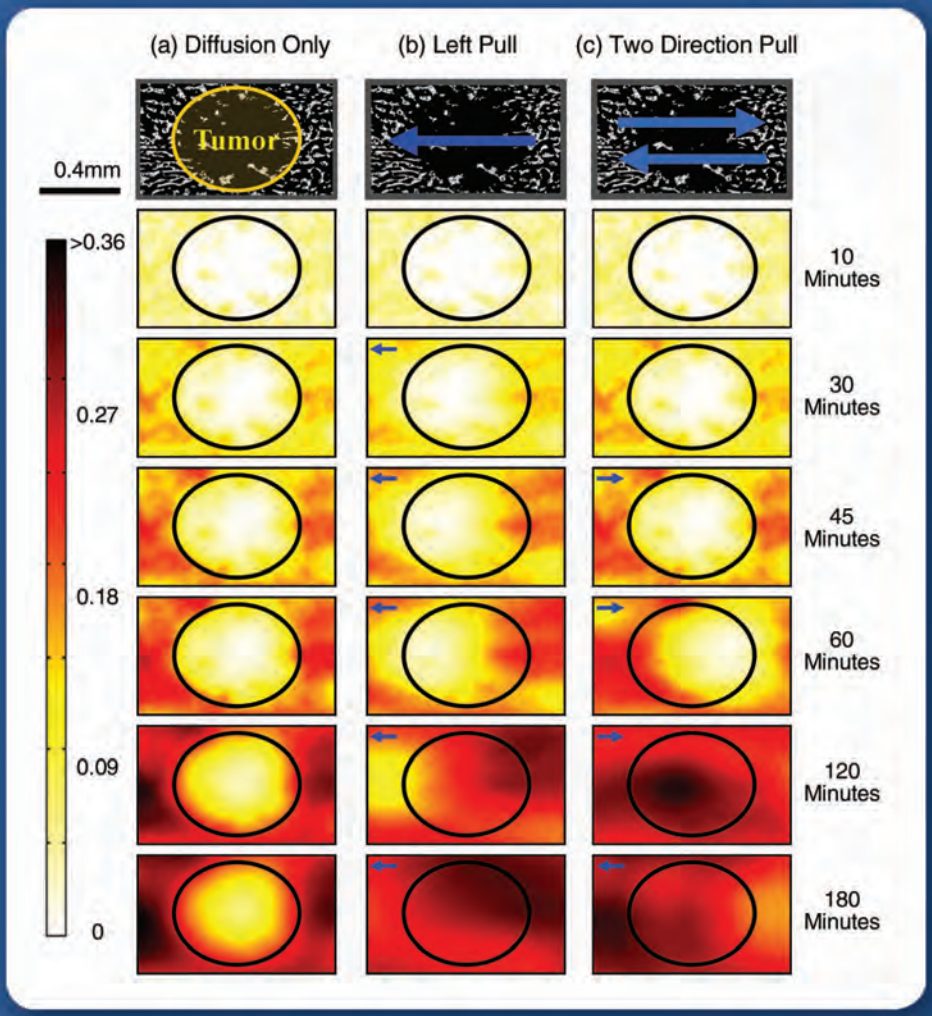

Magnetic Chemotherapy

CSS
Control Systems Society
Advancing Control Science and Technology

IEEE

Towards Control of Magnetic Fluids in Patients

DIRECTING THERAPEUTIC NANOPARTICLES TO DISEASE LOCATIONS

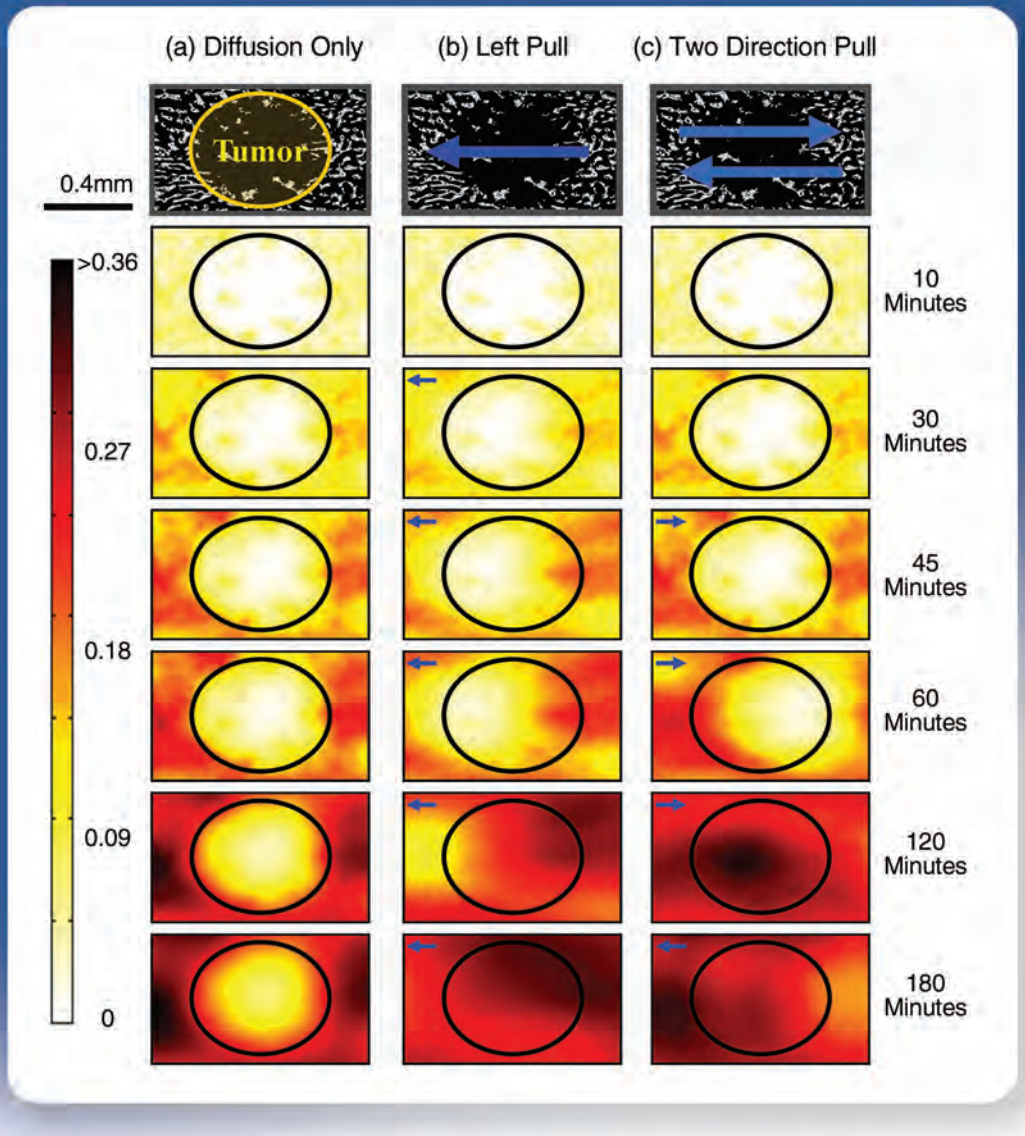

ALEKSANDER NACEV, ROLAND PROBST, SKYE H. KIM, ARASH KOMAEE, AZEEM SARWAR, ROGER LEE, DIDIER DEPIREUX, MICHAEL EMMERT-BUCK, and BENJAMIN SHAPIRO

Digital Object Identifier 10.1109/MCS.2012.2189052
Date of publication: 16 May 2012

A tremendous need exists to be able to focus medicine to disease locations. During chemotherapy, for example, typically less than 0.1% of the drugs are taken up by tumor cells, with the remaining 99.9% going into healthy tissue [1]. Chemotherapy encompasses treating patients with a diverse collection of drugs that attempt to preferentially destroy cancer cells either by inhibiting cellular division (which kills fast growing cancers but also bone marrow, hair, skin, gut, and immune system cells) or by interrupting essential cell signaling pathways [2]–[7]. Physicians often combine drugs into chemotherapy cocktails that can compound side effects, and the dosage is usually selected by how much a patient can physically withstand rather than by how much is needed to kill all the tumor cells [2], [8], [9]. The ability to actively position medicine, to physically direct and focus it to specific locations in the body, would allow better treatment of not only cancer but many other diseases.

Magnetic drug targeting offers a potential solution. It refers to physical manipulation of medicine inside the body by magnetic fields (Figure 1). The medicine is made magnetic by linking it to nanoscopic magnetic carriers [10]–[25]. After injection of such therapeutic magnetic carriers into the patient's body, external magnets can then be used to direct the therapy to sites of disease—to tumors [11], [22], [26], [27], blood clots [10], or infections [28], [29]. This physical focusing of treatment to needed locations can improve efficacy while reducing systemic drug concentrations, thus limiting unpleasant or potentially deadly side effects in the rest of the body.

Magnetic fields—more so than light, electric fields, and ultrasound [42]–[46]—are desirable for directing therapeutics inside patients because they can penetrate deep into the body, are routinely applied through the body in magnetic resonance imaging (MRI), and are considered safe even up to very high strengths (8 T in adults, 4 T in children) [30], [47]–[49]. Magnetic fields can both sense and actuate magnetic particles, although achieving both at once is an engineering challenge [50]–[52]. In contrast, light and ultrasound have limited tissue penetration depths [42], [53], [54], while strong electric fields would electrocute patients [48], [55].

Therapeutic magnetic elements have been created by the attachment of chemotherapy [2], [9] or gene therapy [56]–[58] to ferromagnetic particles [17], [23], [24], [59]–[64], by filling polymer capsules or micelles (capsules that self-assemble from lipid molecules [65]) with both drugs and magnetic materials [64], [66], or by growing cells in a cell-culture medium with magnetic nanoparticles to let the cells ingest the particles and thereby become magnetic [67], [68]. A bare iron oxide nanoparticle is the simplest example of a magnetic carrier [69]. Magnetic particles can also consist of magnetite (Fe_3O_4) or maghemite (Fe_2O_3) nanocrystals embedded in a polymer core and are usually coated with a layer of molecules (often starch or polyethylene glycol (PEG) molecules) to make the particles more biocompatible [23], [64], [66], [70]. In more sophisticated particles, this coating is carefully optimized to better hide the particles from the human immune system so that the particles have a longer circulation time in the body before they are removed to the liver, kidneys, and spleen [64], [71]. Particle sizes can be controlled by various fabrication processes [23], [64], [72] and are made from nanometer to micrometer sizes. They are usually injected into an animal or a patient as a ferrofluid, which is an emulsion of magnetic particles in water. Such magnetic nanoparticles have been tested in animals [17], [24], [37] and humans [13], [22], [73], [74]. Other entities besides particles—such as polymer capsules [75], flexible rods [76], lipid micelles [77]–[79], and live cells (such as stem cells) [67], [68]—can also be loaded with magnetic materials and thus made magnetic. Stem cells are being magnetized so that they can be directed to regions of cardiovascular disease, such as hardened blood vessels in diabetic patients, to help restore tissue function [68], [80], [81]. All of these magnetized carriers, from nanoparticles to

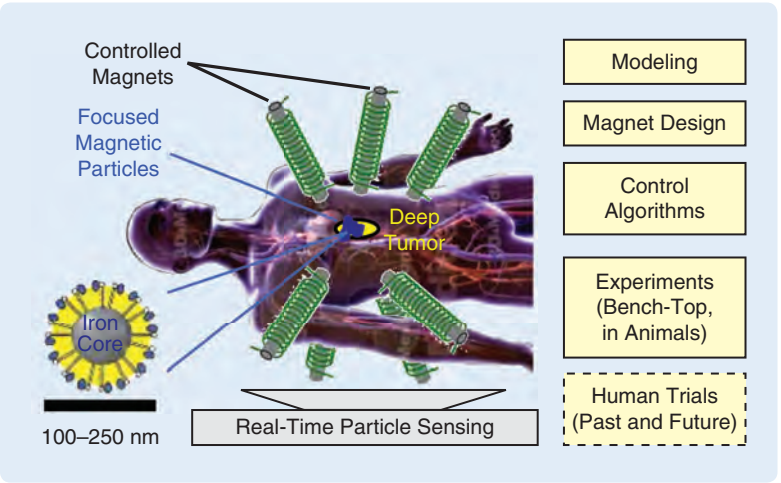

FIGURE 1 The goal is to design and control magnets to direct magnetic therapy to disease locations, for example, to a deep tissue tumor such as this one. The article discusses topics that include the modeling of magnetic fields, forces, and the resulting nanoparticle transport in-vivo (inside the body); magnet designs; open and closed-loop control; equipment; animal experiments; and prior human clinical trials. Deep and real-time imaging of magnetic nanoparticles is an emerging area and could be accomplished by advances in fast magnetic resonance imaging (MRI) [30]–[32], positron emission tomography (PET) scanning [33] with fast gamma imaging [34], [35], or magnetic particle imaging (MPI) that exploits the nonlinear saturation response of ferromagnetic particles to strong magnetic fields [36]–[41]. The conclusion of this article notes future steps required to move the results from research to patients. (The blue anatomical figure showing the major human blood vessels in red and purple was taken from 3D4Medical software and is reproduced with permission.)

cells, can then be manipulated inside the body by externally applied magnetic fields. It takes a lot of development to ensure that magnetic carriers are safe, effective, and therapeutic [64]. Due to stringent regulatory approval requirements, so far only a few magnetic carriers (four total) have been commercialized and approved for human use, and not yet as therapeutic carriers but only as imaging agents [82]–[85].

During magnetic drug targeting, magnetic carriers must be safely and effectively controlled inside the human body. The body consists of a heterogenous and complex environment, which varies widely from person to person, and is not well understood. Many relevant and significant issues for effective control of particles remain unanswered, including uncertainty about the mechanisms of ferrofluid transport within the body, how nanoparticles can or cannot cross blood vessel walls, and how much force is required to direct them from blood into tissue. Similarly, there is a lack of knowledge of basic internal body parameters. The location of most blood vessels, the blood flow velocities in each vessel, the resistance of different tissue types to particle motion, and many other biological parameters are not known in general or for the case of each specific patient. Yet even though the situation is highly uncertain, prior magnetic drug delivery has already been shown to effectively focus therapy to some desired locations in animals and humans. For example, in the Lübbe 1996 phase I human clinical trials, a single permanent magnet was able to concentrate chemotherapy to inoperable but shallow ($\leq$5 cm below skin depth) head, neck, and breast cancer tumors [13], [86], [87].

The depth, precision, and utility of magnetic targeting has been limited by particle material and surface properties [23], [64], by an insufficient understanding of particle transport in the human body [12], [88]–[93], by the strength and design of magnets [47], [94]–[96], by a lack of deep-body real-time nanoparticle sensing capabilities [37], and by control algorithm development and implementation [91], [97]–[102]. Magnetic nanoparticle fabrication and the resulting material and surface properties have been surveyed [17], [23], [62]–[64], [70]. Essentially, material magnetization susceptibility properties, χ, set the strength of the magnetic forces for a given particle size and applied magnetic field [16], [69], [76], [103], [104], whereas surface coatings, particle size, and particle shape regulate biocompatibility and particle circulation times [17], [23], [64]. Modeling magnetic particle transport inside the body (in-vivo) has ranged from simple back-of-the-envelope estimates [105]–[107], to initial formulation of governing partial differential equations [89], [108], to recent numerical efforts to quantify particle motion due to diffusion, blood convection, and extravasation (that is, the ability of nanoparticles to pass through blood vessel walls into surrounding tissue) [21], [88], [93], [109]–[112]. Real-time and sensitive measurement of nanoparticle distributions in-vivo is challenging [14], [22], [23], even in small animals where depth of imaging is less of an issue [113]–[115], and has made it difficult to collect sufficient data to adequately validate models.

Magnetic nanoparticles are small and experience small forces even under strong magnetic fields. In prior magnetic drug delivery experiments, magnet strengths have ranged from 70 mT [16] to 2.2 T [116], and corresponding magnetic gradients have varied from 0.03 T/m [117] to 100 T/m [118], a range that reflects magnet cost, complexity, safety, and ease-of-use versus desired (or possible) depth of targeting. For comparison, modern neodymium-iron-boron ($Nd_{12}Fe_{14}B$) permanent magnets can be purchased in strengths of up to 1.48 T [119], [120] and the electromagnets used in MRI systems create fields of 1–4.7 T, with some commercially available MRI systems going as high as 9.4 T [37], [47]. In the 1996 human trials, 0.2–0.8 T permanent magnets were used to target 100-nm diameter particles to 5-cm depths [11], [86]. Targeting depths of up to 12 cm have been reported in animal experiments using larger 500-nm to 5-μm diameter particles and a 0.5-T permanent magnet [121]. Both permanent and electromagnet designs can be optimized to extend magnetic fields and gradients further out, to increase the depth of magnetic forces. Magnet optimization for depth and strength of forces is not discussed here but is addressed elsewhere [116], [118], [122]–[125].

Precision magnetic control of a single object has been demonstrated in animals and humans. Gentle magnetic manipulation of a rigid implanted permanent magnet through the brain, with a view to scan and burn out brain tumors by subsequently heating the magnet using RF (radio frequency) magnetic fields, has been presented [126], [128] and tested in dogs [129]. Based on market opportunities, the focus of this effort changed to magnetically assisted cardiovascular surgical procedures and led to the formation of Stereotaxis (www.stereotaxis.com). This company now uses magnetic control to guide catheters, endoscopes, and other surgical tools with magnetic tips for precision treatment of cardiac arrhythmias and other cardiovascular procedures [130]–[135] [Figure 2(a)]. To date, Stereotaxis has carried out over 40,000 successful patient procedures in nearly 200 facilities around the world. Systems to magnetically steer implantable devices and micro robots, for gut, eye, cardiac, endovasculature, and lung surgery [136]–[143], have been tested in pigs and chicken embryos [144]–[147]. Conventional MRI machines have also been used as the actuation system to manipulate microscale particles [137], [148]–[152] as well as magnetotactic bacteria [99], [153] or magnetized cells [81], [154]–[157], in pigs and mice [149], [154]. While MRIs are attractive due to their magnetic strength and clinical availability, the difficulty is that MRIs are designed to create a strong uniform magnetic field, but spatially varying magnetic fields are required to create forces on particles. Unless the MRIs are substantially modified [158]–[160], they do not create sufficient magnetic spatial gradients to effectively manipulate nanoscopic

particles. The control algorithms used in the above single-object manipulation systems have ranged from proportional-integral-differential (PID) control [137], [146] to point-wise optimization [126], [128], least-squares inversion [161], robust nonlinearization with backstepping [151], [162], a generalized predictive controller [150], and model predictive control [163].

Precise manipulation of a fluid of nanoparticles is more difficult than control of a single object. In prior ferrofluid trials, a magnet held outside the body drew in and concentrated particles to shallow breast, head and neck, and brain tumors [11], [27], [73], [86], [105], [107], [164]–[177] [Figure 2(b)]. There was no dynamic magnet control, and the magnets accumulated the particles to targets beneath the skin or skull. Implantation of magnets or magnetic material into patients, such as within blood vessel walls, has been suggested as a way of reaching deeper tissue [178]–[189]. The implanted materials serve to locally increase magnetic field gradients, and thus forces, when an external magnetic field is applied. Such a treatment has been envisioned to bring magnetized endothelial cells to blood vessel walls and could also be appropriate for treating tumors that cannot be surgically removed but when magnetizable implants can be inserted into or near the tumor [178]–[181], [187], [190]. Overall, although the field of magnetic drug targeting is advancing toward commercial particles approved for human use [22], [80], [82]–[85], it remains open for significant improvements in modeling, design, and control, especially for noninvasive methods to effectively target deeper tissue. To show how different clinical needs suggest different engineering solutions, this article focuses on two examples: 1) reaching inner ear diseases and 2) better treatment of deep-tissue tumors.

The article begins with modeling magnetic fields and forces on nanoparticles and shows how this can reveal a method for particle pushing, which is a capability that allows magnetic injection of therapy into the inner ear [191] that has been validated in rat experiments [192]. The magnet design for this case is simple, requiring just two magnets that are correctly oriented, and does not require dynamic magnetic fields, particle sensing, or feedback control. Next, modeling the magnetic fields and forces enables dynamic optimal (minimum magnetic power) and robust closed-loop steering of a single drop of ferrofluid in bench-top experiments [100], [193]. These experiments already encapsulate some key features of magnetic drug control (such as electromagnet dynamics, a quadratic mapping from magnet actuation to ferrofluid motion, and the discontinuous nature of optimal solutions) but lack other features that will be required for ferrofluid control in patients (most importantly, the manipulation of a distributed ferrofluid instead of controlling a single droplet and precise control inside a living organism instead of in a petri dish). Indeed, feedback control of ferrofluid inside the body is far more complex than in a petri dish and first requires a better understanding

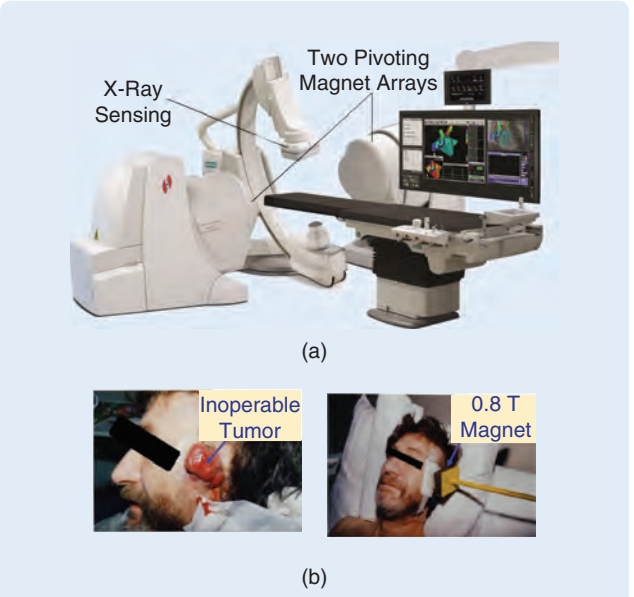

FIGURE 2 Magnetic control of treatment in patients. (a) The magnetic navigation system by Stereotaxis, in alliance with Philips, Siemens, and Biosense Webster Inc., utilizes two pivoting 350-kg 0.1-T NdBFe permanent magnet arrays, positioned on either side of the patient (~70 cm apart), which provide enough force control to precisely manipulate a surgical tool with a magnetic tip in three spatial dimensions [126]. The real-time in-vivo location of the manipulated tool is sensed by X-ray fluoroscopy [127]. (Image courtesy of Stereotaxis and is reproduced with permission.) (b) Magnetic drug targeting. The patient shown had an advanced and inoperable face tumor. A ferrofluid of magnetic nanoparticles coated with chemotherapy was focused to the tumor by a single externally held 0.8-T rectangular permanent magnet [11].

of human physiology and how nanoparticles travel from blood to tissue under magnetic actuation. To this end, quantitative modeling is presented for nanoparticle transport in and around blood vessels [88], [90] and is verified as far as is possible against available experimental data in-vitro (outside a living organism) [107], [194] and in-vivo (in animals and humans) [11], [86], [105]. This same modeling is then applied to breast cancer patient autopsy data to choose open-loop magnetic shift strategies to better reach thousands of metastatic poorly vascularized deep microtumors [91]. Shift does not require real-time nanoparticle imaging, is simpler to implement than closed-loop control, and has the potential to improve treatment of metastatic disease. Finally, model-based closed-loop algorithms are developed for focusing a distributed ferrofluid on average to a central deep target, with the first algorithm chosen by intuition [102] and the second (and far superior version) designed by semidefinite constrained programming [195]. These distributed fluid focusing algorithms have not yet been implemented experimentally, neither in bench-top experiments and certainly not yet in animals. The conclusion of the article outlines the many steps that must still be taken to move these ideas and results from the laboratory to patient care.

It is important to stress that no single magnet hardware implementation or set of control algorithms will be appropriate for all clinical needs; what is best for treating inner ear pathologies is different from control design for focusing chemotherapy to a single inoperable tumor and is again different from magnetic actuation to better reach thousands of poorly vascularized microscopic tumors. Instead, the design of magnet systems and control algorithms must rely on an understanding of classes of expected patient disease profiles, and this requires close interactions with clinicians. This article presents two very different examples—inner ear and deep tumor targeting—to show a sampling of design and control issues. From these two examples, it is clear that there is ample room for both simple magnet designs and control strategies to improve care (such simple solutions can likely be brought to patients faster), as well as for advanced feedback control design (for high performance in the longer term). Overall, the range of current results by our group [88], [90], [91], [100]–[102], [125], [191]–[193], [195] and by others [137], [144]–[146], [150], [151], [158], [159], [161]–[163] shows that design, optimization, and control tools have the potential to significantly improve magnetic drug targeting capabilities. Achieving such improvements will require control implementation for a complex biological environment that is interesting, important, and presents many new and novel control challenges.

MODELING OF MAGNETIC FIELDS AND FORCES

Describing magnetic fields and the forces they create on nanoparticles is standard physics. It is a natural place to start before considering particle transport in the body. Electromagnetic fields are classically described by Maxwell's equations. For stationary or slowly varying applied magnetic fields (as compared to radio frequencies), the magnetostatic equations are appropriate [196]

$$\nabla \times \vec{H} = \vec{j} \tag{1}$$

$$\nabla \cdot \vec{B} = 0 \tag{2}$$

$$\vec{B} = \mu_0(\vec{H} + \vec{M}) = \mu_0(\vec{H} + \chi\vec{H}), \tag{3}$$

where $\vec{B}$ is the magnetic field [in units of tesla], $\vec{H}$ is the magnetic intensity [A/m], $\vec{j}$ is the current density [A/m^2], $\vec{M}$ is the material magnetization [A/m], χ is the magnetic susceptibility [unitless], and $\mu_0 = 4\pi \times 10^{-7} N/A^2$ is the permeability of a vacuum. These equations hold both in vacuum and in materials and for permanent magnets (magnetization $\vec{M} \neq 0$) and electromagnets (current $\vec{j} \neq 0$). Magnetic fields pass virtually unchanged through the human body because the magnetic susceptibility of tissue is close to zero ($\chi_{\text{tissue}} \approx 10^{-6}$ to 10^{-4}) [197], [198]. In contrast, the magnetite cores (Fe_3O_4) of ferromagnetic particles have magnetic susceptibilities five to seven orders of magnitude higher than that of tissue ($\chi \approx 20$) [199], [200], resulting in strong interactions with magnetic fields.

The magnetic force on a single spherical particle depends on the magnetic field and field gradient created at its location [108], [201], [202]

$$\vec{F}_{\text{mag}} = \frac{4\pi a^3}{3}\frac{\mu_0\chi}{(1+\chi/3)}\left[\frac{\partial \vec{H}}{\partial \vec{x}}\right]^T \vec{H} = \frac{2\pi a^3}{3}\frac{\mu_0\chi}{(1+\chi/3)}\nabla(\|\vec{H}\|^2), \tag{4}$$

where a is the radius of the particle, $\vec{x} = (x, y, z)$ is its position vector, and ∇ is the gradient operator. This expression can be derived by recognizing that a conservative force can be written as the gradient of a potential energy $\vec{F} = -\nabla U$ [196]. Here the potential magnetic energy of the particle is equal to the applied magnetic field multiplied by the particle magnetization and so is proportional to the square of the magnetic field strength ($U = -\kappa\|\vec{H}\|^2$) [203]–[205]. Equation (4) states that the magnetic force on a particle always points from low to high magnetic field intensity, up the gradient of $\|\vec{H}\|^2$. The middle expression in (4) is usually used in the magnetic drug delivery literature [178], [202], [206], which illustrates that a spatially varying magnetic field with a nonzero Jacobian matrix ($\partial\vec{H}/\partial\vec{x} \neq 0$) is required to create a magnetic force, and it is equivalent to the last expression in (4) by the chain rule. If the applied magnetic field is sufficiently strong to saturate the particle [206], then $[\partial\vec{H}/\partial\vec{x}]^T\vec{H}$ in (4) is replaced by $[\partial\vec{H}/\partial\vec{x}]^T\vec{M}_{\text{sat}}$ where $\vec{M}_{\text{sat}}$ is the saturated magnetization of the particle [178], [206], [207]. For well-made particles, $\vec{M}_{\text{sat}}$ is large—on the order of $\|\vec{M}_{sat}\| \sim 0.5$ T [41], [107]. Since $\vec{M}_{\text{sat}}$ lines up with $\vec{H}$, this saturation does not change the direction of the force, only its size.

Equation (4) also shows that the magnetic force scales with particle volume, with a particle ten times larger experiencing a magnetic force a thousand times greater. Since creating sufficient magnetic force is an issue, this makes it preferable to use larger particles. There is, however, a trade off. Therapeutic magnetic particles must be sufficiently small to effectively act as drug carriers in the body: to extravasate through blood vessel walls into surrounding tissue [21], to pass through barriers like the ear's round window membrane (RWM) [208], and to elude the immune system that removes them from circulation long enough to provide effective therapy (larger particles are detected and removed more quickly) [17], [21]. Larger particles can also experience a substantially greater tissue resistance to particle motion [110], [111], [209]. An appropriate particle size is about 50–300 nm [11], [73], [86], [107], [118], [168], [174], [176], [210], although both smaller [16], [22] and larger [105], [165] particles have been used depending on the clinical need and desired target location (see Table 1).

MAGNETIC PUSHING

Equation (4) implies that any single permanent or electric magnet will always attract ferromagnetic particles (Figure 3). However, there are a variety of clinical needs where it would be advantageous to use magnets to push in—to "magnetically inject"—particles. Delivery of therapy to inner ear diseases is such a need. Magnetic injection can be achieved by a fixed

TABLE 1 Range of parameters in human physiology and prior magnetic drug delivery studies. Dimensional parameters needed to determine the nondimensional numbers ψ, $\mathcal{D}$, $\mathcal{D}_T$, and Pe for the model of (21) and (22) are in bold [11], [16], [18], [19], [105], [107], [110], [111], [121], [146], [149], [164], [165], [194], [196], [236].

Parameter	Symbol	Parameter Range
Particle radius	a	1 nm–5 μm
Distance from magnet	d	1 mm–30 cm
Magnetic field strength	$\|\vec{B}\|$	0.1–2.2 T
(or magnetic intensity)	$\|\vec{H}\|$	8×10^4–1.75×10^6 A/m
Magnet length	L_M	1–30 cm
Magnetic drift velocity	$\|\vec{V}_R\|$	9×10^{-15} m/s–3.8×10^{-4} m/s
Magnetic force on a particle at the vessel centerline	$\|\vec{F}_{\text{Mag}}\|$	**5×10^{-25} – 1.6×10^{-11} N**
Maximum centerline blood speed	$V_{B\max}$	**0.5 mm/s–40 cm/s**
Vessel diameter	d_B	**7 μm–3 cm**
Blood viscosity	η	0.003 Pa s
Centerline Stokes drag on a particle	$\|\vec{F}_{\text{Stokes}}\|$	**3×10^{-14}–1.1×10^{-7} N**
Temperature	T	310 K (body temperature)
Brownian diffusion coefficient	D_B	1×10^{-14}–1×10^{-12} m^2/s
Scattering diffusion coefficient	D_S	3.5×10^{-12} – 6×10^{-10} m^2/s
Total diffusion coefficient (in blood)	D_{Tot}	**1×10^{-14} – 6×10^{-10} m^2/s**
Diffusion coefficient (in membrane)	D_M	**0 (if particles larger than pores) –1.5×10^{-12}**
Diffusion coefficient (in tissue)	D_T	**0 (if particles larger than interstitial spaces) –1.2×10^{-14}**

arrangement of just two permanent magnets [191], [192] and so does not require dynamic magnet actuation or closed-loop feedback control. It is a situation where a simple concept in control (an unstable node) can make a significant impact in patient care.

The inner ear is behind the blood-brain barrier, which means that all blood vessels that supply the inner ear have vessel walls that are impermeable even to small drug molecules [211]. Thus drugs cannot diffuse from the blood out to the surrounding tissue in the brain and inner ear as they can in the rest of the body. There are a variety of ear pathologies that would likely benefit from even currently available drugs if those drugs could only be delivered to the inner ear. Acute noise-induced injury, uncontrolled labyrinthitis (dizziness), and profound tinnitus (loud ringing in the ears) affect millions of people [212]–[215]. However, injested or injected drugs, which then circulate in the patient's blood, do not pass from the blood stream into the inner ear [216]. To circumvent this blood-ear barrier, a magnetic force has been used to pull drug-coated nanoparticles placed in the middle ears of guinea pigs through their

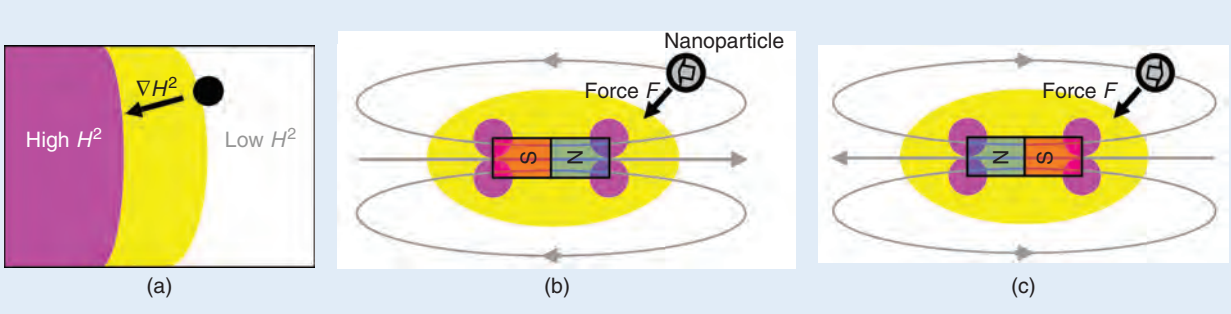

FIGURE 3 Ferromagnetic particles are attracted to regions of highest magnetic field intensity (magnet corners). (a) A ferromagnetic particle (black dot) experiences a magnetic force (arrow) from low to high (white to pink) magnetic field intensity squared. Thus a single permanent magnet (b) attracts particles to its corners where the magnetic field intensity is highest, and (c) this force remains unchanged if the polarity of the magnet is reversed (gray curves show the magnetic field lines; the open arrow shows the corresponding magnetization direction inside the particle).

RWMs into their inner ears by using a strong (0.8 T) magnet held on the opposite side of their heads [217].

While guinea pig ears are similar to human ears, their heads are much smaller. To pull particles into the inner ear of human patients, a magnet would have to be placed on the opposite side of the head at a 12–15-cm working distance from the RWM. Since magnetic fields and forces fall off quickly with the distance from the magnet, this pull magnet would need to be extremely strong, exceeding FDA safety limits [218], to create the same forces at the human RWM as were used to pull particles through the membrane in the guinea pig experiments. A magnet of such size and strength would also be large, expensive, unwieldy, and dangerous to handle [47]. Instead, the ability to *push* particles magnetically from the same side as the diseased ear—over just a 3–5-cm working distance—would facilitate effective treatment with lower and safer magnetic fields.

Figure 4 shows the envisioned treatment paradigm. A syringe would first be used to physically place a gel with therapeutic nanoparticles into the middle ear cavity, instead of delivering drugs into the bloodstream. Then magnetic push would be used to move the therapy from the middle to the inner ear. While injecting therapy into the tympanic cavity (the middle ear) is standard, safe, and can be done with a syringe [219], the same syringe cannot reach, and would irreparably damage, the much more delicate RWM. An ideal magnetic injector system would be simple, small, affordable, and would allow handheld manipulation under visual guidance for ease of use and widespread clinical adoption.

Any single magnet always pulls particles toward itself, but a combination of just two magnets can push [191]. As shown by (4), magnetic forces point from low to high $\|\vec{H}\|^2$. To create an outward push force, there must be a region where $\|\vec{H}\|^2$ is increasing going away from the magnets. One easy way to achieve this is to create a local magnetic intensity $\|\vec{H}\|$ minimum at a distance from the magnets: beyond this minimum the magnetic field intensity increases outward and creates outward forces. The intensity minimum can be created by canceling the magnetic field at a removed node location, as shown in Figure 5. A single magnet exhibits the field lines illustrated in the first panel. When the magnet is tilted clockwise, along a chosen field line, there is a location where the magnetic field is purely horizontal (point A). A second identical magnet, flipped and tilted counter-clockwise, has a corresponding location (point B) where the magnetic field is purely horizontal in the opposite direction and has the same magnitude. If these two magnets are positioned as shown in Figure 5, so that points A and B overlap at point C, the magnetic fields add together (Maxwell's equations are linear)

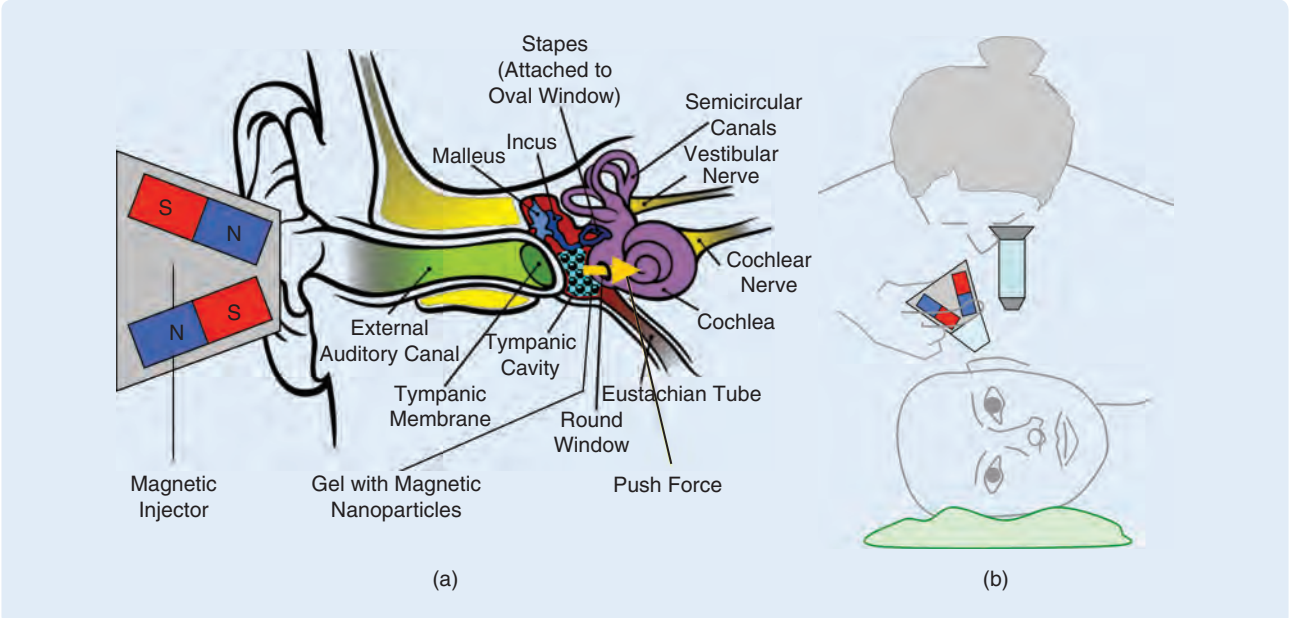

FIGURE 4 Magnetically injecting nanoparticles into the inner ear [191]. The inner ear is behind the blood-brain barrier: microcirculation vessels that supply blood to the cochlea have impermeable vessel walls that prevent most therapies from exiting the bloodstream and reaching inner ear diseases. Pushing particles through the round window membrane (RWM) would bypass this blood-brain barrier and allow therapy to reach the inner ear. (a) The envisioned treatment is shown, from left to right: the magnetic push system, the human ear anatomy, a gel filled with magnetic nanoparticles that has been injected by syringe into the middle ear (light blue with black dots, in the tympanic cavity), the round window membrane (black oval), and the magnetic push force (yellow arrow) to deliver therapeutic particles through the RWM into the inner ear (cochlea). (b) In patients, the niche that contains the RWM, although not the RWM itself, can be seen. The RWM itself can be visualized using a flexible microendoscope. Thus an ear doctor could manipulate the syringe under visual observation and the push device under some combination of visual and computer tomography guidance to direct magnetic particles into the inner ear.

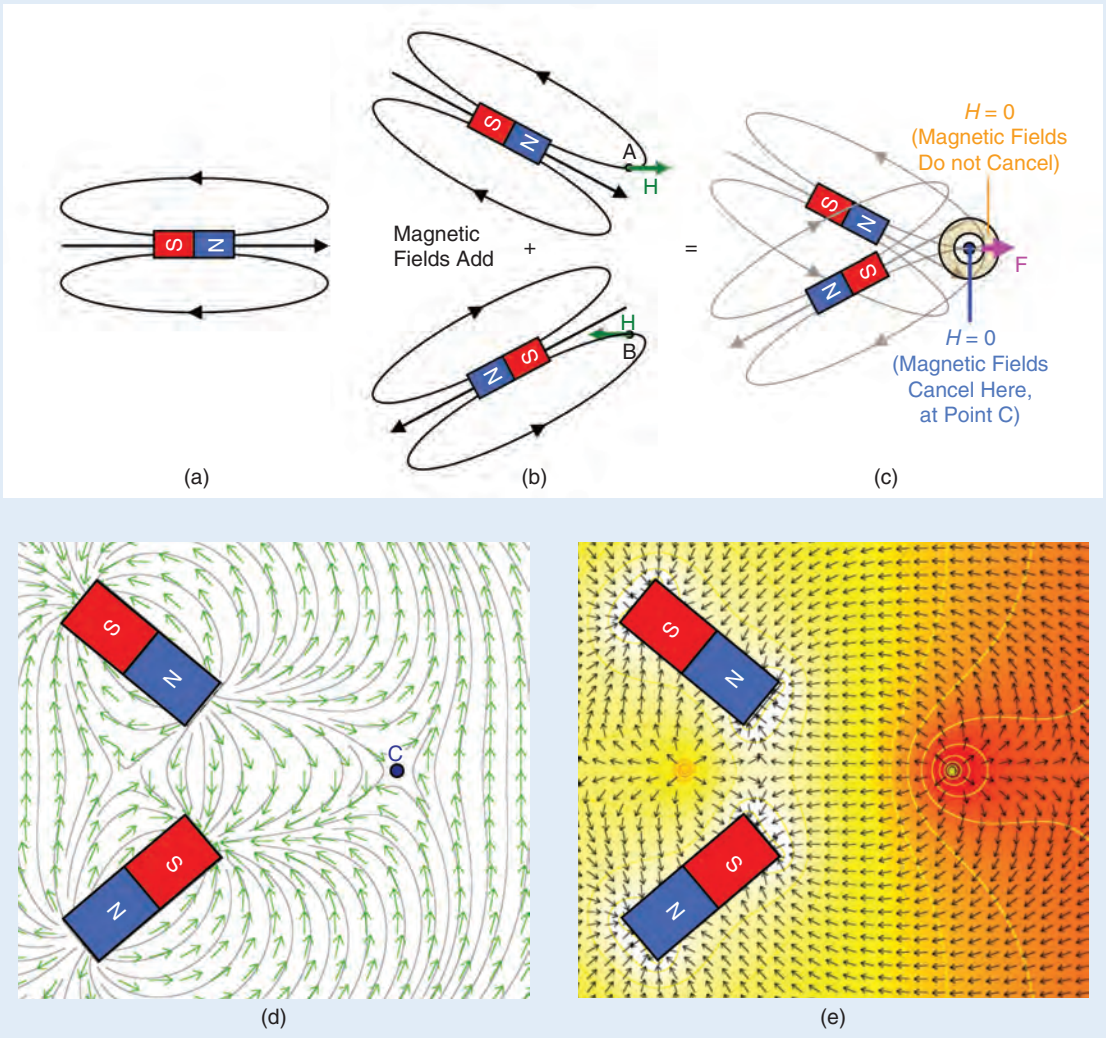

FIGURE 5 Two magnets can create a magnetic field cancellation. Particles are pushed out from that node [191]. (a) Schematic field lines around a single permanent magnet magnetized along its length. (b) Two magnets. Tilting the top magnet down till the magnetic field $\vec{H}$ is along the positive x axis at the desired node location (green dot). Reversal and upward tilting of the other magnet. (c) When these two magnets are correctly overlaid, their magnetic fields combined exactly cancel at the node point C (big dot), but they do not cancel around that point (orange annulus). Resulting forces go outward from $\vec{H} = 0$ at the node to $\vec{H} \neq 0$ surrounding it—the pink force arrow. (In (c), the light gray lines are only guides for the eye and are not magnetic field lines.) (d) Magnetic field directions (green arrows) and magnetic field lines (gray curves) from a simulation of Maxwell's equations. The displaced node is again shown by the big dot. (e) Magnetic forces (directions shown by black arrows) go from low to high magnetic field intensity $\|\vec{H}\|$ (shown by the coloring on a log scale), showing the region of push forces to the right of the node. For the ear application in Figure 4, the doctor would position the system so that the node (point C) is held behind the gel of nanoparticles, and then the magnetic forces beyond the node would push particles from the gel through the round window membrane and into the cochlea.

and exactly cancel at point C to create a zero magnetic field ($\|\vec{H}\| = 0$). Since the magnetic fields do not cancel at other points surrounding C, this point is a local minimum of $\|\vec{H}\|^2$. Forces on the nanoparticles go from low to high magnetic field strength squared, so in the region beyond C they push particles away from the two magnets.

Magnetic push has been confirmed in simulations and hardware experiments [191], as well as in live animals [192]. Mimicking the first step of the human treatment paradigm shown in Figure 4, red fluorescent 300-nm diameter iron-core Chemicell particles were first injected by a 1-cc 28.5 gage insulin syringe (Beckton-Dickson) into the middle ears of 15 rats (Long-Evans strain, Charles River) through their tympanic (ear drum) membranes. This procedure filled the middle ear space with magnetic nanoparticles.

The goal of the magnetic push is to safely move the nanoparticles into the inner ears of the rats. The evaluated push system consisted of four 1.3 T (5.08 cm × 2.54 cm × 2.54 cm, Applied Magnets) magnets encased in a polymer holder fabricated by a three-dimensional printer (personal

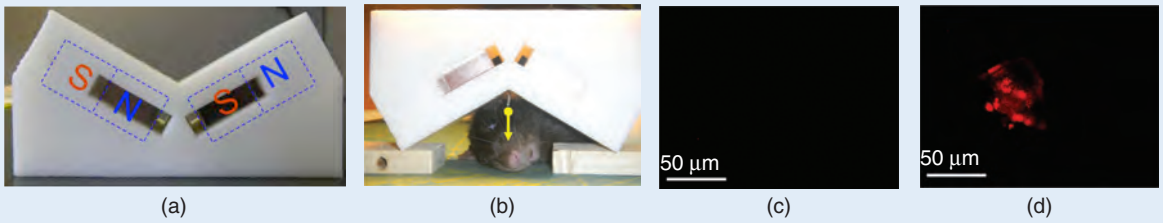

FIGURE 6 Magnetic pushing of 300-nm diameter Chemicell nanoscreen MAG/R-D particles into the inner ears of rats [192]. (a) The magnetic push system for these rat experiments. Two pairs of magnets are inside the white polymer holder, behind the two slots—their position and magnetization is shown by the dashed blue outlines and the North–South (N–S) lettering. (b) Experimental setup. The device is placed upside down above the rat's head in order to align the push node (yellow dot and down force arrow) on axis with the rat's round window membrane (here marked by the small, just visible, white rolled tissue paper above the yellow dot). Red fluorescence was measured from cochlea tissue scrapes. (c) No fluorescence from magnetic red particles is visible in a cochlea tissue scrape for a rat where push was not used versus (d) many particles in the cochlea of a rat where magnetic push was applied.

portable 3D printer, PP3DP). Two magnets were inserted side-by-side on each side of the holder in a "V" geometry [Figure 6(a)]. For these first animal push experiments, it was easier to use four smaller magnets aligned side by side in pairs instead of two twice-as-large magnets that would have been more dangerous to handle. Likewise, using a push node on the back side of the V configuration, which is a node that has not yet been extended out to the 3–5-cm distance required for human ear treatments, was a convenient starting point as it allowed for an easier creation of strong push forces. In four rats, this magnetic push system was held next to the rat ears for 1 h with the push node aligned with the long axis of the base turn of the rats' cochlea [Figure 6(b)]. Four rats were used as negative tests and had no magnetic push applied.

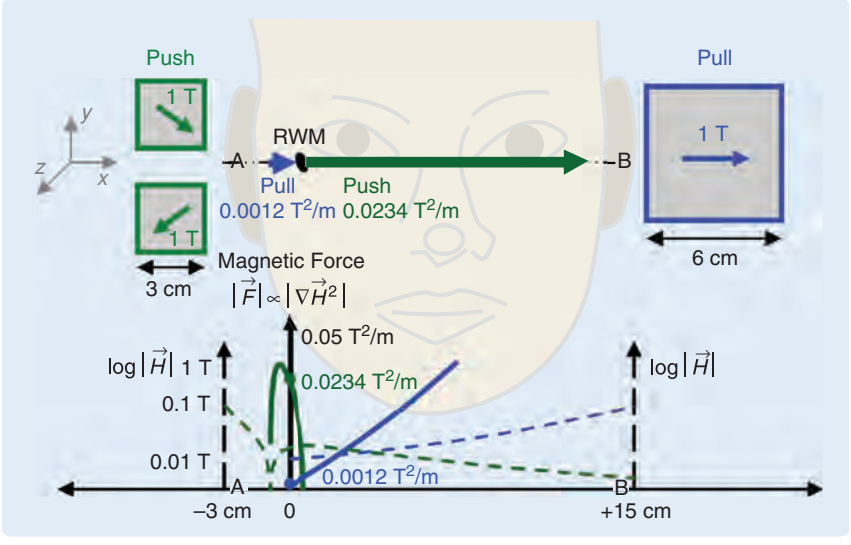

FIGURE 7 Quantitative comparison of magnetic push versus pull to transport therapeutic nanoparticles through the round window membrane (RWM) into the inner ear. The width of the human head is about 18 cm on average (from A to B), and the RWM membrane (black filled ellipse) is about 3 cm deep. An optimal push system is shown in green. It consists of four 1-T 3-cm cube magnets (total magnet volume = 108 cm^3), with optimal magnetization directions (green arrows from south to north) shown for the two magnets in the *xy* plane. The two magnets in the *xz* plane correspond to rotating the *xy* assembly 90° around the x axis. For comparison, pull is shown in blue for a 1 T 6 cm on a side magnet (volume = 216 cm^3) on the opposite side of the head. Graphs along the bottom show the resulting computed magnetic field strength and magnetic forces. The strength of the magnetic field $\|\vec{H}\|$ is shown by the dashed curves according to the log $\|\vec{H}\|$ scale on the left dashed vertical axis (from 0.01 T to 1 T). Force is proportional to $\nabla\|\vec{H}\|^2$ and is shown using solid curves and the scale of the solid middle vertical axis. For all four curves, push is colored green and pull is shown in blue. Since magnetic fields and forces fall off quickly with distance, and since push only has to occur over a short 3-cm length, pushing significantly outperforms pulling. At the RWM, pull creates $\nabla\|\vec{H}\|^2 = 0.0012\ T^2/m$ while push has $\nabla\|\vec{H}\|^2 = 0.0234\ T^2/m$, a 20 times larger force for any particle size (also shown to scale by the blue versus green horizontal force arrows on top at the RWM black ellipse).

Magnetic push must now be extended to human distances, which is the 3–5 cm between the outside of the ear and the RWM. A four-magnet design that is appropriate for handheld use and will generate sufficient push at

a distance of 3 cm is displayed on the left of Figure 7 (only two of the four magnets are shown). The design has four cubic magnets as close to the ear as possible to create maximum strength forces, but the magnets are magnetized at an angle to create the push node. The magnetization angles (the green 1 T arrows) were chosen by semidefinite programming and are guaranteed to be the globally optimal angles to maximize pushing force at the RWM given magnet size and 1 T strength constraints (see [125] for details and a demonstration of global optimality). Compared to the pull created by a twice as large uniformly magnetized magnet on the opposite side of the head, the push force at the RWM (proportional to $\nabla\|\vec{H}\|^2 = 0.0234\ \mathrm{T}^2/\mathrm{m}$ for any particle size) exceeds the pull force ($\nabla\|\vec{H}\|^2 = 0.0012\ \mathrm{T}^2/\mathrm{m}$) by a factor of 20. Push beats pull because push only has to operate over a short distance while pull must act through the width of the human head. The variation of the magnetic field strengths and forces with distance from the push and pull magnets is shown in the graphs at the bottom of the figure. (For the optimal push magnetization angles, the green push force curve reaches its peak about half a centimeter before the RWM. If the magnetization angles are modified to shift the force peak to the right, the drop in peak force due to the added 0.5-cm distance exceeds the benefit gained by placing a force peak at the RWM.) This four-magnet design is currently being constructed and, like the device in Figure 6, will also be tested in rats.

In addition to increasing the push distance, there are multiple other steps that must be taken to move this concept from the laboratory to patient care. The best nanoparticle size must be selected by a sequence of animal experiments. Magnetic forces scale with particle volume (4) but tissue resistance forces do not necessarily follow a simple scaling law: they can be modest for small particle sizes and then grow rapidly as particles exceed a certain tissue-dependent size [110], [111], [221]. Experimentally informed tissue models [110], [111], [209] indicate that particle size has a dramatic impact on the ability of magnetic fields to transport particles through tissue [91]. However, since the resistance of RWMs to nanoparticle motion has not yet been studied, the best choice of particle size for ear treatments will have to be ascertained through both modeling and experiments. It will further be necessary to show that magnetic push treatment is efficacious: that magnetic particles coated with drugs can treat a specific ear disease. That will require inducing that disease in animals and then showing that magnetic push can safely treat it. Comprehensive safety and efficacy trials in a statistically significant number of animals must then follow to lead to human trials, regulatory approval, commercialization, and finally adoption of the technology by clinicians to better treat patients.

EX-VIVO SINGLE DROPLET CONTROL

Before turning to dynamic control of nanoparticles in-vivo (inside the body), this section discusses robust and optimal magnetic control of a single drop of ferrofluid in a petri dish (see Figure 8). The purpose of these experiments is to first understand and solve magnetic control challenges in a situation that does not yet involve tissue or live animals. Ex-vivo manipulation of a ferrofluid drop by electromagnets at a distance already introduces key engineering issues that must also be addressed during in-vivo manipulation. These include consideration of the nonlinear nature of the magnetic forces, the need for smooth switching of magnets as the ferrofluid travels, electromagnet time delays, optimal exploitation of available magnet strengths, and model uncertainties. The algorithm presented below has been experimentally demonstrated for steering a droplet in the plane by four external electromagnets using minimal electrical power [100], [193].

The magnetostatic equations (1)–(3) hold for the case of electromagnetic actuation across a petri dish. The magnetic force on the ferrofluid droplet, which is composed of many nanoparticles in water held together by surface tension, points in the same direction as stated in (4) for a single particle. This magnetic force creates a droplet motion, and because the ferrofluid has a negligible mass and the surrounding mineral oil opposes motion by viscous drag forces, the droplet immediately achieves a steady-state velocity

$$\vec{v}_{\mathrm{droplet\_ss}} = \sigma \nabla \|\vec{H}\|^2, \tag{5}$$

where σ is a scalar coefficient measured to be on the order of $10^{-13}\ \mathrm{m}^4/\mathrm{A}^2\,\mathrm{s}$, with its value dependant on the details of how the magnetic particles aggregate within the water and

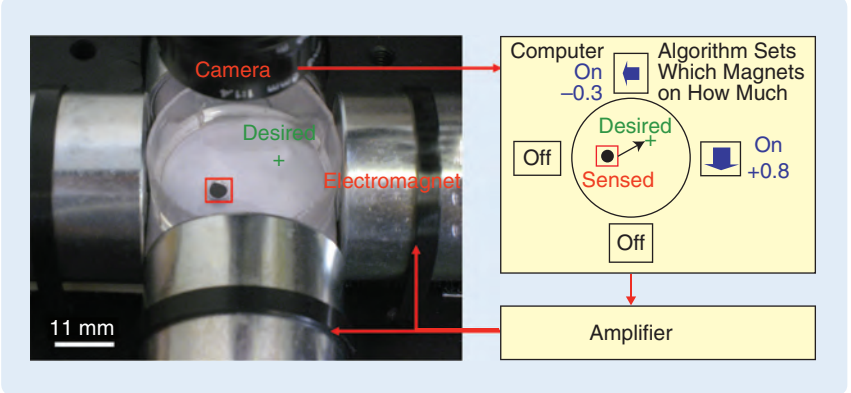

FIGURE 8 The experiment for dynamic control of a single ferrofluid drop ex vivo [193]. A camera, computer, amplifier, and the four electromagnets are connected in a feedback loop around a petri dish containing a single drop of ferrofluid. The camera observes the current location of the droplet; the computer, using the optimal nonlinear control algorithm described in the text, computes the electromagnet actuations required to move the droplet to where it needs to be; and the amplifier applies the needed voltages for actuation.

oil [193]. The term $\nabla\|\vec{H}\|^2$ determines the direction of the applied magnetic velocity. $\vec{H}_1(x, y)$, $\vec{H}_2(x, y)$, $\vec{H}_3(x, y)$, and $\vec{H}_4(x, y)$ represent the magnetic fields in the xy plane across the petri dish when each magnet is turned on with a unit of ampere current, and all the other magnets are turned off. The instantaneous electrical current in each of the four magnets is denoted by u_1, u_2, u_3, and u_4, then the linearity of the magnetostatic equations (1)–(3) implies that

$$\vec{H}(x, y, t) = u_1(t)\vec{H}_1(x, y) + u_2(t)\vec{H}_2(x, y) + u_3(t)\vec{H}_3(x, y) + u_4(t)\vec{H}_4(x, y). \quad (6)$$

During magnetic control there is no direct access to currents, making it impossible to instantly charge an electromagnet to any desired strength. Instead, the control sets the vector of voltages $\vec{V}(t) = [V_1(t)\ V_2(t)\ V_3(t)\ V_4(t)]^T$.

To first order, the current in each magnet is related to the applied voltage by the time delay dynamics [222]

$$\frac{d}{dt}\vec{u}(t) = -\frac{R}{L}\vec{u}(t) + \frac{1}{L}\vec{V}(t), \quad (7)$$

where R and L are the resistance and inductance of the magnets. Substituting (6) into (5) gives

$$\begin{aligned}\frac{d}{dt}[x(t)\ \ y(t)] &= \sigma\nabla\left\|\sum_{i=1}^{4} u_i(t)\vec{H}_i(x,y)\right\|^2 \\ &= \sigma\sum_{j=1}^{4}\sum_{i=1}^{4} u_i(t)[\nabla(\vec{H}_i(x,y)\cdot\vec{H}_j(x,y))]u_j(t) \\ &= \sigma[\vec{u}^T(t)P_x(x,y)\vec{u}(t) \quad \vec{u}^T(t)P_y(x,y)\vec{u}(t)], \quad (8)\end{aligned}$$

where $[x(t)\ \ y(t)]$ is the current location of the droplet in the petri dish, the second equality was achieved by carrying out the square and then moving the gradient operator into the resulting double summation, and the last equality is a compact matrix representation with superscript T denoting vector transposition and the matrices P_x and P_y defined as

$$\begin{aligned}P_x(x, y) &\triangleq [\partial(\vec{H}_i(x, y)\cdot\vec{H}_j(x, y))/\partial x]_{4\times 4} \\ P_y(x, y) &\triangleq [\partial(\vec{H}_i(x, y)\cdot\vec{H}_j(x, y))/\partial y]_{4\times 4}. \quad (9)\end{aligned}$$

Together with (7), equations (8) and (9) describe droplet motion under electromagnet control, they provide a dynamic map from the voltages applied to the four magnets to the resulting motion of the droplet, from $\vec{V}$ to $\vec{u}$ to $(\dot{x}, \dot{y})$. The control $\vec{u}$ appears quadratically in the model and the P matrices are strongly nonlinear in space [193].

The control for droplet steering is explicitly designed to account for the nonlinear aspects of (8) and (9). Let $\vec{d} = \vec{x}_{\text{desired}} - \vec{x}_{\text{measured}}$ be the vector error between the drops desired and measured position. The control applies the correcting velocity $\vec{v} = k\vec{d}$ where k is a scalar gain and $\vec{v} = (v_x, v_y)$. This sets two (out of four) control degrees of freedom according to

$$\begin{aligned}\sigma\vec{u}^T[P_x(x, y)]\vec{u} &= v_x \\ \sigma\vec{u}^T[P_y(x, y)]\vec{u} &= v_y. \quad (10)\end{aligned}$$

Minimizing the total electrical power drawn by the magnets is equivalent to minimizing the quadratic cost function

$$J \triangleq \|\vec{u}\|^2 = \vec{u}^T\vec{u}. \quad (11)$$

Thus the goal is to choose $\vec{u}$ to minimize J subject to the constraints of (10) and then to control the magnet voltages $\vec{V}$ to achieve those magnet currents $\vec{u}$. The optimization proceeds by identifying a parametric family of all solutions of (10), this specifies the constraint space, and then explicitly minimizing the cost function (11) across this space.

For any (x, y) ferrofluid location, and for each desired correction velocity $\vec{v} = (v_x, v_y)$, the constraint space of (10) is a two-dimensional surface in the four-dimensional space of all possible actuations of the magnets. All points $\vec{u}$ on this surface create the desired droplet velocity $\vec{v}$. Set the vector $\vec{p}$ to be the magnetic field at the location of the ferrofluid

$$\sum_{j=1}^{4} u_j\vec{H}_j(x, y) \triangleq \vec{p}. \quad (12)$$

The two-dimensional quadratic constraint of (10) can now be broken up into two equivalent linear constraints [100] given by (12) and

$$2\sigma\sum_{j=1}^{4} u_j\nabla(\vec{p}^T\vec{H}_j(x, y)) = \vec{v}. \quad (13)$$

Equations (12) and (13) are a set of two two-dimensional equations (four equations in total) for $\vec{u}$ and $\vec{p}$ (for six unknowns) rather than one quadratic two-dimensional equation for $\vec{u}$ alone (two equations for four unknowns). The advantage of this second formulation is that it is linear in $\vec{u}$. For any chosen $\vec{p}$, there are four equations for the four actuation variables (u_1, u_2, u_3, u_4). Inverting (12) and (13) gives $\vec{u}$ in terms of $\vec{p}$ and $\vec{v}$ as shown in (14) at the bottom of this page.

This $\vec{u}$ exactly achieves the desired correction velocity $\vec{v}$. Note that there are two different fields acting at the ferrofluid: the magnetic *force* that is proportional to $\nabla\|\vec{H}(x, y)\|^2$ and sets the droplet velocity as stated by (5), and the magnetic *field* $\vec{H}(x, y)$ at the drop's location denoted by $\vec{p}$ in (12).

$$\vec{u} = \begin{bmatrix} \vec{H}_1(x,y) & \vec{H}_2(x,y) & \vec{H}_3(x,y) & \vec{H}_4(x,y) \\ \nabla(\vec{p}^T\vec{H}_1(x,y)) & \nabla(\vec{p}^T\vec{H}_2(x,y)) & \nabla(\vec{p}^T\vec{H}_3(x,y)) & \nabla(\vec{p}^T\vec{H}_4(x,y)) \end{bmatrix}^{-1} \begin{bmatrix} \vec{p} \\ \vec{v}/2\sigma \end{bmatrix} \triangleq \vec{g}(\vec{p}). \quad (14)$$

The two do not necessarily align, as is clear both from Figure 3 (the black force arrow does not align with the magnetic field gray arrows along the gray field lines) and Figure 5 [the magnetic field in (d) is not the same as the magnetic force field in (e)]. The change of variables above neatly separates the velocity constraint and the power minimization by using $\vec{p}$ as an intermediate variable. The final step is to search over the magnetic field direction at the ferrofluid location (over $\vec{p}$) to find the minimum power control.

The electrical power cost function $J = \vec{u}^T\vec{u} = \vec{g}^T(\vec{p})\vec{g}(\vec{p})$ is minimized over $\vec{p}$. Using polar coordinates $\vec{p} = \rho[\cos\theta \ \sin\theta]$, J is first minimized with respect to ρ with θ fixed, then a search is performed over θ. The explicit form of $\vec{u} = \vec{g}(\vec{p})$ written in (14) allows for a closed-form solution of the first step. The second step is carried out by a numerical optimization. These two steps yield the globally optimal control $\vec{u}^*$ that creates the desired correcting velocity $\vec{v}$ with minimal electrical power [100], [193]. Figure 9 shows the optimal actuations for moving a ferrofluid drop from left to right. The actuation switches from the top and bottom magnets to mainly the right magnet as the droplet is moved right. This switch occurs since the right magnet is ineffective when the droplet is far away; in that case the droplet can be actuated to the right with lower current by using the closer top and bottom magnets.

The above analysis determines the desired optimal currents $\vec{u}^*$, but it is the voltages $\vec{V}$ that are controlled in the experiment. The low-pass filter (7) gives the relation between $\vec{V}$ and $\vec{u}$, which is compensated by a linear high-pass filter to provide a flat frequency response over the desired closed-loop bandwidth [100]. Additionally, as the ferrofluid traverses its path, there are jumps in the type of control that is optimal. In Figure 9, for example, it is optimal to first use the nearer top and bottom magnets (the first two panels) until the droplet approaches near enough to the right magnet so that its use becomes preferable (the last panel). The need for magnet switching during optimal control is fundamental, and, if there were no magnet-charging time delays, the control would attempt to apply discontinuous currents in time as the ferrofluid moved through space. A specially designed nonlinear filter is included to smooth out the electrical currents while still ensuring that the direction of the created current vector $\vec{u}(t) = [u_1(t) \ u_2(t) \ u_3(t) \ u_4(t)]^T$ accurately tracks the direction of the optimal current vector found above, since it is the direction of the current vector that sets the direction of the ferrofluid droplet motion. This nonlinear filter smooths out the control in time but does not degrade droplet manipulation performance [100]. Reference [100] also extends the method to single droplet control in three spatial dimensions, but this has not yet been demonstrated experimentally.

Control Design for Magnetic Field Uncertainty

Here the optimal single droplet control scheme is modified to account for magnetic field uncertainty. This uncertainty, which can result from variations in electromagnet shapes, strengths, and material parameters, is an engineering uncertainty. Biological uncertainty, the variability of relevant parameters in live tissue, is far more extensive and complex and components of it are discussed in the next section on in-vivo modeling. The goal here is to understand and limit errors in the actuated droplet velocity $\vec{v}$ due to magnetic field variations.

From (5), if there is an uncertainty in the magnetic field, the modified velocity of the ferrofluid drop is

$$\vec{v} = \sigma\nabla\| \vec{H} + \delta\vec{H} \|^2 \tag{15}$$

where $\delta\vec{H}$ is the error in the applied magnetic field and is unknown. By expanding the square to first order, the velocity error is

$$\delta\vec{v} = 2\sigma\nabla(\vec{H}\cdot\delta\vec{H}) + O(\|\delta\vec{H}\|^2) \approx 2\sigma\Big[\frac{\partial\vec{H}^T}{\partial\vec{x}}\delta\vec{H} + \frac{\partial(\delta\vec{H}^T)}{\partial\vec{x}}\vec{H}\Big]. \tag{16}$$

Using (6), which defines the nominal magnetic field $\vec{H}$ in terms of the four currents u_1, u_2, u_3, and u_4 and the magnetic field created by each magnet alone $\vec{H}_1$, $\vec{H}_2$, $\vec{H}_3$, and $\vec{H}_4$, and grouping the $\delta\vec{H}$ terms into one matrix and the $\vec{H}_j$ terms into another matrix, gives [100]

$$\delta\vec{v} \approx 2\sigma\,[\delta\mathbf{H}(\vec{x},\vec{u})]\,[\mathbf{H}(\vec{x})]\,\vec{u} \tag{17}$$

where the $\delta\mathbf{H}$ matrix is the collection of all the $\delta\vec{H}$ terms, including $\partial(\delta\vec{H}^T)/\partial\vec{x}$, and has a 2×5 size. The $\mathbf{H}$ matrix includes all of the $\vec{H}_j$ terms and is 5×4. While the magnetic field deviation matrix $\delta\mathbf{H}$ depends on both ferrofluid location ($\vec{x}$) and the electromagnetic currents ($\vec{u}$), the matrix $\mathbf{H}$ changes only with the ferrofluid location since the dependence on control is captured by the $\vec{u}$ at the end. The goal is to minimize the velocity error $\delta\vec{v}$ in the presence of magnetic field uncertainties $\delta\mathbf{H}$. It is not possible to exactly minimize $\delta\vec{v}$ because $\delta\mathbf{H}$ is unknown. However, by neglecting second-order and higher terms, it is possible to minimize an upper bound for the velocity error

$$\|\delta\vec{v}\| \le 2\sigma\|\delta\mathbf{H}(\vec{x},\vec{u})\|\,\|\mathbf{H}(\vec{x})\,\vec{u}\| \tag{18}$$

where $\|\cdot\|$ denotes the induced Euclidean matrix norm. Minimizing $\|\mathbf{H}(\vec{x})\,\vec{u}\|$ can be phrased as minimizing $J_{\text{robust}} = \vec{q}^T\vec{q}$ where $\vec{q} = \mathbf{H}(\vec{x})\,\vec{u}$, which is a quadratic form in which $\vec{u}$ can be chosen in the same way as for the J in (11). This minimization of J_{robust} yields a robust control that still exactly satisfies the desired velocity constraints of (10). There is an expected tradeoff between optimality and robustness, in which a purely robust solution (that minimizes $\vec{q}^T\vec{q}$) requires high power, and an optimal solution (that minimizes $\vec{u}^T\vec{u}$) has no guarantee of robustness [100]. The tradeoff can be set by choosing a mixed cost function

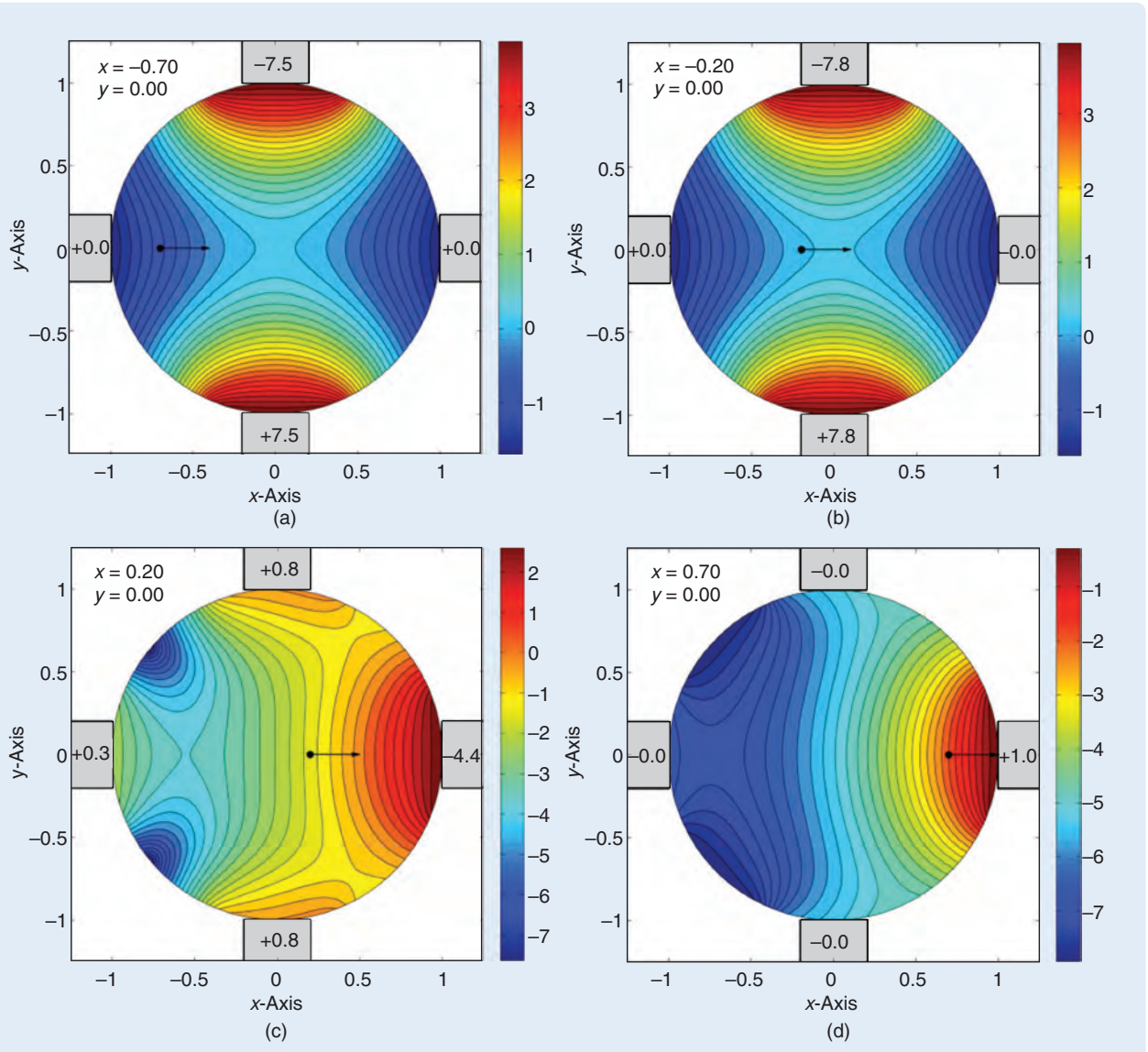

FIGURE 9 Magnetic energy and electromagnetic actuation for minimum power control of a single ferrofluid droplet from left to right [193]. Each panel illustrates a different droplet (x, y) location (the black dot). The black arrow shows the direction of the desired velocity (and thus the applied magnetic force direction), and the color indicates the magnetic potential energy that is proportional to minus the magnetic field intensity squared, $U = -\kappa \|\vec{H}\|^2$ (shown on a logarithmic scale). The text inside each magnet states the current through that magnet (positive for a clockwise current, negative for counter-clockwise).

$J_{\text{mixed}} = \vec{u}^T\vec{u} + \gamma\vec{q}^T\vec{q} = \vec{u}^T[\mathbf{I} + \gamma\mathbf{H}^T\mathbf{H}]\vec{u}$ where the weighting coefficient γ tunes the control from optimal to robust.

Single-Droplet Experimental Results

Figures 10 and 11 present sample experimental results for the optimal control scheme. Optimal manipulation was tested for a variety of ferrofluid drop sizes, as well as desired trajectory shapes and speeds. Volumes were varied from 1 to 20 μL that, under the action of surface tension, corresponded to droplet radii of 0.6–1.7 mm, respectively. The control speed was varied from 0.65 to 1.7 mm/s. In each figure, the columns from left to right show a straight line, square, and spiral trajectory. Time progresses from top to bottom, and each snapshot shows a trace of the droplets' motion over time. The average error between the desired and actual position of the ferrofluid droplet is defined as

$$e_{\text{path}} = \frac{1}{T}\int_0^T \|\vec{x}_{\text{desired}}(t) - \vec{x}_{\text{measured}}(t)\|dt, \tag{19}$$

where T is the time for the droplet to traverse the entire path. For each trajectory, the average velocity and this quantitative average path error are noted on the bottom of that column. Figure 10 illustrates the most straightforward case: control of a slow-moving, medium-sized droplet.

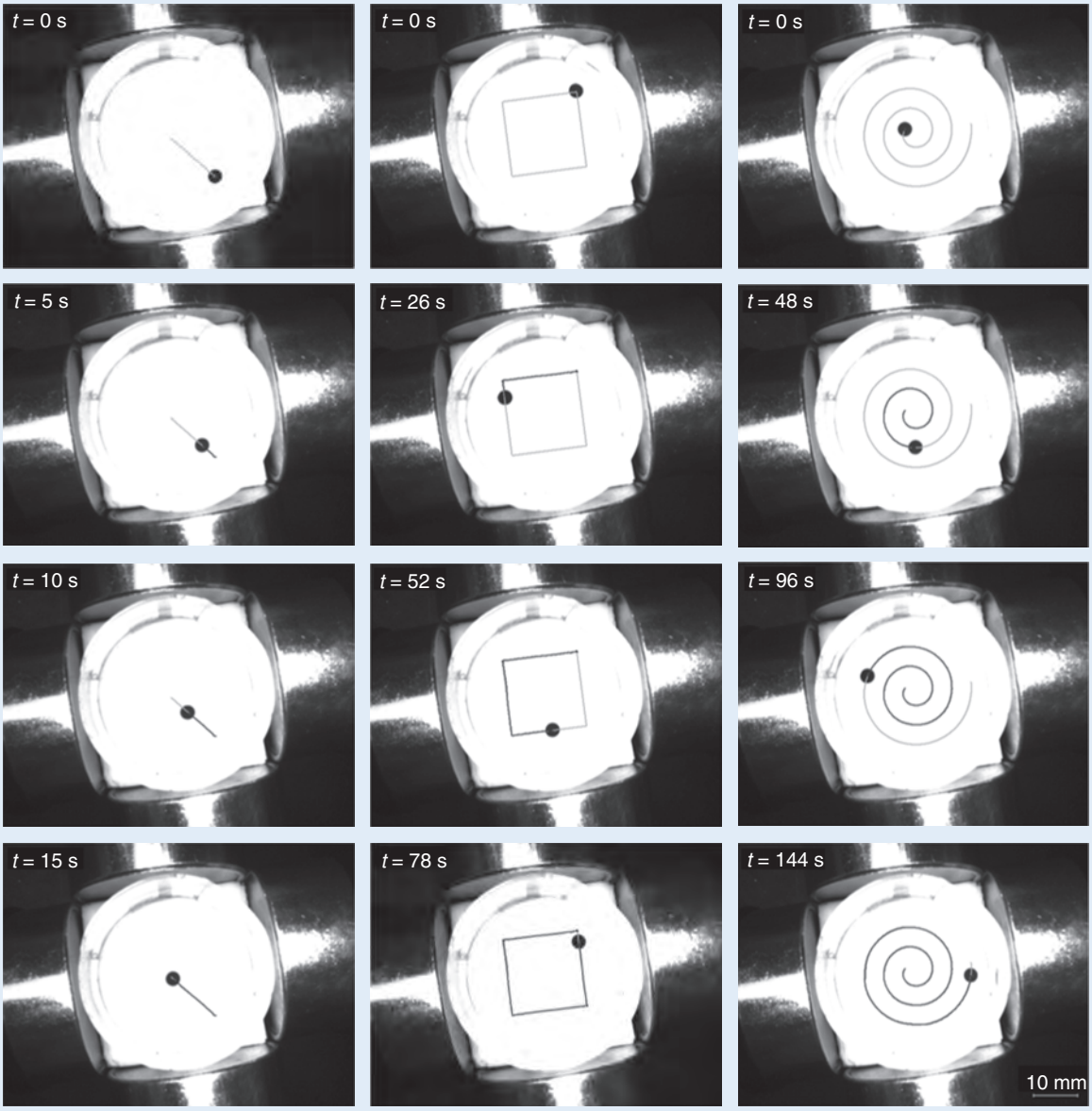

FIGURE 10 Control of a slow-moving, medium-sized 20-μL (1.7-mm radius) ferrofluid droplet along a line, square, and spiral path [193]. A quantitative measure of the average error (19) is noted at the bottom of each column. Movies are online at www.controlofmems.umd.edu/movies/FFmedslow_line.mov, www.controlofmems.umd.edu/movies/FFmedslow_square.mov, and www.controlofmems.umd.edu/movies/FFmedslow_spiral.mov.

Figure 11 shows control of a small drop moving quickly, which is a more difficult task because of the faster speed and because the magnets have to work harder to move the smaller drop (since a smaller drop experiences smaller magnetic forces). Beyond a certain ferrofluid drop size, the single droplet control scheme is no longer feasible. For a large 150-μL droplet (3.3-mm radius), applied magnetic forces exceed the surface tension forces that hold the droplet together, causing the droplet to break into subdroplets (Figure 12).

For control of the small 1-μL droplet, the visible deviation of the ferrofluid from the desired square and spiral paths near the leftmost electromagnet contributes to most of the average positioning error. This deviation occurs in an operating regime where, even for optimal minimum power control, the magnets are being actuated near saturation. It

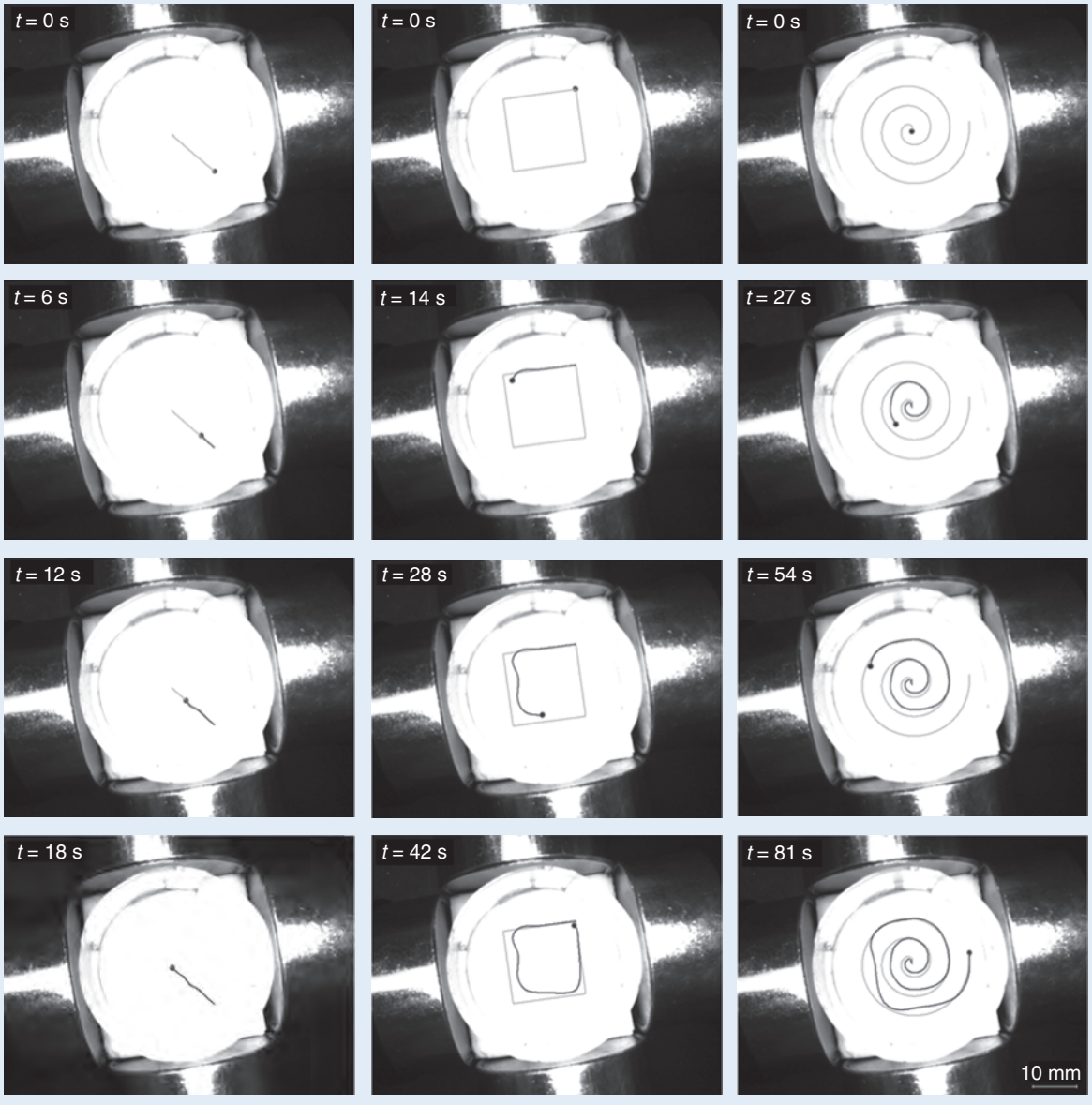

FIGURE 11 Faster control of a small 1-μL (0.6-mm radius) ferrofluid droplet along a line, square, and spiral path [193]. Movies are online at www.controlofmems.umd.edu/movies/FFsmallfast_line.mov, www.controlofmems.umd.edu/movies/FFsmallfast_square.mov, and www.controlofmems.umd.edu/movies/FFsmallfast_spiral.mov.

is likely that different saturation characteristics between the four magnets may be causing the asymmetry seen in the paths in Figure 11. The medium-sized 20-μL droplet can be actuated with less force and the magnets do not approach saturation, thus there is virtually no deviation even during fast control. Additional optimal control experimental results are presented in [100] and [193].

Robust control turns out to be advantageous near magnet edges where the magnetic field is most uncertain. Reference [100] presents a mixed optimal/robust scheme that is robust near the magnet edges and smoothly transitions to optimal control at the center of the petri dish, which works well in experiments. Both the optimal and robust controllers have effectively manipulated single drops of ferrofluid, ranging in volume from 1 to 20 μL, in a 4-cm diameter petri dish, with speeds of 0.033–1.7 mm/s, using four small, inexpensive, and off-the-shelf $\sim$0.13 T electromagnets [193].

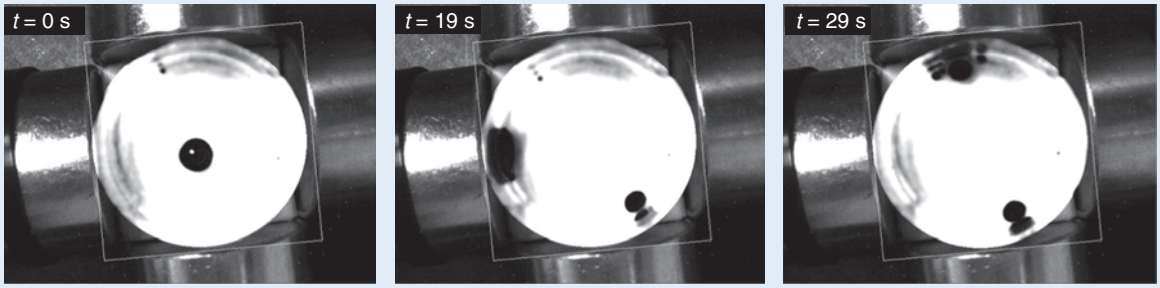

FIGURE 12 Attempted control of a large 150-μL (3.3-mm radius) ferrofluid droplet [193]. As soon as magnetic control is turned on, the droplet breaks up into multiple smaller droplets. This droplet was too big to control effectively.

The underlying purpose of these single droplet experiments was not manipulating a single small object in an inanimate fluid environment, which can be achieved with exquisite precision by other means [223], [224]. Rather, the experiments were to encounter and experimentally solve the initial engineering issues in the magnetic control of ferrofluids. These issues include compensating for the quadratic nature of the magnetic forces, smoothly switching between different types of optimal solutions, dealing with electromagnet time delays, and addressing magnetic field uncertainty. These same issues will remain present during the closed-loop control of ferrofluids in patients. However, to move toward the control of distributed ferrofluids in a biological setting further requires better understanding and quantification of nanoparticle transport through live tissue, in and around blood vessels, and this is discussed next.

MODELING FERROFLUID TRANSPORT IN-VIVO

Modeling the motion of magnetic nanoparticles inside the body is challenging, most immediately because live tissue is so complex and its properties vary significantly from one location to another, from person to person, and many of these properties remain unknown. For example, there is no way to map the complete vasculature of a live patient (MRI can only visualize major vessels [225]), and, even if this vasculature and the blood velocity profile in each vessel were measurable, it is not computationally feasible to resolve particle behavior over seven decades of length scales (from ~100-nm particle size to the meter length scale of a human patient). Minimal models are required that are aimed at answering specific control questions, on an appropriate length scale, with parameters that can be varied over a range of physiological conditions. Then tissue experiments can be designed and implemented to better identify the parameters in these models. This section presents the modeling of ferrofluid transport in and around a single blood vessel. The diameter of the vessel, its blood velocity, the resistance of its walls to particle egress, the properties of the surrounding tissue, and the applied magnetic force can all be varied over a range of expected conditions to predict when magnetic forces will successfully collect particles to surrounding tissue targets. To the degree possible, the model is verified against applicable experimental data from prior hardware [107], [194], animal [86], [105], and human [11] experiments. This style of modeling is then extended to quantify and optimize magnetic sweeping of therapy into breast cancer metastatic tumors in the subsequent section.

Although in some cases, such as the inner ear application illustrated in Figure 4, magnetic particles are introduced into the body outside the blood flow, in most envisioned treatment scenarios particles are injected into the bloodstream [11], [73], [86], [109], [164], [168], [226], [227]. The particles may be injected into a blood vessel immediately upstream of the known disease location, after which magnets are used to try to capture and confine the therapy as it flows by on its first pass [73], [164], [168]. This option is not always possible, as when a clear feeder blood vessel does not exist or is not surgically accessible. Alternatively, the particles may be injected systemically into a major artery [11], [226], [227], in which case they are distributed by blood flow throughout the entire body in minutes and then continue to circulate [228]. In this second case, magnets are used to capture and focus therapy to a disease site when particles pass by the targeted location.

Particles remain in circulation for a limited time, in part because the human immune system is designed to find and remove any foreign bodies [229]. Even for carefully engineered "stealth-coated" nanoparticles, about half of the particle dosage (about 50% of the Chemicell particles used in [11]) is caught within minutes and sequestered to the liver, spleen, and kidneys [71]. The remaining half of the particles are taken out of circulation more slowly, over several hours (~4 h for 30% more) to days, depending on their size and properties. These remaining particles are manipulated during the magnetic targeting.

Nanosized particles are beneficial for two reasons: smaller particles evade the immune system for longer periods, which allows for longer treatment windows [229], and

nanoscopic particles are more likely to leak out of blood vessels into surrounding tissue [110], [111], [229], [230]. This is especially useful when treating cancers, as tumor vessels are often "leakier" than most normal vessels since they are poorly formed and can have submicron gaps or pores that can let through nanoscopic but not microscopic particles [112], [229]–[231].

Therefore the size of magnetic particles must be chosen wisely: they must be small enough to sufficiently evade the immune system and reach target tissue but large enough so that they can be effectively manipulated, as magnetic forces scale with particle volume by (4). In the 1996 human trials, 100-nm diameter particles were used (Figure 13) [11]. Since then, Chemicell has been able to better stealth its particles, and blood circulation times have improved [71]. Consequently, 250-nm diameter particles are planned for future human trials. Even using these larger particles and powerful magnets, the forces created on magnetic particles are still extremely small—tens of pico-Newtons or less (see Table 1). The challenge is to gain *enough* force; applying too much force so that particles tear or otherwise damage tissue has not been an issue. Finally, the strength of the bonds binding the drugs to the particles needs to be chosen so that the drug release rate roughly matches the particle circulation times—previously about 60 min for Chemicell's 100-nm particles [15].

Each set of animal trials has tested just one set of magnetic parameters. Figure 13(b), for example, shows results for 100-nm diameter Chemicell particles with a 0.5 T rod-shaped 5-cm long, 5-mm diameter permanent magnet held against the skin of the rats [86]. These tests require a skilled veterinary surgeon and the results of Figure 13(c) and (d) further require that the rats be sacrificed, dissected, and their tissue slices stained and examined under a microscope. If the animals have tumors, then those tumors must have been seeded by implanting cancer cells into the animals days, weeks, or months before (depending on the tumor rate of growth) and enough animals must be used to achieve statistical significance. Thus, although animal trials remain the final step before testing in humans, it is not feasible to search the magnetic drug-delivery design space using animal experiments.

Rather, models are needed to choose the best magnet placement, size, shape, strength, and dynamic actuation. The next modeling step, beyond (1)–(4), is to better understand what happens in and around a single blood vessel. Figure 14 illustrates the considered simulation domain: it shows a single vessel (delineated in red), the thin endothelial layer that makes up the inside wall of that vessel (in orange), and tissue surrounding that blood vessel (in light brown). It is assumed that systemic blood flow has uniformly distributed the particles before they encounter magnetic forces, hence the inlet concentration of the particles into the vessel is uniform. A magnet is held below the vessel (as shown in the figure inset) and creates downward magnetic forces. Modeling of particle transport in tissue includes these magnetic forces plus particle diffusion. Modeling in blood includes both diffusion and blood viscous drag forces that cause particle convection. In blood, magnetic particles are also scattered by collisions with blood cells, which is an effect that, to a first approximation, can be modeled as additional diffusion [89].

As noted earlier, magnetic fields propagate essentially unchanged through the body and can be described by the magnetostatic equations (1)–(3). Equation (4) gives the magnetic force on each nanoparticle. For particles in blood, this magnetic force competes against viscous (Stokes) drag and creates a steady-state particle drift velocity $\vec{V}_R = c\vec{F}_{\text{mag}}$ where $c = 1/6\pi a\eta$ [232] and where η is the viscosity of blood. This relative magnetic velocity $\vec{V}_R$ acts in addition to particle convection by blood flow. In surrounding tissue, η is replaced by tissue resistance to particle motion, is an

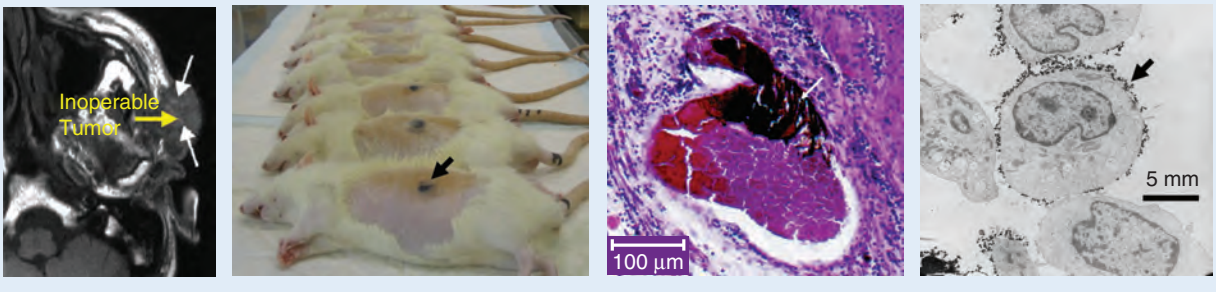

FIGURE 13 Magnetic drug targeting in animal and human clinical trials [11], [86]. Magnetic focusing was verified from the large to the small scale. (a) Magnetic resonance (MR) image of the same patient shown in Figure 2(b) after magnetic nanoparticle treatment. Nanoparticle accumulation at the inoperable tumor was observed as lighter regions (lack of MR signal) and is marked by the white arrows. (b) Rat experiments. Magnetically concentrated ferrofluid is visible under the skin of the animals. (c) Magnetic nanoparticles concentrated in a rabbit tumor microvessel (white arrow). (d) Magnetic nanoparticles at the membrane of mouse epithelial cells (black arrow) after magnetic targeting. These results combine sophisticated capabilities in nanofabrication, chemistry, imaging, animal experiments, and clinical practice [11], [17], [21], [23], [24]. The current goal is to improve the magnet control.

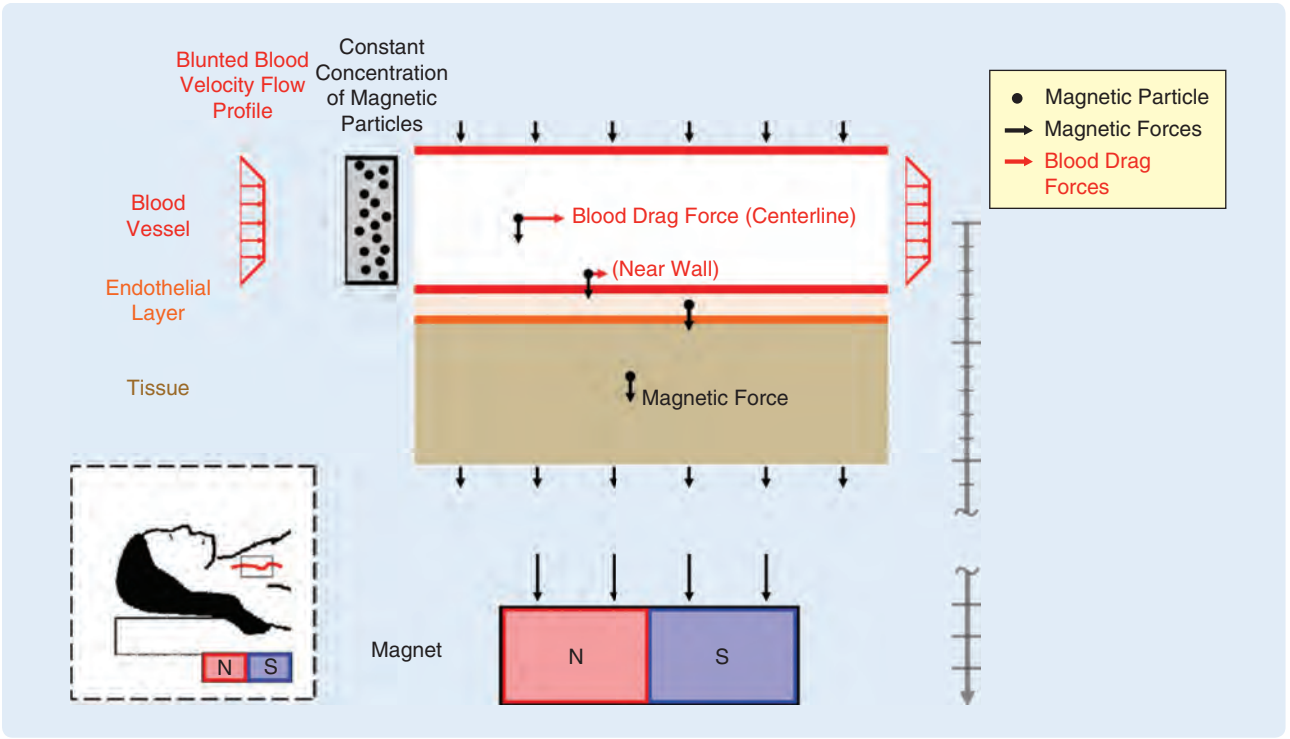

FIGURE 14 Modeling magnetic particle transport in and around a single blood vessel [88]. The blood vessel is idealized as a straight channel. Blood and a constant concentration of magnetic particles enter from the left. The magnetic particles (black circles) within the blood vessel experience diffusion, convection under blood flow, and magnetic forces. Magnetic particles in the surrounding endothelial and tissue layers experience diffusion and magnetic drift but no blood flow forces. The magnet can be a long distance from the blood vessel (deep targeting) and here this is denoted by the break in the length bar on the right of the figure. (Inset: A blood vessel in a patient and a small box showing the simulation domain.)

uncertain parameter, and varies between different tissue types (for example, muscle resists particle motion more than fat but less than bone) [110], [111], [230], [233]. In Figure 14, only two different tissue types are considered: the endothelial vessel wall and a homogeneous surrounding tissue.

The time rate of change of particle concentration at each spatial location, in blood or tissue, is given by the divergence of a ferrofluid flux [234]

$$\frac{\partial}{\partial t}C(\vec{x},t) = -\nabla\cdot\vec{J}(\vec{x},t). \tag{20}$$

Equation (20) is a particle conservation law and is exact; equations chosen for the flux $\vec{J}$ are approximate. In tissue, the flux consists of particle magnetic drift plus particle diffusion and can be modeled as $\vec{J} = -D_T\nabla C + \vec{V}_T C$ [235]. Here, $\vec{V}_T$ is the magnetically created particle velocity in tissue. Diffusion is modeled by a tissue diffusion coefficient D_T and a flux that is proportional to the negative of the particle concentration gradient ∇C. In blood, particles are also transported by blood flow so that $\vec{J} = -D_B\nabla C + (\vec{V}_B + \vec{V}_R)C$ where $\vec{V}_B$ is the blood velocity. Also in blood, particles are further scattered by collisions with blood cells. This scattering can be modeled as additional diffusion and is folded into a total blood diffusion coefficient ($D_{\text{Tot}} = D_B + D_S$) [89]. The above offers a reasonable next-step model. However, the range of possible blood and tissue parameters is wide and uncertain (see Table 1).

When the above model is nondimensionalized, all of the particle, magnetic field, blood, and tissue parameters (Table 1) collapse down to four essential quantities: the magnetic-Richardson number $\boldsymbol{\Psi}$, two reduced Renkin diffusion coefficients (one each for the endothelial membrane $\mathcal{D}$ and the surrounding tissue $\mathcal{D}_T$), and a Péclet number **Pe**. The resulting three partial differential equations (PDEs), one PDE each for particle transport in blood, the endothelial layer, and in surrounding tissue, can be written in nondimensional variables as [88], [90]

$$\frac{\partial}{\partial t}C_B = -\nabla\cdot\left[-\frac{1}{\mathbf{Pe}}\nabla C_B + (\vec{V}_B + [0,-\boldsymbol{\Psi}])C_B\right] \tag{21}$$

where C_B is the nondimensionalized particle concentration at each location in the blood vessel, $\vec{V}_B$ is the nondimensional blood velocity, t is nondimensional time, and ∇ is the nondimensional gradient operator. Since the magnet is below the vessel, the magnetic drift vector $[0,-\boldsymbol{\Psi}]$ points straight down. In the endothelial membrane and surrounding tissue

$$\begin{aligned}\frac{\partial}{\partial t}C_M &= -\nabla\cdot\mathcal{D}\left[-\frac{1}{\mathbf{Pe}}\nabla C_M + [0,-\boldsymbol{\Psi}]C_M\right],\\ \frac{\partial}{\partial t}C_T &= -\nabla\cdot\mathcal{D}_T\left[-\frac{1}{\mathbf{Pe}}\nabla C_T + [0,-\boldsymbol{\Psi}]C_T\right],\end{aligned} \tag{22}$$

where C_M and C_T are the nondimensional concentrations of particles at every spatial location in the membrane and tissue.

The magnetic-Richardson number $\boldsymbol{\Psi}$ quantifies the ratio between the applied magnetic forces and the maximum Stokes drag forces that the blood flow can exert on particles in the vessel. $\boldsymbol{\Psi}$ is defined as the ratio

$$\boldsymbol{\Psi} = \frac{\text{Magnetic Force at Blood Vessel Centerline}}{\text{Stokes Drag Force at Blood Vessel Centerline}} = \frac{\|\vec{F}_{\text{Mag}}\|}{\|\vec{F}_{\text{Stokes}}\|} = \frac{\|\vec{V}_R\|}{V_{B\max}} \tag{23}$$

where $\vec{F}_{\text{Mag}}$ is the magnetic force on a single particle at the centerline of the blood vessel [see (4)], $\vec{F}_{\text{Stokes}}$ is the Stokes drag on a stationary particle that is also at the vessel centerline, $V_{B\max}$ is the maximum blood speed in the vessel, and $\vec{V}_R = c\vec{F}_{\text{Mag}}$ is the magnetic drift velocity (as defined earlier). The Péclet number quantifies the competition between particle convection by blood flow versus particle diffusion in the blood and is defined as

$$\mathbf{Pe} = \frac{\text{Blood Vessel Width} \times \text{Maximum Blood Velocity}}{\text{Total Diffusion Coefficient of Particles}} = \frac{d_B V_{B\max}}{D_{\text{Tot}}}. \tag{24}$$

where D_{Tot} takes into account the particle scattering due to collisions with blood cells. The Renkin reduced diffusion coefficients for the endothelium and surrounding tissue are defined as

$$\mathcal{D} = \frac{\text{Diffusion Coefficient in Membrane}}{\text{Total Diffusion Coefficient in Blood}} = \frac{D_M}{D_B + D_S} = \frac{D_M}{D_{\text{Tot}}} \tag{25}$$

and

$$\mathcal{D}_{\mathcal{T}} = \frac{\text{Diffusion Coefficient in Tissue}}{\text{Total Diffusion Coefficient in Blood}} = \frac{D_T}{D_{\text{Tot}}} \tag{26}$$

where D_B is the particle diffusion in blood due to Brownian thermal motion, D_S is the additional diffusion caused by collision with blood cells, D_M is the diffusion in the endothelial membrane (which is set to zero if the particles cannot penetrate the blood vessel wall), and D_T is the particle diffusion coefficient in the surrounding tissue. Only the minimum of the two Renkin numbers needs to be considered as the smaller value determines the behavior [88]. Thus three nondimensional numbers predict nanoparticle behavior in and around a single blood vessel.

Table 1 lists relevant physiological parameters for the human body. For example, in humans, the minimum blood vessel diameter is 7 μm (for small capillaries) and the maximum is 3 cm (for the vena cava) [110], [236]. Table 1 also lists the range of engineering parameters used in past magnetic drug delivery studies. For these two ranges, the three nondimensional numbers vary between $4 \times 10^{-18} \le \boldsymbol{\Psi} \le 6 \times 10^{3}$, $1 \le \mathbf{Pe} \le 1 \times 10^{12}$, and $0 \le \min(\mathcal{D}, \mathcal{D}_T) \le 1$. In [88] the behavior of the single-vessel model (21) and (22) was exhaustively mapped over this entire nondimensional regime. For all physiological conditions—from small to large vessels with slow to fast velocities, and across all particle sizes and magnet strengths—only three types of qualitative behavior occurred: velocity-dominated behavior, magnetic-force-dominated behavior, or boundary layer formation. These three behaviors are illustrated in Figure 15.

In the velocity-dominated case, the created magnetic forces are weak compared to the blood flow forces and so cannot capture the particles, and the particles are washed to the right, out the back of the blood vessel. In the magnetic-force-dominated case, the magnetic forces far exceed the ability of the vessel membrane and tissue to resist particle motion. Here the particles are pulled down by the magnet out of the vessel and eventually also out of the region of tissue being considered. This case requires either exceedingly strong magnetic forces or a blood vessel membrane that does not substantially inhibit particle movement (such as a sufficiently "leaky" tumor vessel). In the boundary layer case, nanoparticles accumulate in a thin layer inside the vessel wall. If extravasation (the egress of particles through the blood vessel wall) is possible, these particles are in the ideal location to then enter the surrounding tissue. This last case presents the most promising possibilities as the applied magnetic field can serve to concentrate the therapeutic magnetic particles to tissue targets.

Figure 16 shows the predicted particle behavior in and around a single blood vessel [88], displaying the type of behavior expected to occur for each Richardson, Péclet, Renkin triplet. The figure shows the thin and vertical magnetic-dominated domain in solid purple at the back and the velocity-dominated domain in dark green, with the remaining space corresponding to boundary layer behavior. Parameter ranges for prior magnetic drug delivery experiments are overlaid using colored wire frames. Figure 16(a) shows the parameter range for two experiments in glass tubes [194], [107]. These two experiments did not involve any live organisms and the engineering parameters were tightly controlled, allowing for only minimal variation in the Richardson, Péclet, and Renkin numbers. In Figure 16, (b) and (c) correspond to rat experiments [86], [105], [237]. Because rats have both small and large blood vessels with varying blood velocities and their different tissue types have a range of possible diffusion and mobility coefficients, their nondimensional numbers span a broader range. Panel (d) shows the parameter range for human trials [11]. The blood velocity is higher in bigger vessels, and, unlike in rats, the relationship between vessel size and blood velocity has been measured in humans. This quantitative relation determines the curved boundary of the red Lübbe domain. Within the boundary layer regime for each animal or human

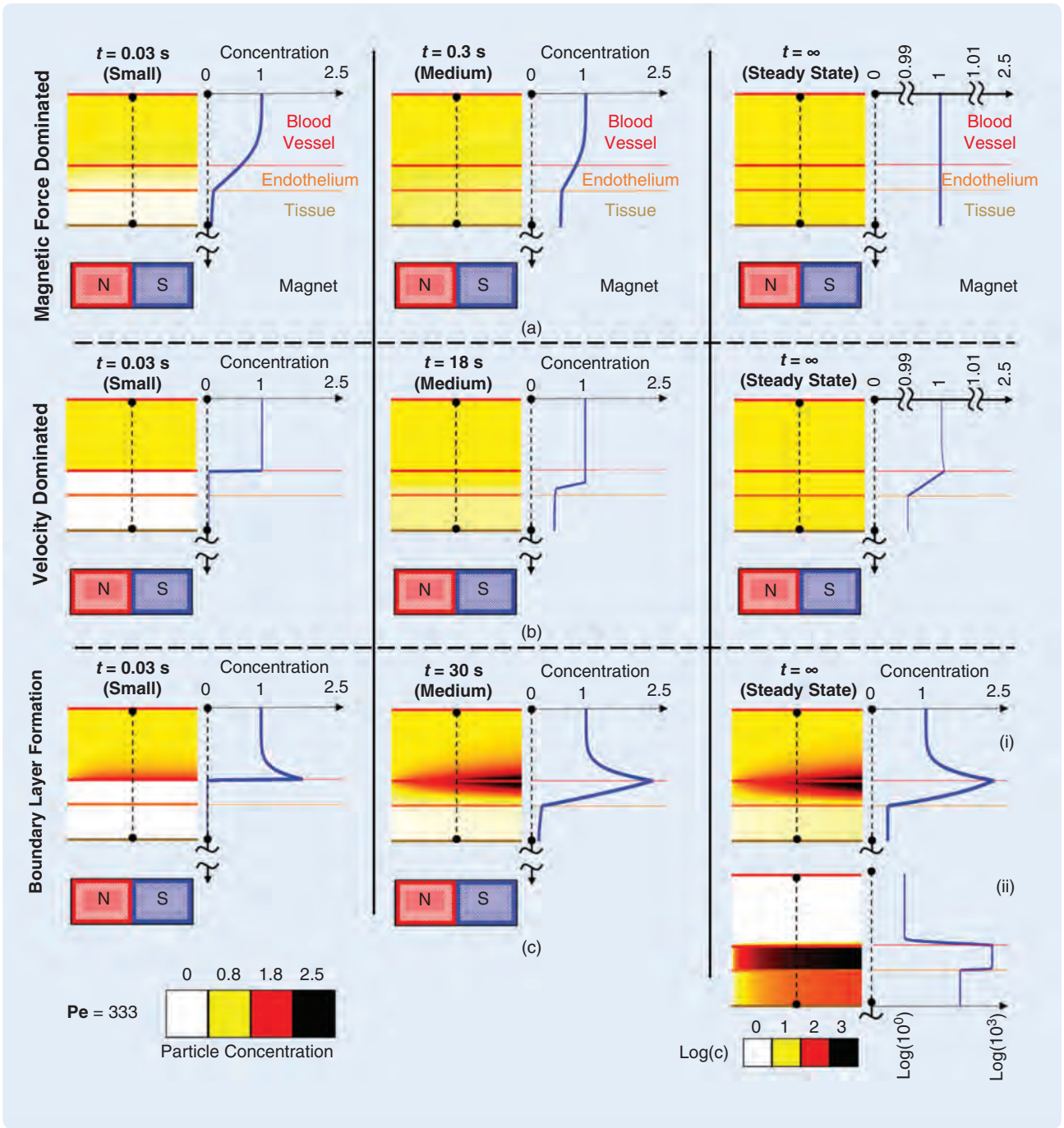

FIGURE 15 The three types of predicted behavior in and around a single vessel. (a) Magnetic force-dominated case ($\psi = 10^{-3}$, $\mathcal{D} = 1$), (b) velocity-dominated case ($\psi = 10^{-5}$, $\mathcal{D} = 10^{-3}$), and (c) boundary layer formation ($\psi = 10^{-2}$, $\mathcal{D} = 10^{-3}$). (a) The case of magnetic-force-dominated behavior shows a cross-sectional concentration of the nanoparticles for three times, at t = 0.03 s (early), 0.3 s (middle), and at equilibrium, all at **Pe** = 333. Particles are pulled towards the magnet and out through the bottom of the tissue, resulting in a final constant concentration equal to the blood inlet concentration. (b) The velocity-dominated case shows a cross-sectional concentration of the magnetic nanoparticles for three times, at t = 0.03 s (early), 18 s (middle), and at equilibrium, all at **Pe** = 333. Particles are washed out before they generate a significant boundary layer along the vessel wall. Over long times, diffusion equilibrates the concentration between tissue and blood. (c) Boundary layer formation shows a cross-sectional magnetic nanoparticle concentration for three times, at t = 0.03 s (early), 30 s (middle), and at equilibrium, all at **Pe** = 333. (i) The steady-state profile for $\psi = 10^{-2}$. Here the particle concentration is depicted on the same linear scale as in the other time snapshots. (ii) The steady-state profile for a higher magnetic-Richardson number, in this case $\psi = 10^{-1}$. Here both the particle concentration and the cross-sectional plot are shown on a log scale. In both boundary layer cases ($\psi = 10^{-2}$ and 10^{-1}), the particles rapidly build up along the vessel membrane, on both the vessel side and within the membrane. In (ii), the membrane particle concentration is sufficiently high to create a concentration in the tissue greater than the vessel inlet concentration—the magnetic targeting collects particles into the tissue around the vessel.

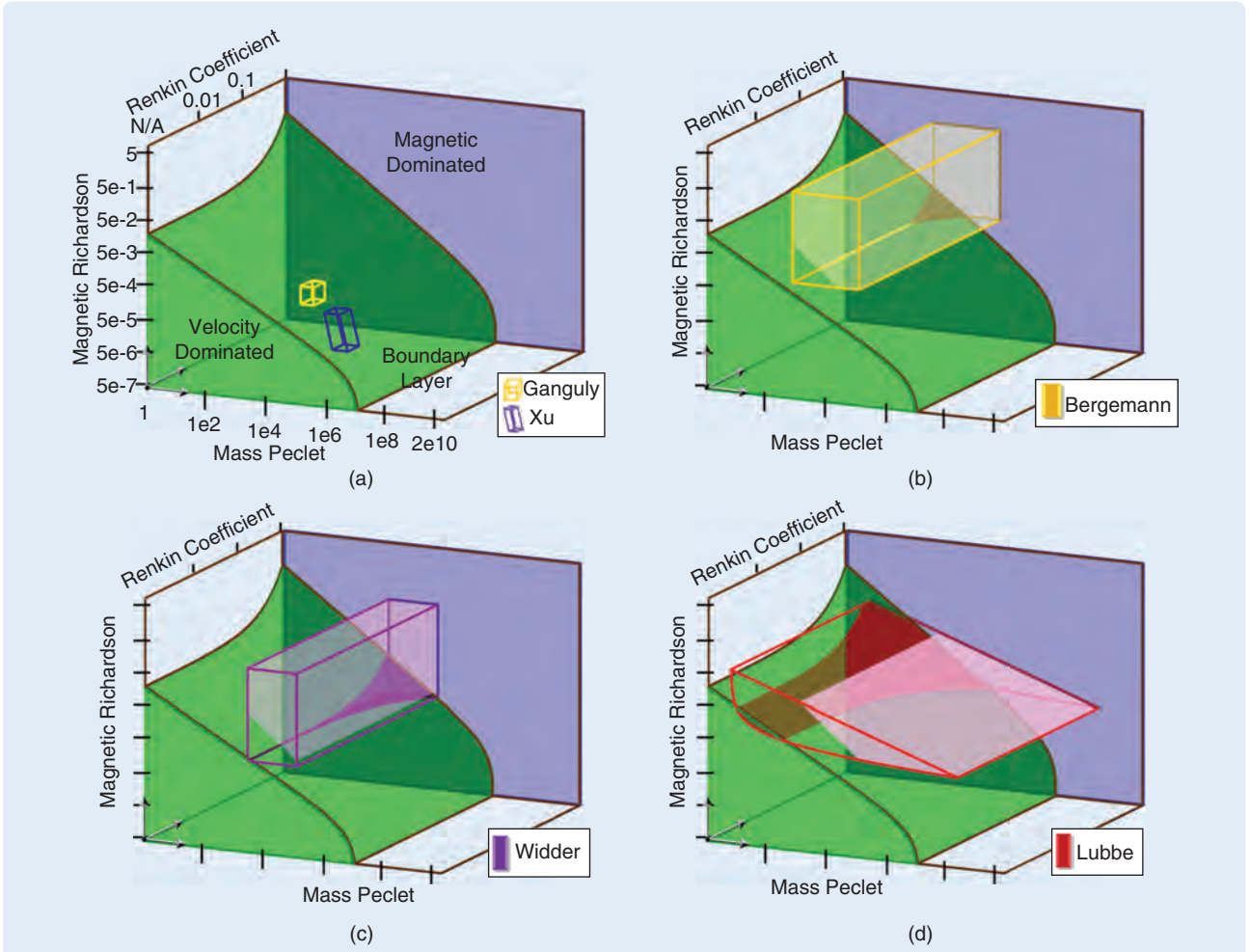

FIGURE 16 Predicted versus experimentally observed particle behavior [88]. The situation considered corresponds to Figure 14. In all the experiments, the magnetic particles are flowing down a vessel, either a glass tube as in Ganguly and Xu or through blood vessels in animals (Bergemann, Widder) or humans (Lübbe), and an external magnet is pulling on the particles. Behavior type is plotted against the three nondimensional parameters of (21) and (22): against the magnetic-Richardson number $\boldsymbol{\psi}$, the Péclet number **Pe**, and the minimum of the two Renkin numbers $\min(\mathcal{D}, \mathcal{D}_T)$. Firmly shaded regions in green and purple denote the velocity- and magnetic-force-dominated behavior domains. Specifically, the magnetic-force-dominated domain is the thin purple vertical slice at the back. The remaining space denotes boundary layer behavior. In each panel, the colored wire frame regions show the nondimensional values spanned by that experiment. Overlap dark shading [dark yellow in (b), purple in (c), and dark red in (d)] shows the region within that experiment that exists in the velocity-dominated region. Light shading [light yellow in (b), light purple in (c), and pink in (d)] shows the region of the experiments where the concentration created in the tissue around the blood vessel is greater than the vessel inlet concentration.

experiment, there are two cases: either the particle concentration in the tissue is below the blood vessel inlet concentration (as in panel c:i in Figure 15), or magnetic focusing increases the concentration in the tissue to above the vessel inlet concentration (as in panel c:ii). Figure 16 marks these second desired $C_T > 1$ cases using light yellow, purple, and pink in panels (b), (c), and (d). Readers interested in further understanding how the bounding wire frames have been computed for the in-vitro and in-vivo experiments are referred to [88] that contains all the details. Overall, Figure 16 shows the overlay between predicted and experimentally observed behavior by graphing it against the three key nondimensional numbers $\boldsymbol{\Psi}$, **Pe**, and $\min(\mathcal{D}, \mathcal{D}_T)$.

The above single-vessel analysis correctly predicts and explains available magnetic drug delivery experimental data. The PDE model of (21) and (22) accurately predicts both the occurrence and amount of magnetic particle capture in Ganguly's and Xu's glass tube experiments. Further, it resolves an open question noted by Xu [107]. A common back-of-the-envelope analysis, which compares the strength of applied magnetic forces to blood drag forces to determine if magnetic capture will or will not occur, failed to explain the experimentally observed behavior. The simple analysis was deficient because blood velocities, and hence drag forces on nanoparticles, are maximum in the center of the blood vessel. However, blood

velocities approach zero on the inside boundary of the vessel at the blood vessel walls due to wall no-slip boundary conditions [110], [235], which is shown schematically in the velocity profile at the top left of Figure 14. (The velocity profile further has a blunted shape due to the non-Newtonian properties of blood [110].) Using the centerline blood velocity to estimate the drag forces dramatically overestimates these forces near the vessel walls, and thus severely underpredicts the ability of magnetic drug targeting to capture particles. In contrast, in Figure 16, the boundary layer regime (remaining background pale blue region) first appears at $\boldsymbol{\Psi} \approx 10^{-3}$ (1e-3 on the vertical axis) even for the lowest mass Péclet number ($\mathbf{Pe} \approx 1$) where particle diffusion is highest and it is most difficult to form thin boundary layers. Thus the current analysis predicts that magnetic targeting can create a particle boundary layer even when the magnetic force is just 0.1% of the vessel centerline drag force. Simple back-of-the-envelope estimates [106], [107] also do not account for particle diffusion and particle transport in tissue, both of which are included in the current formulation.

For in vivo experiments [86], [105], the PDE model correctly predicted that the magnets used by Bergemann and Widder capture nanoparticles against blood flow in rats, again making a correct prediction in a case where the back-of-the-envelope estimate fails. The model also predicted the depth of magnetic focusing observed in Lübbe's human clinical trials [11]. For deeper blood vessels further away from the magnet, the magnetic force is smaller and the magnetic-Richardson number decreases. From Figure 16 it is possible to discern at which depths boundary layer behavior first ceases in various types of blood vessels [88]. The predicted 5-cm depth for large vessels and 8-cm focusing depth for capillaries are consistent with the extent of particle accumulation observed by MRI immediately after patient treatment (Figure 13(c) [238]).

If the same 100-nm diameter particles were actuated by a stronger and larger magnet, for example by a 2-T (MRI strength) electromagnet with a 25-cm diameter, 20-cm length, and 5-cm air core, then the analysis predicts that targeting would have been possible to a depth of 20 cm in large vessels and to a depth of 30 cm in capillaries [88]. Effective manipulation of thin boundary layers of ferrofluids at 30 cm is enough to reach deep tissue targets if control algorithms could be developed to effectively move such thin films along vessel walls through the body-filling network of human capillaries to deep tissue tumors.

Additional model features such as curved blood vessels, pulsating blood flow velocity (as actually occurs in vessels), particle clumping, and the presence of skin are discussed in [88]. These additions increase the realism of the model, which can make a quantitative difference in particle concentration profiles. However, except in the case of skin (which can force particles to accumulate underneath it), these additional factors do not change the three types of behaviors observed. Behavior remains as either magnetic-force-dominated, velocity-dominated, or the particles form a boundary layer. Still, even with the above additions, the model remains oversimplified. For example, it treats extravasation as simple diffusion. Extravasation is a complex and sometimes active process (some particles are taken up and actively transported through blood vessel wall endothelial cells) [111], [239]–[241]; research investigations are ongoing; and the physiological mechanisms that drive extravasation are not well known or characterized. Weak points of the above modeling must now be identified and rank ordered to determine which weaknesses should be addressed first to best improve the predictions and enable better magnetic drug delivery design and control. Then dedicated tissue and animal experiments must be devised to isolate, understand, measure, and fix key weaknesses. For instance, to address the large uncertainty in the model parameters, such as transport properties of nanoparticles in tissue (Table 1 provides only a rough range), experiments are under way to measure particle diffusion, magnetic mobility, and extravasation in different types of animal tissue, across blood vessel walls, and in different types of tumors.

SWEEPING METASTATIC TUMORS

Dynamic magnetic sweep, a preplanned treatment informed by blood vessel distribution data from breast cancer patient autopsies, is presented next [91]. Sweep can be implemented with just two strong magnets in open loop (Figure 17) and does not require measurement of the real-time distribution of ferrofluids in patients. As such, it will be simpler to implement than closed-loop focusing of ferrofluid to deep tumors (for which preliminary control results are presented in the next section).

The treatment of cancer is an inherently difficult and complex undertaking, and even "simple" approaches have been fraught with unanticipated challenges. As a contextual example, attaching cancer therapy to monoclonal antibodies that would recognize and preferentially bind to receptors on tumor cells initially appeared to be a relatively straightforward advance [244]–[247]. However, two decades on, this therapeutic strategy has had only minimal clinical efficacy [248]–[253] and in a rather small subset of cases. Issues of patient immune response to the murine-derived monoclonal antibodies [250], [252]–[257], difficulty in maintaining adequate therapeutic half-life in blood [252], [258], [259], and problems with the penetration of the antibodies into tumor tissue [252], [260]–[262] have all arisen as new challenges.

Further, any new medical technology that is designed or manufactured in the United States, or that is used to treat U.S. patients, must pass U.S. Food and Drug Administration (FDA) regulatory approval [263]. The FDA requires a comprehensive and detailed assessment of risks to patients, and their effective mitigation, for every hardware and software component of the technology. There is a rigorous

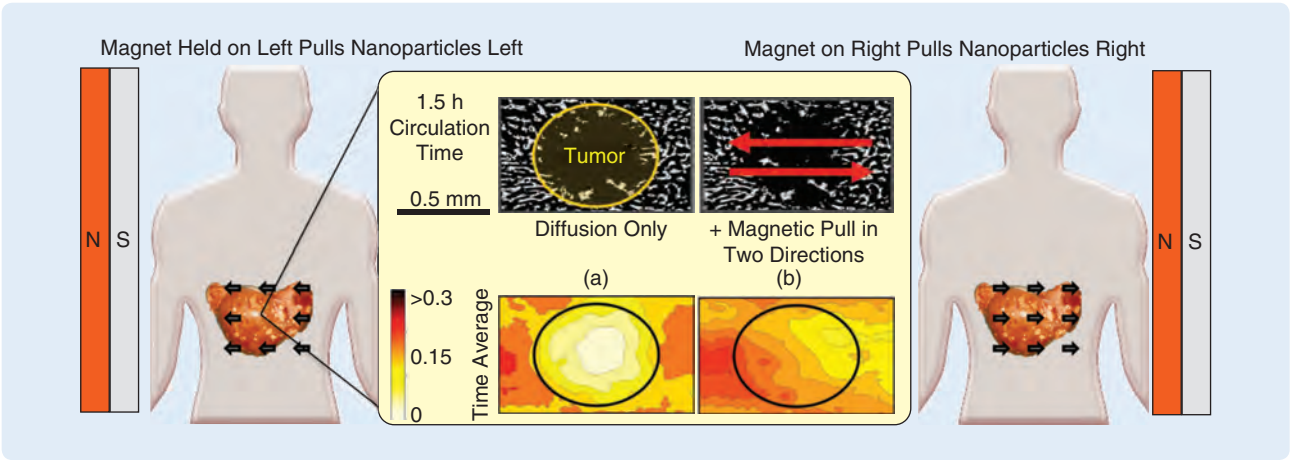

FIGURE 17 Dynamic magnetic sweep would be employed to better reach many poorly vascularized human metastases that are too small (<1 cm) to be detected by radiological means [242], [243] and whose location is therefore unknown [91]. Dynamic magnetic sweep is open-loop control and does not require real-time ferrofluid sensing. Left and right panels: magnets displace therapeutic magnetic nanoparticles from the vicinity of blood vessels into adjacent, poorly vascularized tumor regions. The process can be repeated in multiple spatial directions so that the combination of magnetic drift and particle diffusion better reaches all poorly vascularized cancer cells. Middle panel: computer simulations of the resulting drug transport in a sample 1.2-mm wide tissue region using blood vessel geometry taken from autopsy data.

framework that must be used to prove compliance, which includes requirements such as a traceability matrix for every potential fault and fail-safe in the technology [264]. More complex systems, including more complex control algorithms, face additional hurdles and hence a lengthier and more onerous path to regulatory approval. For this reason, sweep is envisioned as a magnetic treatment that could possibly reach patients earlier. Success with sweep could provide a precedent and so enable FDA approval of more complex closed-loop magnetic control treatments in the longer term.

Sweep also has the advantage that it has the potential to better treat metastatic disease. Treating the tumor shown in Figure 2(b), and its Figure 1 analog where an inoperable tumor is deep inside the body, is critical for patients where that specific tumor is causing problems (extreme pain, obstruction of the heart or breathing, pressure on the spine) [2]. However, it is metastatic disease, which is the spread of thousands of tumors throughout the body, that causes the majority of cancer deaths [265]. Moreover, metastatic tumors in humans differ from test tumors implanted into animals. A quote to this effect, by Colin Garner, CEO of Xceleron (a company that sells instruments for accelerated drug development), illustrates the point: "We have learned well how to treat cancer in mice and rats but we still can't cure people" [266]. Additionally, patients with metastatic disease are usually not operated on since it is not possible to remove thousands of widely dispersed internal tumors. Consequently, there is a lack of data on the distribution, morphology, and blood supply of human metastatic tumors. The Clinical Center at the National Institutes of Health has a unique facility that performs comprehensive autopsies on patients enrolled in their clinical trials. Using this resource, autopsy tissue sections were analyzed from breast cancer patients who died from their disease, in an attempt to better understand the path therapy must travel from blood vessels to human metastases [91].

Because breast cancer often metastasizes to the liver and there is evidence that better treatment of liver tumors can improve patient outcomes [267], the focus below is on liver metastases. Figure 18 shows a photograph of a cancerous human liver. The metastases appear as firm white nodules, in contrast to the red blood-filled surrounding tissue, indicating a poor blood supply to the tumor sites. The degree of tumor vascularization was assessed by staining thin slices of tissue to visualize the distribution of blood vessels and cell nuclei. In normal liver regions, the average distance from each cell to its nearest blood vessel was 5.3 μm (the maximum was 67.8 μm); in tumor regions, the average was observed to be 43.8 μm (the maximum was 287 μm). Poor tumor vascularization presents a problem for chemotherapy delivery. Chemotherapy injected into the blood must diffuse from blood vessels into tumors; since metastatic cells are further away from blood vessels, they are likely subjected to lower concentrations of chemotherapy, as compared to healthy cells that would receive higher doses [231], [268]. Thus poor vascularization of metastases inverts the desired outcome, causing chemotherapy to preferentially dose healthy cells rather than cancerous cells. These same poorly vascularized (and thus poorly oxygenated hypoxic) tumor cells have been linked to cancer recurrence [268].

Magnetic sweep, illustrated in Figure 17, is a concept that might be used to better treat thousands of poorly vascularized human metastases in unknown locations. Chemotherapy would be affixed to magnetic nanoparticles and would

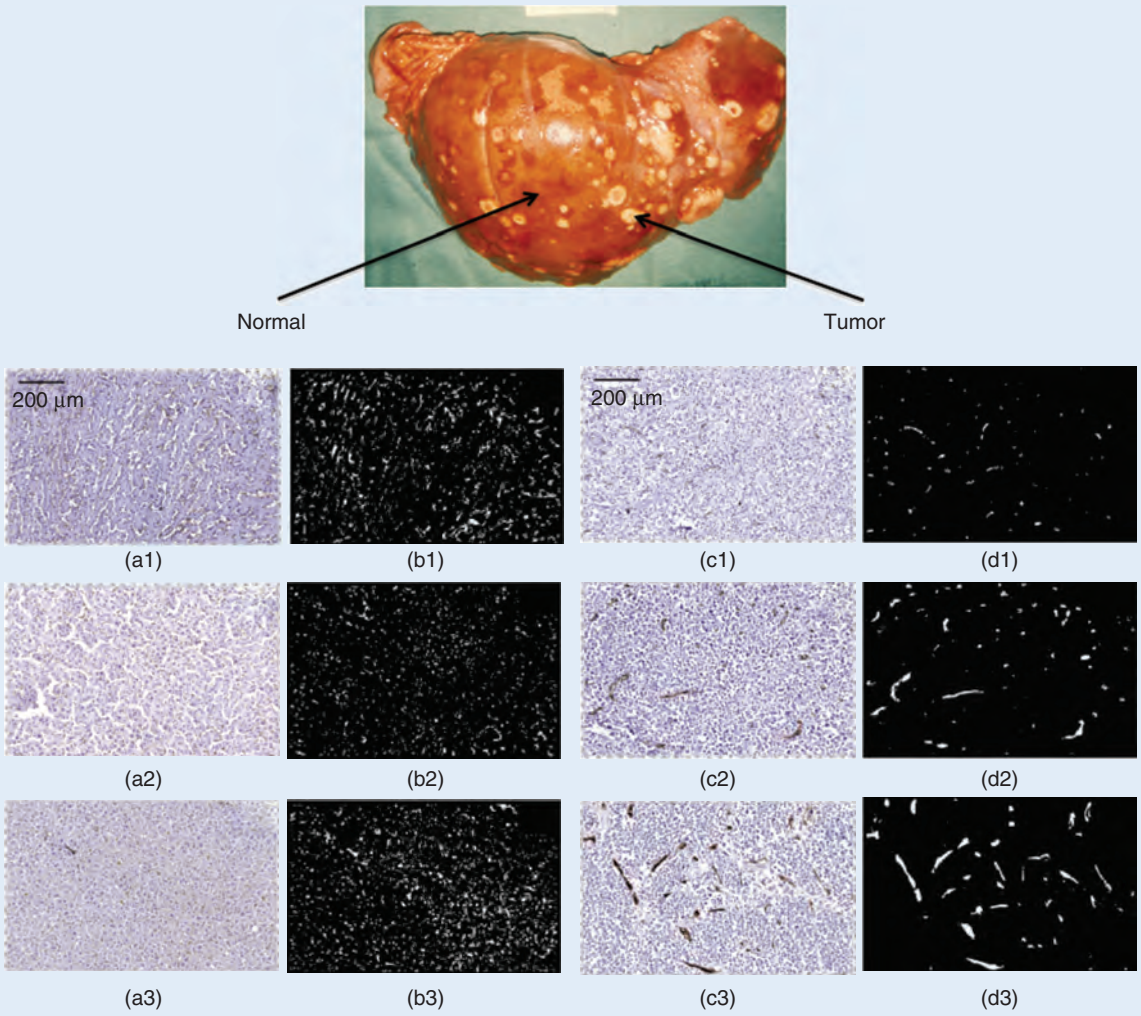

FIGURE 18 Liver metastases in breast cancer patients are poorly vascularized [91]. The top image (courtesy of Hanne Jensen and Robert D. Cardiff, University of California at Davis) shows a cancerous liver. Metastases appear as firm white nodules in contrast to the normal red blood-filled surrounding tissue. From the Clinical Center autopsies, panels (a) and (b) show thin slices of normal tissue. Each slice is 1.2-mm wide and 5-μm thick. Panels (c) and (d) show tumor slices. Blood vessels are stained dark brown, and viable cells are stained blue. In the corresponding black images the vessels are marked in white. Normal tissue displays a fine meshwork of capillaries. Tumors exhibit vessels that are larger, misshapen, further apart, and fewer in number.

be injected into the bloodstream. Magnets would then be held outside of the body to magnetically pull particles from blood vessel reservoirs into poorly vascularized hypoxic metastatic tumors. For the kind of widespread microtumors found in the livers of breast cancer patients, therapeutic particles would only have to be swept through a modest distance [$\sim$300 μm for the blood vessel distribution of Figure 18(c) and (d)]. Sweeping over much longer distances might not be necessary, as even hypoxic tumor cells that are able to survive with reduced oxygen and nutrient supply must still be sufficiently close to blood vessels to stay alive. The goal of sweeping is to reverse the current situation—where chemotherapy concentration is high in the whole body *except* at hypoxic tumors—by using magnetic forces to equalize the concentration.

When a body-length magnet is turned on or rotated into place on the left side of a patient, as shown on the left of Figure 17, it will pull all magnetic particles within every location in the body to the left. Here we consider a smaller 20-cm high by 10-cm thick, strong 5-T electromagnet that would be easier to construct than a full-body magnet, but that will suffice to pull therapy through the whole liver. The placement of the magnets ideally should be front to back, instead of left to right, to pull through the thinnest dimension of (non-obese) patients, but below we keep the discussion as left to right for simplicity and for consistency with Figure 17. The 20-cm $\times$ 10-cm magnet size creates a gradient of the magnetic field squared [$\nabla \| \vec{H} \|^2$ in the force (4)] that is nearly constant across the thickness of the liver, and the 5-T strength is in line with electromagnet

strengths that are already achieved in MRI [37], [47]. This magnet choice provides a strong and nearly uniform sweep force across the entire human liver and will move magnetized chemotherapy in basically the same way through all liver metastatic tumors. To start, a representative sample microtumor is considered 11-cm deep inside the liver. This corresponds to a deep location between two magnets positioned 20–30 cm apart, a distance that is sufficient to accommodate most non-obese patients. (As a concrete example, the corresponding author's upper abdomen is currently 18-cm thick.) Obese patients would require both larger and stronger magnets to achieve comparable sweep forces.

The model used to predict the distribution of therapy in this sample tumor is the same as in (21) and (22) except the focus now is on what happens between many vessels instead of in and around a single vessel. The spatial distribution of blood vessels is taken from sample autopsy data (here from the middle panel of Figure 17) and the boundary of each blood vessel is treated as a source of chemotherapy for surrounding normal and tumor tissue. The flux of particles through blood vessel walls and into tissue is chosen to match observed particle circulation times for the 1996 human trials [11]: it is high at the beginning and falls off exponentially with a 45-min half-life. The goal is to evaluate whether magnetic sweep can provide better therapy than diffusion alone. Because magnetic forces scale with particle volume, sweep would easily outperform diffusion for larger particles, and both diffusion and sweep are only feasible if the particles remain small enough to be able to travel through tissue [110], [111], [209]. Thus to appropriately test sweep, small 60-nm diameter particles are considered. These small particles diffuse rapidly and enable a fair comparison of whether sweep can improve upon diffusion. Such small particles can also extravasate (pass through blood vessel walls) more easily, which is another reason to consider them, although effective extravasation is less of a concern in the liver where even normal blood vessels are porous to allow the liver to filter the blood.

Based on particle size and magnet strength, realistic values are chosen for particle diffusion ($D = 9 \times 10^{-13}\,\mathrm{m}^2/\mathrm{s}$) and particle magnetic drift velocity ($V = 0.9 \times 10^{-7}\,\mathrm{m/s}$) [91]. At this velocity, it would take a magnetic particle approximately 53 min to cover the 287-μm maximum distance between a worst-case hypoxic tumor cell and its nearest blood vessel. Three cases are evaluated. For the baseline diffusion-only case, no magnetic force is applied. For the left-pull case, a constant left magnetic force is applied for the duration of the 3-h treatment. For the third bidirectional case, no magnetic force is applied for 45 min at the start (to allow a high concentration of chemotherapy to build up around each blood vessel before sweeping), then a right magnetic force is applied for 1.5 h, and finally a left magnetic force is applied for 45 min. The simulated therapy distribution results are shown in Figure 19.

These simulations indicate that magnetic sweep can improve chemotherapy concentrations in a poorly vascularized metastatic tumor. Since some drugs are fast acting, while others kill cells slowly, the time averaged (for slow-acting drugs) and maximum over time (for fast-acting drugs) concentrations were examined at each tissue location. For the diffusion-only case, both the time-averaged and the time-maximum drug concentration in the tumor was lower than in surrounding normal tissue. Single direction sweep [Figure 19(b)] improved the time-maximum drug concentration in the tumor but the average over time remained below the average in the surrounding normal tissue. Bidirectional sweep (case c) improved both the time averaged and time maximum. The tumor time average and maximum concentrations now slightly exceeded normal tissue average and maximum concentrations. Moreover, compared to diffusion-only, bidirectional sweep substantially improved the *ratio* of tumor to normal drug concentration, both averaged and maximum over time, by 86% and 89%, respectively [91].

Optimizing Sweep over Multiple Tumors and Patients

Beyond considering a single sample tumor, magnetic sweep sequences were optimized based on autopsy data across multiple tumors and patients. During sweep, there is a fundamental tradeoff; since the nanoparticles have a finite circulation time in-vivo, there is a balance between magnetically pulling in one direction for as long as possible to sweep therapy as far as possible versus applying magnetic pulls in multiple different directions to bring drugs into poorly vascularized tumors from a variety of adjacent locations. A third pull direction did not add much value, so the timing of sweep was optimized only in two opposite directions. Further, vessel distribution autopsy data is only available for deceased patients, so there is a need to choose treatment for future patients based on autopsies of similar past patients. Hence bidirectional sweep is optimized based on one set of samples (group A) and then tested on a second set of samples (group B).

The optimization metric has to be chosen with care. The goal of sweep is to normalize the distribution of therapy, so as to avoid therapy cold spots at thousands of metastatic tumors. Moreover, for a single small tissue area (for example, the 1-mm wide sample shown in Figures 17 and 19), a trained pathologist can identify the microtumor location and its extent (the yellow circle). However, it is not feasible for a pathologist to visually identify thousands of tumors per liver autopsy, and to do so over many patients. There is also a need to continue to consider both slow-acting and fast-acting therapies, for which, respectively, time-averaged and time-maximum particle concentrations are more appropriate. Thus two metrics are considered

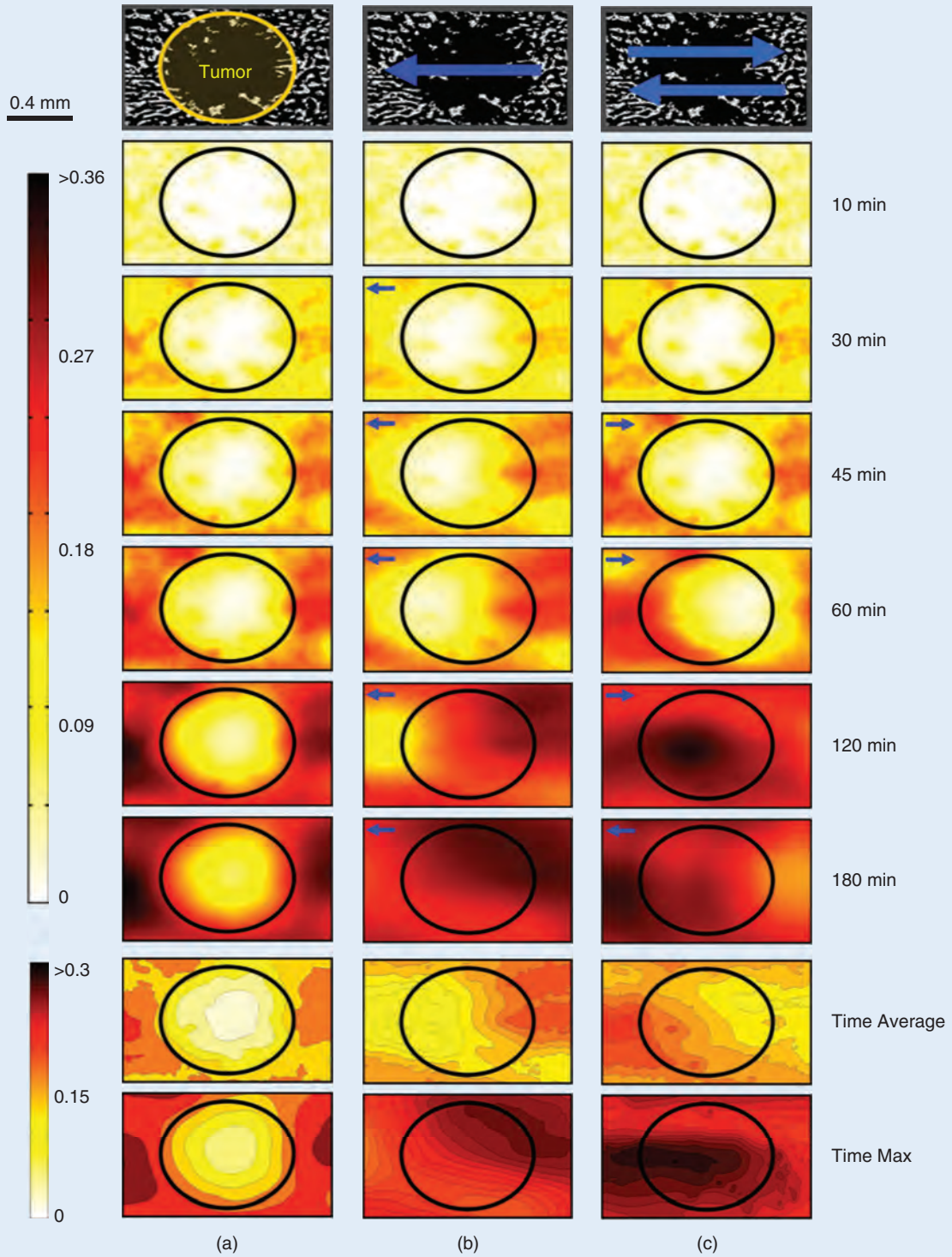

FIGURE 19 Simulation of chemotherapy distribution in and around a sample human metastases, for diffusion only compared to one- and two-directional magnetic sweep [91]. The top row shows the blood vessels (white) around a single human micro metastases (visible as a gap in blood vessel distribution), along with arrows showing the magnetic pull directions. The second panel shows the simulated chemotherapy concentration at each location in the tissue over a 3-h treatment window for (a) diffusion only, (b) a left magnetic pull only, and (c) a right then left magnetic pull. The bottom two rows show the average and maximum over time drug concentration at each tissue location. The tumor (marked by the black circle) receives both higher time average and time maximum drug concentrations for sweep compared to diffusion only. Movies are available online at www.controlofmems.umd.edu/movies/diffonly.mov, www.controlofmems.umd.edu/movies/leftpull.mov, and www.controlofmems.umd.edu/movies/bipull.mov.

$$J^{\text{time}-\text{avg}} = \frac{\text{Spatial average of the time averaged concentration}}{\text{Spatial variance of the time averaged concentration}} = \frac{\text{avg}(C^{\text{avg}-\text{time}})}{\text{std}(C^{\text{avg}-\text{time}})} \quad (27)$$

$$J^{\text{time}-\text{max}} = \frac{\text{Spatial average of the time maximum concentration}}{\text{Spatial variance of the time maximum concentration}} = \frac{\text{avg}(C^{\text{max}-\text{time}})}{\text{std}(C^{\text{max}-\text{time}})} \quad (28)$$

where the numerator is the spatial average of the nanoparticle concentration across the entire tissue slice, for either the time average or the time maximum. The denominator of the metrics penalizes high spatial variance across tissue; if the spatial standard deviation is high (if the tissue has regions of both high and low particle concentration, an undesired situation since now some tumor regions remain untreated), then the denominator is high and the metric is low. Together, the numerator and denominator try to ensure a nonzero and uniform concentration of therapy across the entire tissue. In particular, if sweep timing parameters can be chosen to create a uniform high nanoparticle concentration, then this metric will tend to infinity and sweep will have completely eliminated the problem that poorly vascularized tumors lack therapy.

The bidirectional sweep optimization considered 70 tissue samples in group A and another 71 for group B. Two parameters were optimized across group A: the duration of the first pull and the duration of the second pull. Since the treatment time was kept constant at 1.5 h, this also defined the waiting period at the start by $t_{\text{wait}} = 1.5\,\text{h} - t_{\text{first}-\text{pull}} - t_{\text{second}-\text{pull}}$. Each of the two pull durations was varied across 25 values yielding 625 simulations per tissue slice, and thus a total of 88,125 simulations. It took seven days to complete the simulations on a Core i7 2.6 GHz computer running Windows 7 with 32 GB of RAM. Figure 20 shows the fold increases in the two metrics $J^{\text{time}-\text{avg}}$ and $J^{\text{time}-\text{max}}$ versus the diffusion-only case for group A.

In (a) and (b) of Figure 20, the optimal sweep strategies for slow- and fast-acting drugs are marked by the blue stars. To increase the degree of normalization for slow-acting drugs ($J^{\text{time}-\text{avg}}$), it was best to shift in one direction for $\approx$45% of the time and then shift in the opposite direction for the remaining $\approx$55% of the time. This procedure corresponded to shifting in one direction until just before the half-life of the nanoparticles was reached, and it made no difference if the shift was to the right or left first. By comparison, to increase the degree of normalization for fast-acting drugs ($J^{\text{time}-\text{max}}$), it was best to shift the nanoparticles in only one direction—either only left or only right—for the entire duration of the 1.5-h treatment. This procedure ensured that every region of tissue saw as many new nanoparticles as possible. Bringing the particles back in the opposite direction did not improve the maximum over time. Thus, depending on whether a fast- or slow-acting therapy was considered, a different sweep strategy was optimal.

The optimums of Figure 20(a) and (b) were then tested on group B. In Figure 20(c) and (d), the histograms of $J^{\text{time}-\text{avg}}$ and $J^{\text{time}-\text{max}}$ for diffusion alone versus optimal bidirectional sweep are shown. As can be seen, the group A sweep optima effectively shift the mean of the histograms of group B to better outcomes.

The above sweep concept presents encouraging initial simulation results based on human autopsy data. The next steps entail experiments in excised animal tissue sections (currently underway) and in live animals (planned). A serious and comprehensive study is necessary to determine if and when magnetic sweep will be clinically appropriate. Although it was consistently found, across more than 100 microtumors, that liver metastases are poorly vascularized compared to normal tissue [91], the above autopsy and simulation studies were carried out on a relatively small cohort (18 breast cancer patients). More data is needed to determine effective control strategies for different scenarios so that the optimal method can be chosen according to patient profiles (e.g., an advanced breast cancer patient with liver tumors). For any live patient, the distribution of metastatic tumors and blood supply to these tumors is unknown, so sweep control strategies must be chosen for that type of cancer and disease profile based on statistical information from prior similar autopsy cases.

TOWARD MAGNETIC FOCUSING TO DEEP TUMORS

This final technical section considers control algorithms for the closed-loop control of a ferrofluid to deep targets. Compared to the previous results on static pushing into inner ears, closed-loop control of a single droplet, and dynamic but open-loop magnetic sweeping, the new aspect is control to focus a *distributed* ferrofluid. In a patient, blood flow quickly breaks up an injected bolus of ferrofluid (which is composed of magnetic nanoparticles suspended in water) and distributes it throughout the entire body (now that the nanoparticles are suspended in blood). Focusing particles to a deep location requires that the magnets take that distributed ferrofluid, concentrate it, and direct it back down to the target.

The following results are preliminary, involving only simulations in two spatial dimensions (experiments are ongoing), without accounting for human vasculature and assuming that real-time sensing of a ferrofluid is possible. As noted in Figure 1, deep and fast imaging of ferrofluids is an emerging area and is being addressed by fast-MRI [32], [269], positron emission tomography (PET) [33], [270] with fast gamma sensing [34], [35], [271], [272], as well as by a novel method that exploits the nonlinear properties of particle saturation [36], [39]–[41], [210]. The state of the art for these methods, and what remains to be done to enable in-vivo ferrofluid sensing, is summarized at the end of this section.

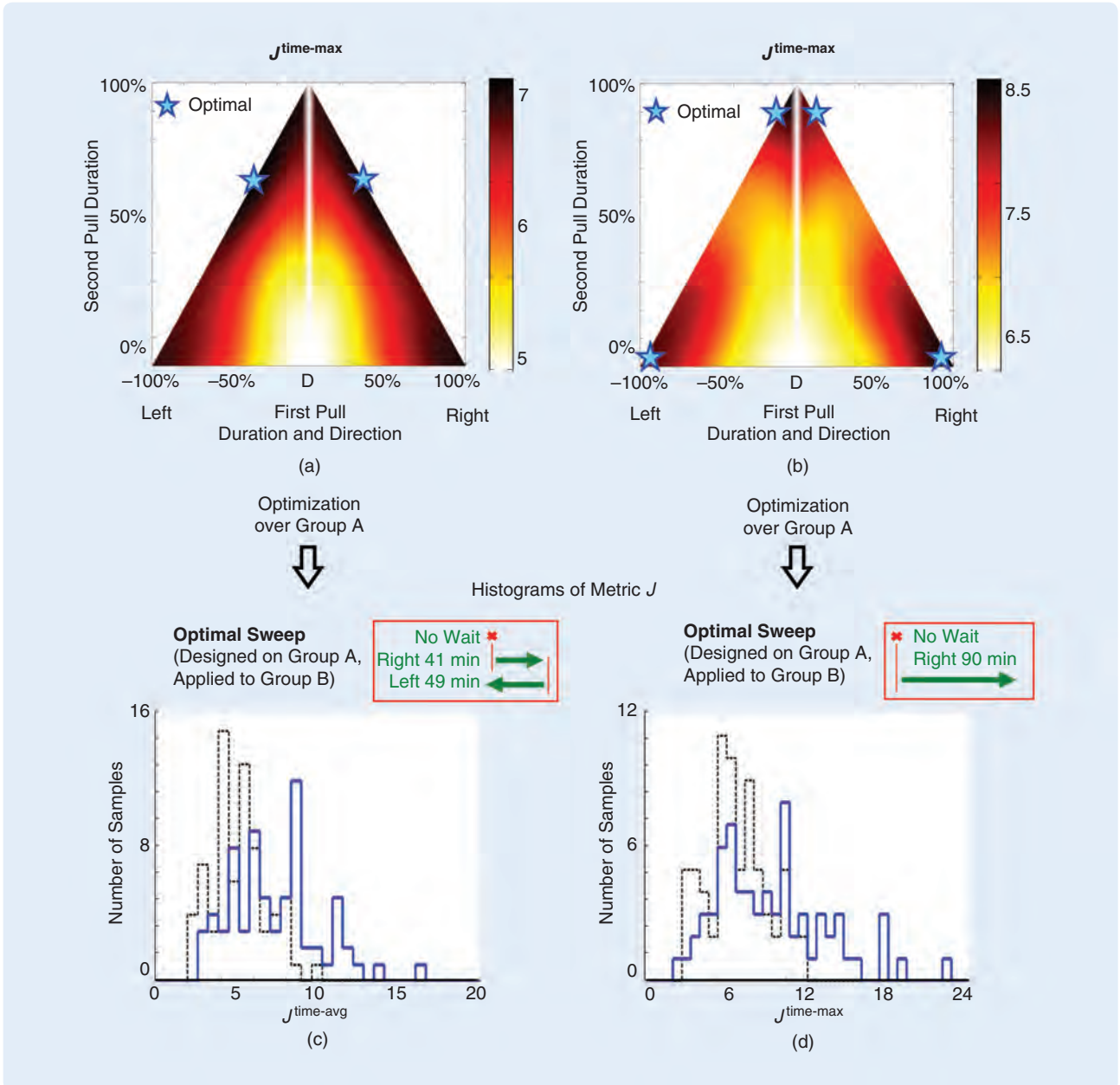

FIGURE 20 Sweep optimized over group A (first row) was then applied to group B (second row). (a), (b) Degree of nanoparticle normalization [$J^{\text{time-avg}}$ (27) and $J^{\text{time-max}}$ (28)] averaged over group A, as a function of pull left and right durations. Dark colors corresponded to high average concentrations and low spatial variances across group A tissue samples. Low values correspond to low concentrations or therapy hot and cold spots. In the triangles, the first pull duration is varied along the horizontal axis and the second along the vertical axis, with any remaining time spent waiting at the start of the treatment. For example, the location (+ 0.50, – 0.20) represents a 30% (27 min) waiting time, followed by a 50% (45 min) pull to the right, then a final 20% (18 min) pull left. Pure diffusion (no pulling) corresponds to the center white vertical axes above D. Optimal strategies are marked by the blue stars. (c), (d) Dotted black lines shows the histogram of metrics $J^{\text{time-avg}}$ and $J^{\text{time-max}}$ across group B samples for diffusion only. When the optimal sweep sequences of group A are applied to group B samples, these metrics shift to higher values as shown by the solid blue histograms in panels (c) and (d). The optimal sweep sequences are summarized within the red box at the top right of each panel: in both cases it is optimal to begin pulling immediately (there is no wait) and the pull directions and optimal durations are shown by the green arrows and text. In panel (c) the suboptimal and optimal means are 5.1 and 7.1 with a $p = 2.2 \times 10^{-7}$ (ANOVA). In panel (d) the suboptimal and optimal means are 6.3 and 8.7 with a $p = 8.4 \times 10^{-6}$ (ANOVA).

If it were possible to arrange magnets in such a way as to create a magnetic energy trap deep inside the body, that would be the easiest solution; such a trap could capture particles every time they flow by, it could be shifted to focus chemotherapy to tumors in different locations, and it could be slowly scanned to treat a single large tumor. This approach would constitute an open-loop solution, and would not require ferrofluid sensing. However, Earnshaw's

Samuel Earnshaw's 1839 Theorem

Samuel Earnshaw's result on "the nature of molecular forces which regulate the constitution of the luminiferous ether" (available in Google books) was read to the Cambridge Philosophical Society in March 1839 but was not printed until 1842 [273]. The result considers particles attracted to each other by an inverse square law and proves that "instability cannot be removed by arrangement (of the particles); for though the values of d_f^2V, d_g^2V, d_h^2V depend upon the arrangement of the particles, the fact that one at least must be positive and one negative depends only upon the equation $d_f^2V + d_g^2V + d_h^2V = 0$, which is true for every arrangement. And consequently, whether the particles be arranged in cubical forms, or in any other manner, there will always exist a direction of instability." Earnshaw's function V is the potential energy of a single particle being attracted by many others. The proof proceeds by showing that the equation for V is "that of an hyperboloid" (a saddle), with the result that the sum of its three second derivatives must equal zero. Even if two derivatives are negative (corresponding to particle stability in a plane), the third derivative must then be positive (instability along a line).

Earnshaw's result equally applies to nanoparticles in a magnetic field. Although nanoparticles do not attract each other strongly, the potential energy created by an imposed magnetic field is also, at best, an energy saddle. It is not possible to create an energy well between magnets, no matter how they are arranged.

A modern proof proceeds as follows: the force on a single particle is given by $\vec{F} = \kappa \nabla \| \vec{H} \|^2$ [the coefficient $\kappa = 2\pi a^3 \mu_0 \chi / (3 + \chi)$ by (4)]. The corresponding potential energy for the ferromagnetic particle is $U = -\kappa \| \vec{H} \|^2$ since force is minus the gradient of the potential energy [196]. The Laplacian of the energy is

$$\begin{aligned} \nabla^2 U &= \frac{\partial^2 U}{\partial x^2} + \frac{\partial^2 U}{\partial y^2} + \frac{\partial^2 U}{\partial z^2} \\ &= -\kappa \nabla^2 \| \vec{H} \|^2 = -\kappa \nabla^2 (H_x^2 + H_y^2 + H_z^2) \\ &= -2\kappa (\| \nabla H_x \|^2 + \| \nabla H_y \|^2 + \| \nabla H_z \|^2 \\ &\quad + H_x \nabla^2 H_x + H_y \nabla^2 H_y + H_z \nabla^2 H_z). \end{aligned} \tag{S1}$$

Between magnets, where there are no applied electric currents, by Maxwell's equations both the divergence and the curl of the magnetic field are always zero. This result implies that the Laplacians of the individual components of the magnetic field are zero: $\nabla^2 H_x = \nabla^2 H_y = \nabla^2 H_z = 0$. For ferromagnetic particles $\kappa > 0$ so

$$\nabla^2 U = -2\kappa (\| \nabla H_x \|^2 + \| \nabla H_y \|^2 + \| \nabla H_z \|^2) \leq 0 \tag{S2}$$

because the term in parentheses is the sum of squares and is thus always positive. It is not possible to create a magnetic potential energy well, as this would require a positive energy curvature $\nabla^2 U > 0$ that would violate Maxwell's equations.

This result has implications for magnetic drug delivery; no arrangement of magnets can create an energy well between them to focus ferromagnetic particles to an interior target. Diamagnetic particles with $\kappa < 0$ could be focused, in principle, but diamagnetism is six orders of magnitude weaker than ferromagnetism ($\chi \approx -10^{-5}$ instead of $+20$), and the forces created would be too tiny to move particles against tissue or blood resistance. Even if sufficient forces could be created on diamagnetic particles, as mentioned in the text, the susceptibility of human tissue is similar to that of diamagnetic materials in particles ($|\chi_{\text{tissue}}| \approx 10^{-6} - 10^{-4}$ [21]), but its volume is far greater; thus the tissue would experience orders of magnitude greater forces than diamagnetic nanoparticles, which would harm patients. Finally, most diamagnetic materials (bismuth, lead, mercury) are poisonous if injected into people. Thus Earnshaw's 1839 theorem, which shows that no static magnetic field can focus ferromagnetic particles to an interior target, remains a key and fundamental limitation for magnetic drug targeting. The solution is to bypass the assumptions of the theorem, for example, by introducing feedback control and varying the magnetic fields in time and space to control ferrofluid dynamics.

theorem [273] (see "Samuel Earnshaw's 1839 Theorem") proves that it is not possible to create such a stable magnetic energy trap between external magnets.

The simplicity and fundamental nature of Earnshaw's theorem makes it hard to bypass. Starting from Maxwell's equations, Earnshaw's theorem proves that the potential energy created by any arrangement of magnets cannot be concave; a stable energy well cannot be made. Any straightforward temporal averaging operation, such as applying a fast sequence of different magnetic fields or rotating an energy saddle, fails to bypass the theorem due to linearity. If $U_1(x, y, z)$, $U_2(x, y, z), \ldots, U_n(x, y, z)$ are the sequence of applied magnetic energies, then the curvature of the time-averaged magnetic energy $\nabla^2 U = (1/n)(\nabla^2 U_1 + \nabla^2 U_2 + \cdots + \nabla^2 U_n) \leq 0$ because each U_i satisfies Earnshaw's theorem. Creating a magnetic energy that is flat to second order but is convex in fourth and higher order derivatives has not been achieved. Even if this were possible, such a solution would create magnetic forces that are too weak for effective particle manipulation, would require precision cancellation of strong magnetic fields and would likely be too fragile and sensitive for practical engineering implementation. Another idea is to exploit a strong physical nonlinearity, such as

particle magnetization saturation. But Earnshaw's theorem can be extended to show that the saturated magnetic energy also cannot have positive curvature. In principle, it is possible to exploit single-particle magnetization and rotation dynamics, that is, applying a magnetic field to magnetize the particles in one direction and then quickly switching the field so that the individual particles do not have time to realign, which means the particles will be briefly opposed to the new field and hence will act diamagnetically. This strategy flips the sign of the magnetic energy and makes a positive curvature possible. Using this idea, it may be possible to create a deep magnetic trap on average. But even microsecond switching of strong magnetic fields by pulsed-power electromagnets [32] might not be fast enough, the physics of magnetic particles under quickly changing magnetic fields is complex [22], [274]–[276] so additional unanticipated forces may arise, and this concept has not been tested in experiments. There may be some other clever and practical open-loop strategy to create a deep and stable magnetic trap, but such a strategy has not yet been found. In the meantime, feedback control, which exploits both sensing and the transport dynamics of the ferrofluid as a whole, is investigated as a method to focus particles to a deep target on average.

Consider the same experiment as shown in Figure 8 but now, instead of a single droplet, the ferrofluid is distributed throughout the petri dish with a concentration $C(x, y, t)$ at each location over time. The partial differential equation for this situation is an analog of (21), minus the blood convection term (which will need to be put back in for future control design). This equation is rewritten below in a form that highlights that the magnetic force on the ferrofluid is equal to the gradient of the square of the magnetic field intensity

$$\frac{\partial}{\partial t}C(x, y, t) = -\nabla\cdot\Big[-\frac{1}{\mathbf{Pe}}\nabla C(x, y, t) + \Psi C(x, y, t)\nabla\|\vec{H}(x, y, t)\|^2\Big]. \tag{29}$$

As before, the controlled electromagnets are placed outside the petri dish. The goal is to control these magnets to create a high ferrofluid concentration at the center of the dish. The larger purpose is to learn something about control algorithm design for a distributed ferrofluid.

By-Hand Control Design Via Shaping a Sequence of Magnetic Energies

Initially, it was not clear how to think about control design to focus a distributed ferrofluid to a deep target. To see if such focusing was even possible, a control algorithm was first designed by hand. Using an intuitive understanding of magnetic energies and forces, and Earnshaw's constraints on their shapes, a succession of magnetic energies $U_i = -\kappa\|\vec{H}\|^2$ was chosen to drive a ferrofluid from domain edge to center with minimal spreading [102]. The by-hand control was able to create a ferrofluid hot-spot on-average at the center of the domain and indicated how to phrase a rigorous optimization problem for deep focusing (whose quadratic programming solution is presented in the next subsection). This by-hand approach was "semi" closed-loop in the sense that each magnetic energy shape was chosen by knowing the ferrofluid distribution created by the previous shaped energy (see Figure 21), and it was instructive by building intuition on what kind of magnetic focusing actions are possible.

The focusing control was carried out in two steps: first the ferrofluid was focused to the edge of the circular domain and then it was moved with minimal spreading to the center target [102]. The first step sidesteps Earnshaw's theorem by using the petri dish boundary to contain the ferrofluid. The second step tries to do the best possible under the $\nabla^2 U \le 0$ curvature constraint. This strategy, when repeated multiple times will, on average, create a higher concentration of ferrofluid at the center, and at some edge locations, but with a lower concentration within the remainder of the domain. In a patient, this would correspond to increased chemotherapy concentration at the deep tumor and in some locations under the skin, but it would reduce chemotherapy in the interior of the body (in the lungs, liver, other internal organs, and would spare more of the patient's immune system).

To show what happens without closed-loop control of magnets, Figure 21(a) [102] first shows the response of the ferrofluid to a single magnet that is switched on and left on. The simulation begins with a uniform ferrofluid concentration $C(x, y, 0) = 1$. Ferrofluid flows down the energy surface $U = -\kappa\|\vec{H}\|^2$ (shown in panel a:i) and accumulates at the $\|\vec{H}\|^2$ maximum, collecting as closely as possible to the turned-on magnet. If all eight magnets were switched on and left on, the ferrofluid would collect at eight spots nearest to the eight magnets. This switching would create a transient hot spot at the center since fluid there would be removed last. However, creating such a "focus" by depleting ferrofluid everywhere else is not a viable in-vivo targeting approach since blood flow would quickly wash away this remaining region of the ferrofluid. The control strategy illustrated next actively moves ferrofluid to the center target.

Figure 21(b) illustrates the two-step "edge then move in" energy-shaping control algorithm. Again the simulation starts with $C(x, y, 0) = 1$. Magnets are numbered 1–8, starting with the rightmost magnet and proceeding counterclockwise. At time $t = 0$, the y-axis magnets (third and seventh) are turned on in the same direction with unit strength, which creates the highest magnetic field along the y-axis, and along this axis the field is greatest nearest the two activated magnets. The resulting magnetic energy surface is a saddle, as shown in panel b:i bottom. The ferrofluid, which is uniformly distributed at time zero, flows

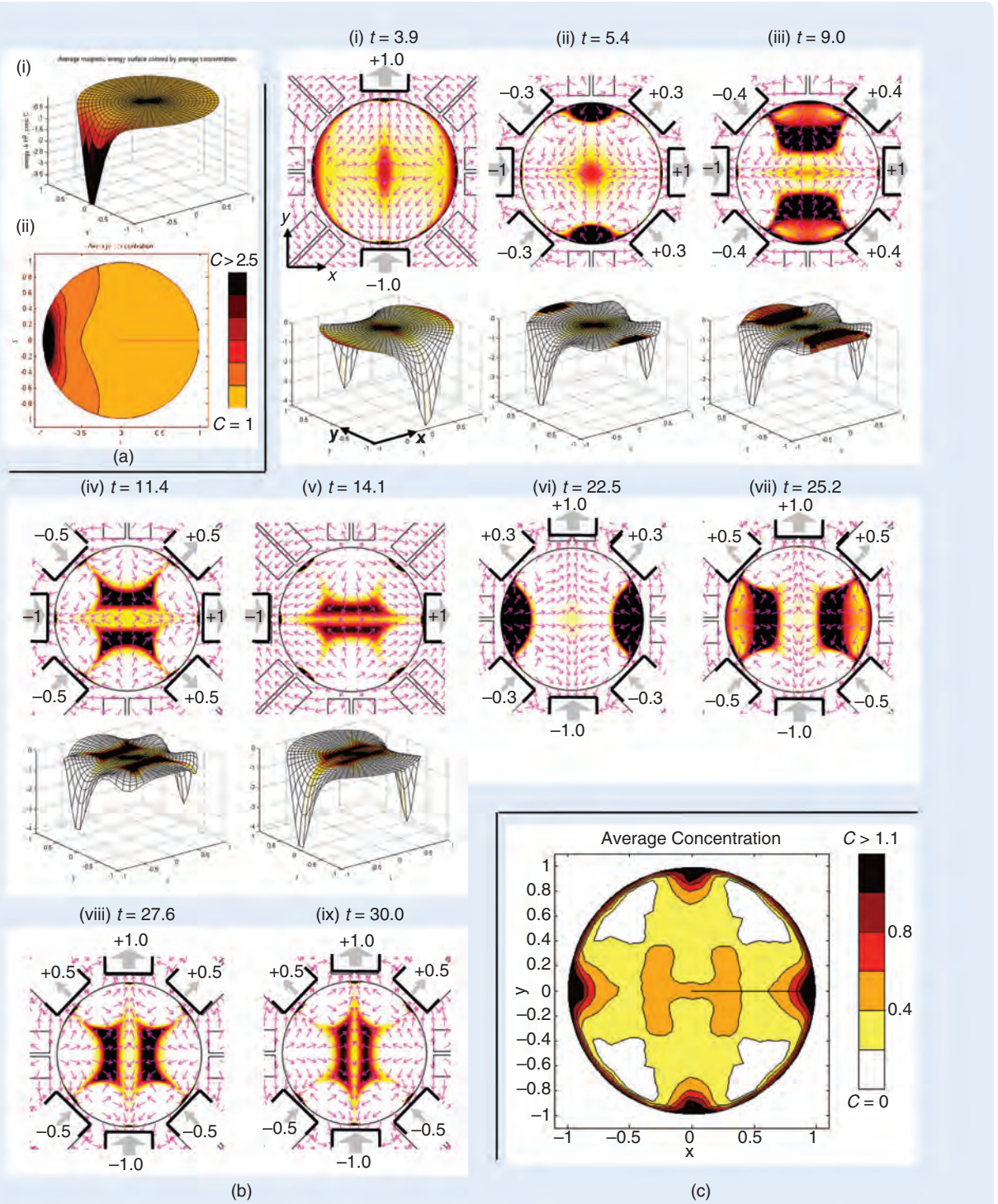

FIGURE 21 Initial dynamic magnet control to focus ferrofluid to a center target on average [102]. (a) Constant actuation: ferrofluid concentration due to turning on the fifth (far left) magnet. (i) The magnetic energy surface $U = -\kappa \|\tilde{H}\|^2$ is plotted along the z axis to show ferrofluid flowing downhill along the force directions $F = -\nabla U$ with the resulting averaged ferrofluid concentration shown by the coloring here and in subpanel (ii). (b) Dynamic focusing control: magnets are now turned on and off to direct ferrofluid to the center. The first five subpanels show ferrofluid concentration and magnetic actuation with the corresponding magnetic energy surfaces. Energy surfaces for the last four panels (not shown) are 90° flips of the panels shown. Coloring denotes ferrofluid concentration [the scale bar is the same as in (c)]. Switched-on magnets are marked by heavy black lines with weighted thick gray arrows and numbering showing magnet strength and orientation. A positive outward polarity corresponds to a counterclockwise electrical current. Thin pink arrows (normalized to unit length) show magnetic force directions that match the gradients of the magnetic energy surfaces (forces point down the surfaces). (c) The resulting time-averaged ferrofluid concentration. Note the on-average hot spot at the center. The movie is available online at www.controlofmems.umd.edu/movies/sim-distcontrol.mov.

down this energy saddle, forms a transient hot spot at the center (where depletion is slowest), and collects near the two activated magnets (the resulting distribution is shown at time $t = 3.9$).

After focusing the particles at the edges, there is the challenge of moving the ferrofluid from near the two y-axis magnets toward the center. To do so, at time $t = 4$, the eight magnets are switched to the values $u = [+1, +0.3, 0, -0.3, -1, -0.3, 0, +0.3]$ as shown in panel b:ii. The extra $|0.3|$ values of magnets 2, 4, 6, and 8 create two locally unstable points (energy maxima) along the y-axis just outside the ferrofluid hot spots (see the force arrow sources in panel b:ii adjacent to magnets 3 and 7). This switching causes the ferrofluid to spill down the energy surface toward the center target.

The ferrofluid continues to move in along the y-axis, but by $t = 9$ a significant amount of spreading out along the x direction, toward magnets 1 and 5, becomes apparent. This spreading is due to the modest negative curvature of the energy surface in the x direction at the location of the two ferrofluid hot spots (see the energy curvature underneath the black regions in panel b:iii). To combat this unfavorable curvature, magnets 2, 4, 6, and 8 are turned on to higher values (this switch from $|0.3|$ to $|0.5|$ happens smoothly from $t = 8.9$ up to $t = 9.1$), flattening out the energy surface in x somewhat (panel b:iv) and limiting further spread in x while continuing to drive the fluid in along y.

By $t = 14.1$, the ferrofluid hot spots have reached the center target but have spread out significantly along x. At this point, it is no longer feasible to continue effectively moving the hot spots to the center, so ferrofluid is refocused next to magnets 1 and 5 by activating these two magnets at $t = 14$, which concentrates the ferrofluid to the edges again. The move-to-center sequence then repeats, but now in the x direction: it places energy saddles outside the ferrofluid foci to drive them back in toward the center at $t = 20$, flattening the energy surface in the y direction at $t = 25$ to limit spreading in the y direction. The results, both in terms of ferrofluid concentration and the energy surfaces (not shown), are 90° flips of those already shown in the y direction. As this bring-to-edges then move-to-center sequence repeats, the control scheme continually drives ferrofluid through the center to create a mild hot spot on average at the central target [as shown in panel (c)]. A tighter hot spot result is shown next and is achieved by phrasing and solving a quadratic optimization.

Control Design by Semidefinite Quadratic Programming

Focusing of ferrofluid to the center is again achieved by first collecting ferrofluid to the edge of the domain, then moving it to the center with minimal spreading, and repeating this sequence multiple times to create a deep hot spot on average. The difference is that now the move-to-center stage is optimized by semidefinite quadratic programming [277], [278] instead of being chosen by intuition. The need for semidefinite quadratic programing arises naturally: the governing equations are quadratic in the magnetic actuation [from (29) to (33) and (34)] and the matrices within the quadratic forms (35)–(37) can be indefinite. Also, one hot spot is moved to center at a time, as opposed to two at once as in Figure 21. This approach allows all eight magnets to coordinate to move and shape just one ferrofluid bolus, instead of having to symmetrically move in two spots at once, and enables a higher averaged concentration at the target. As previously, the simulation begins with $C(x, y, 0) = 1$. The central target $\|\vec{r}\| \le 0.2$ is marked by the dashed blue circle in the first panel of Figure 22(a), and the goal is to choose magnet actuations to maximize the concentration of ferrofluid in this target area on-average: $\max (1/T) \int_0^T \int_{\|\vec{r}\| \le 0.2} C(\vec{r}, t)\, d\vec{r} dt$.

The first task is to focus the ferrofluid to the domain edge using magnet control. To do so, a single magnet is turned on with all others turned off and is left on until 99% of the ferrofluid has collected to within a 0.03 distance of the edge. The result of this first collection stage is shown in the first row (phase I) of Figure 22(a).

The next task is to move the edge hot spot to the center with minimal spreading [195]. Define the location (center of mass) and the spread (covariance matrix) of the ferrofluid by

$$\vec{r}_{cm}(t) \triangleq \int_\Omega \vec{r} C(\vec{r}, t) d\vec{r}, \tag{30}$$

$$\Sigma(t) \triangleq \int_\Omega (\vec{r} - \vec{r}_{cm}(t))(\vec{r} - \vec{r}_{cm}(t))^T C(\vec{r}, t) d\vec{r} \tag{31}$$

where $\vec{r} = (x, y)$, $\Omega = \{\|\vec{r}\| \le 1\}$ is the circular domain, and, as before, $C(\vec{r}, t)$ is the ferrofluid concentration in space and time. The trace of the covariance matrix is used as a measure for the size of the ferrofluid spot. Since the move-to-center step must be carried out with minimal spreading, but should also be completed as quickly as possible to minimize time-averaged ferrofluid concentrations outside the central target region, the optimization cost is defined as

$$J = \text{trace}\{\Sigma(t_f)\} + \beta t_f \tag{32}$$

where t_f is the length of time it takes to complete the step, $\beta > 0$ is a constant, and the term βt_f penalizes the time taken to complete the move. The control task is to choose the magnet control currents $\vec{u}(t) = [u_1(t), u_2(t), \ldots, u_8(t)]$ to minimize J under the constraints that the center of mass $\vec{r}_{cm}$ moves from edge to center and the magnet actuations remain bounded by $\|\vec{u}\|_2 \le 1$. Here the 2-norm is used instead of the prior infinity norm ($|u_i| \le 1$ for $i = 1, 2, \ldots, 8$) because the 2-norm leads to a known quadratic program that can be solved by the methods in [100] and any actuation that lies within the unit sphere $\|\vec{u}\|_2 \le 1$ also falls within the infinity-norm unit cube $\|\vec{u}\|_\infty \le 1$. The optimization method below will be extended to directly handle the infinity norm in the future.

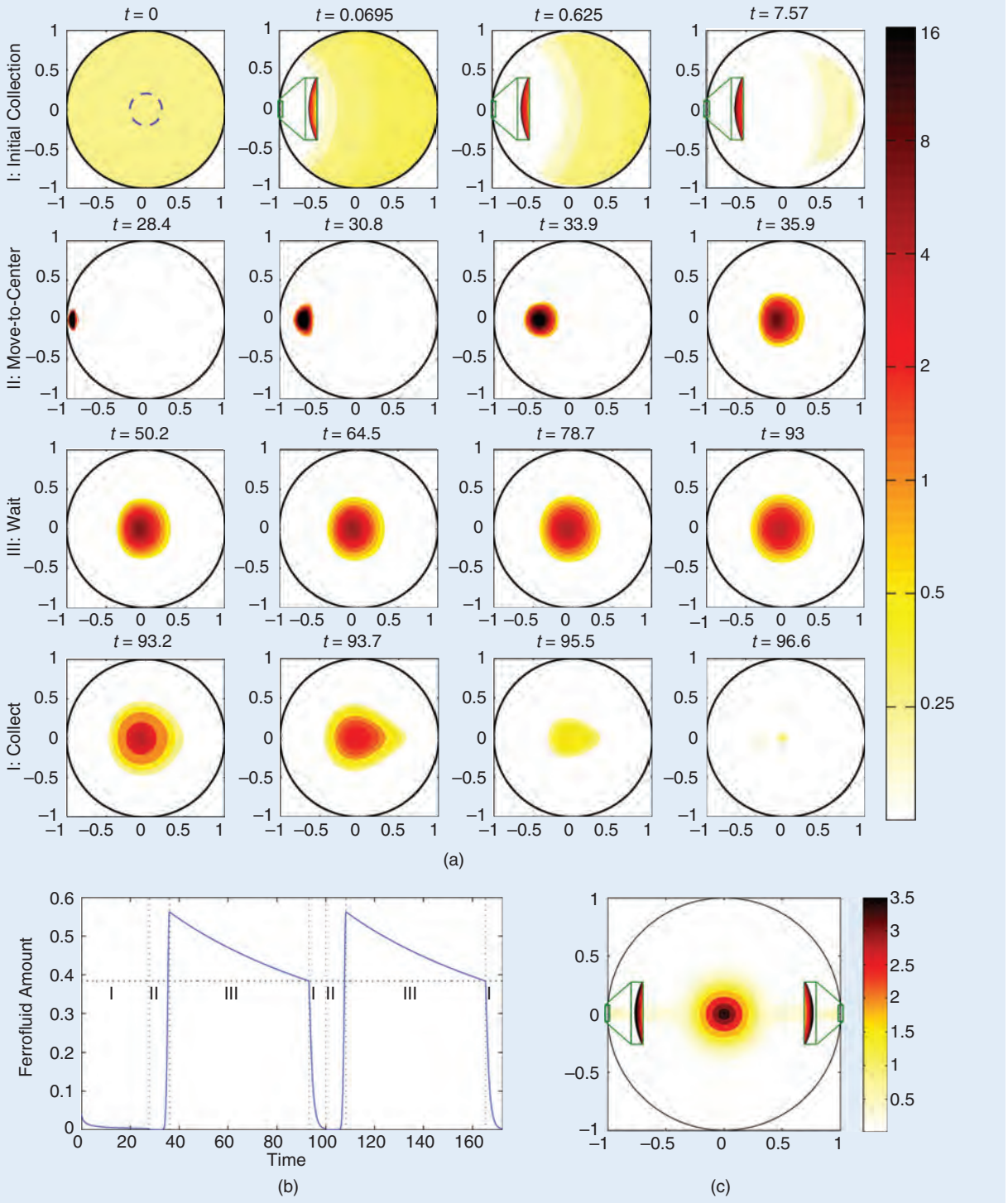

FIGURE 22 Quadratic programming optimization of ferrofluid focusing to a deep target on average. (a) The concentration of the ferrofluid in space for a sequence of times. The central target is marked by the dashed blue circle in the first panel. Phase I: Initial collection of the ferrofluid to the left edge. The action of the left turned-on magnet depletes ferrofluid from the domain interior and collects it at the edge, as shown by the three zooms in the second, third, and fourth panels. Phase II: Control of the ferrofluid to center with minimal spreading. Phase III: A waiting step, the ferrofluid begins to diffuse back out. Phase I again: Collection of the ferrofluid to a new edge location. Phases II and III were optimized individually while step I (the collection phase) has not been optimized yet. (b) The amount of ferrofluid inside the $\|\vec{r}\| \leq 0.2$ target at each time. (c) The average concentration across two full cycles (across phases I, II, and III repeated twice). Notice the different color scale. The movie is available online at www.controlofmems.umd.edu/movies/opt-distcontrol.mov.

As for control of a single droplet (Figures 10 and 11), a mapping is constructed from magnet actuation to the ferrofluid metrics—here from $\vec{u}(t)$ to the time rate of change of $\vec{r}_{cm}(t)$ and the trace of $\Sigma(t)$. Since the center of mass and covariance are linear functions of the ferrofluid concentration C by (30) and (31), and the magnetic field still appears quadratically in the ferrofluid dynamics and depends linearly on the magnet actuations [(29) and the eight magnet analog of (6)], the map $\vec{u}(t) \mapsto [(d/dt)(\vec{r}_{cm}, \text{trace}\,\Sigma)]$ is quadratic in $\vec{u}$. Substituting this map into the cost J, nondimensionalizing, working through the integrals and transforming variables, leads to a quadratic program [195]

$$\min_{\vec{\xi}} \ \vec{\xi}^T \mathbf{W}(t) \vec{\xi} \tag{33}$$

$$\text{subject to:} \ \left[\vec{\xi}^T \mathbf{Q}_x(t)\vec{\xi} \quad \vec{\xi}^T \mathbf{Q}_y(t)\vec{\xi}\right]^T = (\vec{r}_i - \vec{r}_f)/\|\vec{r}_i - \vec{r}_f\| \tag{34}$$

where the ferrofluid is constrained to move from its initial edge location $\vec{r}_i$ to the final center target $\vec{r}_f$ along a straight line. The $\vec{\xi}^*$ that achieves this motion with minimal spreading is rescaled to yield the magnet control $\vec{u}^* = \vec{\xi}^*/\|\vec{\xi}^*\|$ that creates this motion as fast as possible but still meets the magnet actuation $\|\vec{u}\| \le 1$ constraints. The matrices $\mathbf{W}$, $\mathbf{Q}_x$, and $\mathbf{Q}_y$ are given by

$$\mathbf{W}(t) = \int_\Omega ([x - x_{cm}(t)]\mathbf{P}_x(\vec{r}) + [y - y_{cm}(t)]\mathbf{P}_y(\vec{r}))C(\vec{r}, t)d\vec{r} + \left[\frac{2}{\mathbf{Pe}\Psi} + \frac{\beta}{2\Psi}\right]\mathbf{I} \tag{35}$$

$$\mathbf{Q}_x(t) = \int_\Omega \Psi \mathbf{P}_x(\vec{r})C(\vec{r}, t)d\vec{r} \tag{36}$$

$$\mathbf{Q}_y(t) = \int_\Omega \Psi \mathbf{P}_y(\vec{r})C(\vec{r}, t)d\vec{r} \tag{37}$$

where $\vec{r}_{cm} = (x_{cm}, y_{cm})$, $\mathbf{I}$ denotes a 2×2 identity matrix, and $\mathbf{P}_x = (\partial/\partial x)(\mathbf{H}^T\mathbf{H})$, $\mathbf{P}_y = (\partial/\partial y)(\mathbf{H}^T\mathbf{H})$ where the $\mathbf{H}$ matrix is defined via $\vec{H}(\vec{r}, t) = \mathbf{H}(\vec{r})\vec{u}(t)$ and each of its eight columns contains the magnetic field created by a single magnet turned on with unit strength. Generally, the $\mathbf{Q}_x$ and $\mathbf{Q}_y$ matrices are indefinite while the $\mathbf{W}$ matrix remained positive definite throughout the move-to-center step in Figure 22, but $\mathbf{W}$ can become indefinite if β is not chosen large enough.

Equations (33) and (34) depend on the current ferrofluid concentration $C(\vec{r}, t)$ and are solved by semidefinite quadratic programming at each time to yield a closed-loop control. Each such quadratic programming solution takes 0.15–0.2 s on a desktop computer. Similar to the single droplet case [(8)–(14) and Figures 9–11], it can be guaranteed that a global optimum is attained for (33)–(37) at each moment. However, since these equations phrase an optimization task that is local in time (the magnet control is optimized for each instantaneous ferrofluid distribution without any knowledge of future ferrofluid behavior), there is as yet no guarantee of optimality over a finite time interval. Figure 22(a), second row (phase II), shows the optimized motion of the ferrofluid from edge to center.

Once the ferrofluid has been delivered to the center, it begins to diffuse away. By Earnshaw's theorem (see "Samuel Earnshaw's 1839 Theorem") there is no way to actuate the magnets so that all the magnetic forces would point into the center to create a stable trap and prevent outward diffusion. Instead, the magnets are simply turned off for a wait time T_{III}. The ferrofluid diffusion during this stage is shown by the third row (phase III) in Figure 22(a). This wait time T_{III} is optimally chosen to be short enough so that not all the ferrofluid diffuses away from the center, but long enough so that the duration of the wait step, which creates the on-average high concentration at the center, is long compared to the collect (phase I) and move-to-center (phase II) steps.

After the hot spot at the center has diminished, phase III ends, and the sequence repeats again. Now ferrofluid is collected to a new location at the edge of the domain (fourth and last row in Figure 22(a), phase I again), is again moved with minimal spreading to the center (not shown), and there is another waiting period (also not shown). Choosing a new edge region at each cycle prevents high on-average ferrofluid concentration at any single edge location. Figure 22(b) shows the amount of ferrofluid within the $\|\vec{r}\| \le 0.2$ target at each time. Panel c shows the time-averaged ferrofluid concentration. Compared to Figure 21, there is a bright hot spot at the center with only modest on-average ferrofluid concentration at the domain edges. In a patient, this would correspond to a high concentration at the deep tumor, modest concentration at locations underneath the skin, and low concentrations in the rest of the body. Also in a patient, in addition to diffusion, blood flow in major vessels would act to partially wash away ferrofluid from the center and so the phase III wait step must be augmented by active feedback control that will continuously correct for the disturbing effects of patient blood flow.

Emerging Capabilities for Real-Time In-Vivo Ferrofluid Sensing

MRI can be used to sense magnetic nanoparticles inside patients [87]. Accumulations of magnetic particles disrupt the MR signal and show up as lighter regions that are marked by the two white arrows in Figure 13(a) (these regions are hard to see for the uninitiated but are clear to a radiologist). However, current MR imaging is too slow to sense ferrofluid distributions in real time, as is necessary for closed-loop feedback control. Depending on the size of the region of the body to be imaged and the desired resolution, MR scans take between half an hour to a couple of hours [30], [242]. The speed of MR scanning is limited by the magnetic field gradient rise-time (known as the slew rate and measured in tesla per meter per second). To date, the fastest MRI slew rate has been 400 T/m/s [279]. MRI slew rates have been limited by safety regulations that are

concerned with preventing neural stimulation bioeffects; quickly changing magnetic fields create electric eddy currents [196] that can stimulate nerve cells [280]. However, if the magnetic fields are changed much faster than the cells can respond, in microseconds (for example at 120,000 T/m/s slew rates) by using pulsed-power technology [281], then bioeffects can be bypassed as shown by Fricke and Weinberg [32]. This makes it feasible to construct fast-MRI machines that could safely sense ferrofluids in real time.

As an alternate approach, nuclear imaging [282] has been used in patients for many years and is being improved for faster speed [283]–[286]. X-ray imaging [287], [288] is used to measure the real-time location of surgical tips in the Stereotaxis system [Figure 2(a)] but has not been sensitive enough to measure nanoparticle distributions in animals [289], [290]. PET [291] is a technique that produces three-dimensional images of the distribution of radioactive (tracer) particles inside the body. Through a number of biomechanisms, such as by glucose uptake and subsequent phosphorylation that is elevated in rapidly growing malignant tumors [33], the radioactive tracers are designed to be taken up predominantly by tumors and the gamma rays they emit are then detected and localized by external gamma cameras [292]–[296]. Magnetic nanoparticles have been made radioactive by addition of the same carbon-11 (^{11}C), nitrogen-13 (^{13}N), oxygen-15 (^{15}O), and fluorine-18 (^{18}F) elements approved for and most commonly used during PET scanning in patients [37], [297], [298]. Further, there are efforts underway to improve the sensitivity and speed of gamma cameras [292], [299]–[301], which could enable the real-time sensing of radioactive ferrofluids. Radioactivity could be used only as a ferrofluid sensing modality, or, if the degree of ferrofluid control to tumors is sufficient, the nanoparticles could be made sufficiently radioactive to also treat tumors with radiation in addition to chemotherapy.

Finally, a third emerging option, without the need for radioactivity, is magnetic particle imaging (MPI) [36], [39]–[41], [210]. This sensing exploits the nonlinear magnetic response of magnetic nanoparticles under strong (> 3 T/m) magnetic field gradients [210]. Simply put, this technique first creates a magnetic field node point within the imaging location using two external "sensing" coils [36]. Then additional driving coils apply a time-varying magnetization to which particles near the node point will respond. Finally, two other sensing coils then interpret the particle magnetization curves and determine the particle concentration at this node point. This technique has recently been shown to have sufficient temporal and spatial resolution to resolve particle concentrations in the beating heart of a mouse [210]. MPI is specifically designed for magnetic drug targeting; its goal is to locate and quantify magnetic nanoparticle concentrations in-vivo. However, since MPI exploits the nonlinear response of saturated versus unsaturated particles to locate them, and since such nonlinearities first begin at $\sim$0.15 T [302], [303], high fields are required deep inside the body to use MPI to sense magnetic nanoparticles with sufficient resolution.

CONCLUSIONS

This article describes a range of results, from passive magnet design to optimal feedback control of a distributed ferrofluid. Representing magnetic forces as the gradient of a magnetic energy ($\vec{F} = -\nabla U$ with $U = -\kappa \|\vec{H}\|^2$) allowed design and demonstration, in animal experiments, of a simple open-loop two-magnet system to inject nanoparticles into the inner ear. Then a petri-dish test bed was used to develop and test optimal closed-loop manipulation of a single ferrofluid droplet. The demonstrated algorithms exploited the quadratic dependence of the magnetic forces on control inputs while accounting for magnet time delays and spatial discontinuities in the optimal control. Additional modeling was carried out to understand and quantify nanoparticle transport in-vivo, in and around a single blood vessel. All dimensional parameters were reduced to three essential nondimensional numbers, and ferrofluid behavior was mapped across the entire feasible drug delivery parameter space (Figure 16). The predictions matched all prior published magnetic drug delivery experiments, both in-vitro (bench top) and in-vivo (in animals and humans). The model was then extended to vessel distributions taken from autopsy data, which indicated that magnetic sweep may prove useful in better delivering chemotherapy to thousands of poorly vascularized metastatic tumors that otherwise would not receive sufficient treatment. The magnetic sweep parameters were optimized across one group of samples and then tested on a second independent group. Finally, for the long-term goal of focusing therapeutic nanoparticles to deep-tissue tumors, simulations and control designs were developed to drive a distributed ferrofluid to a deep target under the fundamental energy curvature constraints of Earnshaw's theorem.

As discussed in the introduction, magnetic drug targeting has already been demonstrated in animals and in human patients, but its utility has been limited to shallow targets [11], [25], [86], [121], [304]. The goal of our research is to improve magnetic targeting to allow it to better reach additional clinically relevant disease targets. Compared to control of inanimate engineering systems, control of magnetic nanoparticles inside a living person is messier, less certain, and will vary significantly from patient to patient. Even basic things such as the placement and geometry of the majority of blood vessels are unknown in individual patients, and will most likely remain unmeasurable for the foreseeable future (MR imaging can only visualize large vessels [225], [305], [306]). Moreover, many nanoparticle behaviors, such as particle transport in tissue and through vessel walls or nanoparticle uptake by the immune system,

require significantly more research before they are understood on even a rudimentary level.

The magnetic drug targeting community is composed mainly of nanofabricators, chemists, clinicians, and magnetism experts. This community is active with hundreds of people who are fabricating novel nanocarriers, designing magnet systems, and, most crucially, interacting with clinicians to identify new clinical opportunities for magnetic drug targeting. However, this community contains very few control researchers, and this is a good opportunity for the controls community. The end goal in magnetic targeting is to direct therapeutic particles to disease locations, and this is a controls task.

To improve *control* of magnetic drug targeting requires a better interface between control theory and medicine. Medical knowledge must be translated into mathematical models that can be used for magnet control design. This translation requires the immersion of control theorists in human anatomy courses, medical conferences, and animal experiments. Otherwise the created models will either be too simplistic or will include irrelevant complications. Parameters in the models must be identified, as much as possible, which must be performed by combining tissue and animal experiments with system identification techniques. The effect of important parameters that cannot be identified, now or in the foreseeable future, must then be circumvented by clever control design. Since even a single rectangular magnet next to a tumor can already provide a benefit [Figure 2(b)], the question is how to use control theory to do better. Magnet designs must be optimized to enable deeper and stronger forces with smaller, cheaper, and less powerful magnets. Control algorithms must be designed for these magnets, based both on magnet physics and on incomplete and uncertain models for ferrofluid transport inside the body. These advances must then be extensively tested in animal experiments, before they can proceed to human trials and FDA approval, so as to reach patients.

ACKNOWLEDGMENTS

A large number of students and collaborators have made this research possible. The help of Catherine Beni, Christian Bergemann, Oscar Bruno, Zach Cummins, Kenneth Dormer, Didier Depireux, John Lin, Roger Lee, Andreas Lübbe, Greg Marquart, Silvia Muro, Arkadi Nemirovski, Jaime Rodriguez-Canales, Isaac Rutel, Raymond Sedwick, Michael Tangrea, and Irving Weinberg is greatly appreciated. Funding from NIH is gratefully acknowledged.

AUTHOR INFORMATION

Aleksandar Nacev received a B.S. degree in aerospace engineering from the University of Maryland, College Park, in 2008, where he is also currently working toward his Ph.D. His research interests include ferrofluid control for therapeutic treatments, specifically developing the methodology by utilizing simulated, table-top, cell culture, and live animal experiments.

Arash Komaee received a Ph.D. in electrical engineering from the University of Maryland, College Park, in 2008. After a short postdoc at the University of Texas at Dallas working on optimization of inventory systems, he joined the University of Maryland, College Park, as a research associate. His research interests are in the areas of optimal control, stochastic decision making and control, estimation theory and its applications, and nonlinear filtering. In his current research, he applies these areas to problems in control of magnetic nanoparticles.

Azeem Sarwar received a Ph.D. in mechanical engineering in 2009 and master's degrees in mechanical engineering and mathematics from the University of Illinois at Urbana-Champaign. His research interests are mathematical modeling, simulation, optimization, and control design of systems related to drug targeting. He is currently working as a research associate with the Fischell Department of Bioengineering at the University of Maryland, College Park, where his current research is focused toward maximizing the reach of magnetic drug delivery by optimally designing permanent magnet arrays.

Roland Probst received a diploma in computer engineering from the University of Applied Sciences, Mannheim, Germany, and a Ph.D. in aerospace engineering from the University of Maryland, College Park. He is currently a research associate with the Fischell Department of Bioengineering at the University of Maryland. His main interest is to create and develop smart yet simple methods to control micro- and nanoscale systems by electrokinetic and magnetic actuation. He is currently involved in the development of three-dimensional electrokinetic tweezers for nanoassembly applications.

Skye H. Kim received a B.S. in biomedical engineering from the University of Utah and an M.S. in biotechnology from the Johns Hopkins University. She is currently a biomedical scientist with the Science Applications International Corporation, supporting the programmatic review processes for the Congressionally Directed Medical Research Programs, Department of Defense. Her interests include the identification and support of translationally relevant research proposals with potentially high impact for cancer patient care.

Michael Emmert-Buck received his M.D. and Ph.D. degrees from Wayne State University School of Medicine. His clinical training in anatomic pathology was conducted in the Laboratory of Pathology, NCI, and completed in 1995. In 1996, he was promoted to head of the Pathogenetics Unit. His group develops new technologies that address unmet needs in the field of molecular pathology and then applies these methods to tumor biology projects. The Unit invented or coinvented laser capture microdissection (LCM), layered expression scanning, and molecular-targeted dissection. His group also codiscovered the gene for multiple endocrine

neoplasia Type-1. He also serves as director of the LCM Core Laboratory at NCI and as a commissioned officer in the U.S. Public Health Service, providing medical surge capacity in times of national emergency, under the auspices of the U.S. Surgeon General, Department of Health and Human Services, Washington, D.C.

Benjamin Shapiro (benshap@umd.edu) received a B.S. in aerospace engineering from the Georgia Institute of Technology and a Ph.D. from the California Institute of Technology where he worked on symmetry breaking in jet engines. He joined the University of Maryland Department of Aerospace Engineering in 2000. His interests have shifted to control of miniaturized systems, with a focus on systems for biomedical applications. In 2009, he spent his sabbatical at NIH and NIST, half time within the Advanced Technology Center at the National Cancer Institute, the other half at the Center for Nanoscale Science and Technology at the National Institute of Standards and Technology. He is currently an associate professor in the Fischell Department of Bioengineering and the Institute for Systems Research at the University of Maryland. He is also a Fulbright scholar (Germany 2009). He can be contacted at Fischell Department of Bioengineering, 1226 Kim Building, University of Maryland, College Park, MD 20742.

REFERENCES

[1] R. Reszka, P. Beck, I. Fichtner, M. Hentschel, J. Richter, and J. Kreuter, "Body distribution of free, liposomal and nanoparticle-associated mitoxantrone in B16-melanoma-bearing mice," *J. Pharmacol. Experiment. Therapeut.*, vol. 280, pp. 232–237, Jan. 1997.

[2] M. C. Perry, *The Chemotherapy Source Book.* Philadelphia, PA: Wolters Kluwer Health, 2008.

[3] S. B. Horwitz, "Taxol (paclitaxel): Mechanisms of action," *Ann. Oncol.: Official J. Eur. Soc. Medical Oncol./ESMO*, vol. 5, suppl. 6, pp. S3–S6, 1994.

[4] D. Lorusso, A. Pietragalla, S. Mainenti, V. Masciullo, G. Di Vagno, and G. Scambia, "Review role of topotecan in gynaecological cancers: Current indications and perspectives," *Crit. Rev. Oncol./Hematol.*, vol. 74, pp. 163–174, June 2010.

[5] S. B. Duffull and B. A. Robinson, "Clinical pharmacokinetics and dose optimisation of carboplatin," *Clin. Pharmacokinet.*, vol. 33, pp. 161–183, Sept. 1997.

[6] S. Rockwell and G. B. Grindey, "Effect of 2', 2'-difluorodeoxycytidine on the viability and radiosensitivity of EMT6 cells in vitro," *Oncol. Res.*, vol. 4, no. 4–5, pp. 151–155, 1992.

[7] E. Mini, S. Nobili, B. Caciagli, I. Landini, and T. Mazzei, "Cellular pharmacology of gemcitabine," *Ann. Oncol.: Official J. Eur. Soc. Med. Oncol./ESMO*, vol. 17, suppl. 5, pp. v7–v12, May 2006.

[8] T. De Vita, Jr., S. Hellman, and S. A. Rosenberg, *Cancer, Principles and Practice of Oncology*, 8th ed. Philadelphia, PA: Lippincott Williams and Wilkins, 2008.

[9] B. Chabner and D. Longo, *Cancer Chemotherapy and Biotherapy: Principles and Practice*, 5th ed. Philadelphia, PA: Wolters Kluwer Health, 2011.

[10] N. M. Orekhova, R. S. Akchurin, A. A. Belyaev, M. D. Smirnov, S. E. Ragimov, and A. N. Orekhov, "Local prevention of thrombosis in animal arteries by means of magnetic targeting of aspirin-loaded red cells," *Thromb. Res.*, vol. 57, no. 4, p. 611–616, 1990.

[11] A. S. Lubbe, C. Bergemann, H. Riess, F. Schriever, P. Reichardt, K. Possinger, M. Matthias, B. Dorken, F. Herrmann, R. Gurtler, P. Hohenberger, N. Haas, R. Sohr, B. Sander, A. J. Lemke, D. Ohlendorf, W. Huhnt, and D. Huhn, "Clinical experiences with magnetic drug targeting: A phase I study with 4'-epidoxorubicin in 14 patients with advanced solid tumors," *Cancer Res.*, vol. 56, no. 20, pp. 4686–4693, 1996.

[12] V. P. Torchilin, "Drug targeting," *Eur. J. Pharmaceut. Sci.*, vol. 11, no. 4, pp. 81–91, 2000.

[13] A. S. Lubbe, C. Alexiou, and C. Bergemann, "Clinical applications of magnetic drug targeting," *J. Surg. Res.*, vol. 95, no. 2, pp. 200–206, 2001.

[14] M. Shinkai, "Functional magnetic particles for medical application," *J. Biosci. Bioeng.*, vol. 94, no. 6, pp. 606–613, 2002.

[15] C. Alexiou, R. Jurgons, R. J. Schmid, C. Bergemann, J. Henke, W. Erhardt, E. Huenges, and F. Parak, "Magnetic drug targeting—Biodistribution of the magnetic carrier and the chemotherapeutic agent mitoxantrone after locoregional cancer treatment," *J. Drug Target.*, vol. 11, no. 3, pp. 139–149, 2003.

[16] D. L. Holligan, G. T. Gillies, and J. P. Dailey, "Magnetic guidance of ferrofluidic nanoparticles in an in vitro model of intraocular retinal repair," *Nanotechnology*, vol. 14, no. 6, pp. 661–666, 2003.

[17] Q. A. Pankhurst, J. Connolly, S. K. Jones, and J. Dobson, "Applications of magnetic nanoparticles in biomedicine," *J. Phys. D: Appl. Phys.*, vol. 36, no. 13, pp. R167–R181, 2003.

[18] R. Jurgons, C. Seliger, A. Hilpert, L. Trahms, S. Odenbach, and C. Alexiou, "Drug loaded magnetic nanoparticles for cancer therapy," *J. Phys.-Condens. Matter*, vol. 18, no. 38, pp. S2893–S2902, 2006.

[19] C. Alexiou, R. Jurgons, C. Seliger, B. Schick, S. Kolb, and H. Iro, "Magnetic drug targeting in cancers of the head and neck," *Laryngo-Rhino-Otologie*, vol. 85, no. 11, pp. 857–859, 2006.

[20] J. Dobson, "Magnetic micro- and nano-particle-based targeting for drug and gene delivery," *Nanomedicine*, vol. 1, no. 1, pp. 31–37, 2006.

[21] M. Arruebo, R. Fernandez-Pacheco, M. R. Ibarra, and J. Santamaria, "Magnetic nanoparticles for drug delivery," *Nano Today*, vol. 2, no. 3, pp. 22–32, 2007.

[22] M. Johannsen, U. Gneveckow, B. Thiesen, K. Taymoorian, C. H. Cho, N. Waldofner, R. Scholz, A. Jordan, S. A. Loening, and P. Wust, "Thermotherapy of prostate cancer using magnetic nanoparticles: Feasibility, imaging, and three-dimensional temperature distribution," *Eur. Urol.*, vol. 52, pp. 1653–1661, Dec. 2007.

[23] C. Sun, J. Lee, and M. Zhang, "Magnetic nanoparticles in MR imaging and drug delivery," *Adv. Drug Deliv. Rev.*, vol. 60, pp. 1252–1265, Aug. 2008.

[24] Q. A. Pankhurst, N. K. Thanh, S. K. Jones, and J. Dobson, "Progress in applications of magnetic nanoparticles in biomedicine," *J. Phys. D: Appl. Phys.*, vol. 42, no. 22, pp. 224,001–224,016, 2009.

[25] N. Tran and T. J. Webster, "Magnetic nanoparticles: Biomedical applications and challenges," *J. Mater. Chem.*, vol. 20, no. 40, pp. 8760–8767, 2010.

[26] J. Dobson, "Magnetic nanoparticles for drug delivery," *Drug Develop. Res.*, vol. 67, no. 1, pp. 55–60, 2006.

[27] K. Maier-Hauff, R. Rothe, R. Scholz, U. Gneveckow, P. Wust, B. Thiesen, A. Feussner, A. von Deimling, N. Waldoefner, R. Felix, and A. Jordan, "Intracranial thermotherapy using magnetic nanoparticles combined with external beam radiotherapy: Results of a feasibility study on patients with glioblastoma multiforme," *J. Neuro-Oncol.*, vol. 81, pp. 53–60, Jan. 2007.

[28] P. K. Stoimenov, R. L. Klinger, G. L. Marchin, and K. J. Klabunde, "Metal oxide nanoparticles as bactericidal agents," *Langmuir*, vol. 18, pp. 6679–6686, Aug. 2002.

[29] P. Gong, H. Li, X. He, K. Wang, J. Hu, W. Tan, S. Zhang, and X. Yang, "Preparation and antibacterial activity of Fe_3O_4@Ag nanoparticles," *Nanotechnology*, vol. 18, pp. 285604–285611, July 2007.

[30] E. D. Allen and J. H. Burdette, *Questions and Answers in MRI.* 2nd ed., St. Louis, MO: Mosby, 2001.

[31] A. J. Lemke, M. I. S. von Pilsach, A. Lubbe, C. Bergemann, H. Riess, and R. Felix, "MRI after magnetic drug targeting in patients with advanced solid malignant tumors," *Eur. Radiol.*, vol. 14, no. 11, pp. 1949–1955, 2004.

[32] S. Fricke, I. N. Weinberg, P. Stepanov, S. Glidden, A. McMillan, and P. M. Starewicz, "Threshold for peripheral nerve stimulation with ultra-fast gradients," in *Proc. 19th Meeting Society for Magnetic Resonance in Medicine*, Montreal, Canada, 2011, p. 1787.

[33] N. K. Devaraj, E. J. Keliher, G. M. Thurber, M. Nahrendorf, and R. Weissleder, "18F labeled nanoparticles for in vivo PET-CT imaging," *Bioconjug. Chem.*, vol. 20, no. 2, pp. 397–401, 2009.

[34] S. I. Parker, C. J. Kenney, D. Gnani, A. C. Thompson, E. Mandelli, G. Meddeler, J. Hasi, J. Morse, and E. M. Westbrook, "3DX: An X-ray pixel array detector with active edges," *IEEE Trans. Nuclear Sci.*, vol. 53, no. 3, pp. 1676–1688, 2006.

[35] C. J. Kenney, J. D. Segal, E. M. Westbrook, S. Paker, J. Hasi, C. DaVia, S. Watts, and J. Morse, "Active-edge planar radiation sensors," *Nuclear Instrum. Methods Phys. Res. A*, vol. 565, no. 1, pp. 272–277, 2006.

[36] B. Gleich and J. Weizenecker, "Tomographic imaging using the nonlinear response of magnetic particles," *Nature*, vol. 435, pp. 1214–1217, June 2005.
[37] M. Mahmoudi, V. Serpooshan, and S. Laurent, "Engineered nanoparticles for biomolecular imaging," *Nanoscale*, vol. 3, no. 8, pp. 3007–3026, 2011.
[38] Y. Ishihara, T. Kuwabara, and N. Wadamori, "Sensitivity improvement of a molecular imaging technique based on magnetic nanoparticles," in *Medical Imaging 2011: Biomedical Applications in Molecular, Structural, and Functional Imaging* (SPIE, vol. 7965), J. B. Weaver and R. C. Molthen, Eds. 2011 p. 79652J.
[39] T. Knopp, S. Biederer, T. F. Sattel, J. Rahmer, J. Weizenecker, B. Gleich, J. Borgert, and T. M. Buzug, "2D model-based reconstruction for magnetic particle imaging," *Med. Phys.*, vol. 37, no. 2, pp. 485–492, 2010.
[40] T. Knopp, T. F. Sattel, S. Biederer, J. Rahmer, J. Weizenecker, B. Gleich, J. Borgert, and T. M. Buzug, "Model-based reconstruction for magnetic particle imaging," *IEEE Trans. Med. Imag.*, vol. 29, no. 1, pp. 12–18, 2010.
[41] S. Biederer, T. Knopp, T. F. Sattel, K. Ludtke-Buzug, B. Gleich, J. Weizenecker, J. Borgert, and T. M. Buzug, "Magnetization response spectroscopy of superparamagnetic nanoparticles for magnetic particle imaging," *J. Phys. D: Appl. Phys.*, vol. 42, pp. 42–49, 2009.
[42] T. J. Dougherty, C. J. Gomer, G. Jori, D. Kessel, M. Korbelik, J. Moan, and Q. Peng, "Photodynamic therapy," *J. Nat. Cancer Inst*, vol. 90, no. 12, pp. 889–905, 1998.
[43] B. W. Barry, "Novel mechanisms and devices to enable successful transdermal drug delivery," *Eur. J. Pharmaceut. Sci.*, vol. 14, no. 2, pp. 101–114, 2001.
[44] A. R. Denet, R. Vanbever, and V. Preat, "Skin electroporation for transdermal and topical delivery," *Adv. Drug Deliv. Rev.*, vol. 56, no. 5, pp. 659–674, 2004.
[45] W. G. Pitt, G. A. Husseini, and B. J. Staples, "Ultrasonic drug delivery—A general review," *Expert Opin. Drug Deliv.*, vol. 1, no. 1, pp. 37–56, 2004.
[46] Z. G. Gao, H. D. Fain, and N. Rapoport, "Controlled and targeted tumor chemotherapy by micellar-encapsulated drug and ultrasound," *J. Control. Release*, vol. 102, no. 1, pp. 203–222, 2005.
[47] J. F. Schenck, "Safety of strong, static magnetic fields," *J. Magn. Reson. Imag.*, vol. 12, pp. 2–19, July 2000.
[48] D. J. Schaefer, J. D. Bourland, and J. A. Nyenhuis, "Review of patient safety in time-varying gradient fields," *J. Magn. Reson. Imag.*, vol. 12, pp. 20–29, July 2000.
[49] E. Andersen, "Magnetic resonance imaging–Safety and health issues," *AAOHN J.*, vol. 55, pp. 137–139, Apr. 2007.
[50] S. Martel, O. Felfoul, J. B. Mathieu, A. Chanu, S. Tamaz, M. Mohammadi, M. Mankiewicz, and N. Tabatabaei, "MRI-based medical nanorobotic platform for the control of magnetic nanoparticles and flagellated bacteria for target interventions in human capillaries," *Int. J. Robot. Res.*, vol. 28, no. 9, pp. 1169–1182, 2009.
[51] C. Catana, Y. Wu, M. S. Judenhofer, J. Qi, B. J. Pichler, and S. R. Cherry, "Simultaneous acquisition of multislice PET and MR images: Initial results with a MR-compatible PET scanner," *J. Nuclear Med.*, vol. 47, no. 12, pp. 1968–76, 2006.
[52] W. T. Katsiyiannis, D. P. Melby, J. L. Matelski, V. L. Ervin, K. L. Laverence, and C. C. Gornick, "Feasibility and safety of remote-controlled magnetic navigation for ablation of atrial fibrillation," *Amer. J. Cardiol.*, vol. 102, no. 12, pp. 1674–1676, 2008.
[53] A. Haake and J. Dual, "Contactless micromanipulation of small particles by an ultrasound field excited by a vibrating body," *J. Acoust. Soc. Amer.*, vol. 117, pp. 2752–2760, May 2005.
[54] S. Oberti, D. Moller, A. Neild, J. Dual, F. Beyeler, B. Nelson, and S. Gutmann, "Strategies for single particle manipulation using acoustic and flow fields," *Ultrasonics*, vol. 50, pp. 247–257, Feb. 2010.
[55] C. Polk and E. Postow, *Handbook of Biological Effects of Electromagnetic Fields*. Boca Raton, FL: CRC Press, 1996.
[56] J. Villemejane and L. M. Mir, "Review. Physical methods of nucleic acid transfer: General concepts and applications," *Brit. J. Pharmacol.*, vol. 157, no. 2, pp. 207–219, 2009.
[57] R. G. Hawley, F. H. Lieu, A. Z. Fong, and T. S. Hawley, "Versatile retroviral vectors for potential use in gene therapy," *Gene Ther.*, vol. 1, no. 2, pp. 136–138, 1994.
[58] S. Li and L. Huang, "Nonviral gene therapy: Promises and challenges," *Gene Ther.*, vol. 7, no. 1, pp. 31–34, 2000.
[59] S. W. Kamau, "Enhancement of the efficiency of non-viral gene delivery by application of pulsed magnetic field," *Nucleic Acids Res.*, vol. 34, pp. e40–e40, Mar. 2006.
[60] S. C. McBain, U. Griesenbach, S. Xenariou, A. Keramane, C. D. Batich, E. W. F. W. Alton, and J. Dobson, "Magnetic nanoparticles as gene delivery agents: enhanced transfection in the presence of oscillating magnet arrays," *Nanotechnology*, vol. 19, pp. 405102–405107, Oct. 2008.
[61] E. Stride, C. Porter, A. G. Prieto, and Q. Pankhurst, "Enhancement of microbubble mediated gene delivery by simultaneous exposure to ultrasonic and magnetic fields," *Ultrasound Med. Biol.*, vol. 35, pp. 861–868, May 2009.
[62] C. C. Berry, "Progress in functionalization of magnetic nanoparticles for applications in biomedicine," *J Phys D: Appl. Phys.*, vol. 42, no. 22, pp. 224003–224012, 2009.
[63] A. G. Roca, R. Costo, A. F. Rebolledo, S. Veintemillas-Verdaguer, P. Tartaj, T. Gonzalez-Carreno, M. P. Morales, and C. J. Serna, "Progress in the preparation of magnetic nanoparticles for applications in biomedicine," *J. Phys. D: Appl. Phys.*, vol. 42, pp. 224002–224012, Nov. 2009.
[64] O. Veiseh, J. W. Gunn, and M. Zhang, "Design and fabrication of magnetic nanoparticles for targeted drug delivery and imaging," *Adv. Drug Deliv. Rev.*, vol. 62, pp. 284–304, Mar. 2010.
[65] D. C. Drummond, O. Meyer, K. Hong, D. B. Kirpotin, and D. Papahadjopoulos, "Optimizing liposomes for delivery of chemotherapeutic agents to solid tumors," *Pharmacol. Rev.*, vol. 51, pp. 691–743, Dec. 1999.
[66] K. Cho, X. Wang, S. Nie, Z. Chen, and D. M. Shin, "Therapeutic nanoparticles for drug delivery in cancer," *Clin. Cancer Res.*, vol. 14, pp. 1310–1316, Mar. 2008.
[67] U. Zimmermann and G. Pilwat, "Organ specific application of drugs by means of cellular capsule systems," *Zeitschrift Naturforschung C Biosciences*, vol. 31, no. 11–12, pp. 732–736, 1976.
[68] A. Solanki, J. D. Kim, and K. Lee, "Nanotechnology for regenerative medicine: Nanomaterials for stem cell imaging," *Nanomedicine*, vol. 3, pp. 567–578, Aug. 2008.
[69] R. Weissleder, A. Bogdanov, E. A. Neuwelt, and M. Papisov, "Long-circulating iron oxides for MR imaging," *Adv. Drug Deliv. Rev.*, vol. 16, pp. 321–334, Sept. 1995.
[70] S. Yu and G. M. Chow, "Preparation of polymer-coated functionalized ferrimagnetic iron oxide nanoparticles," Massachusetts Institute of Technology, Cambridge, MA, 2004.
[71] A. J. Cole, A. E. David, J. Wang, C. J. Galban, H. L. Hill, and V. C. Yang, "Polyethylene glycol modified, cross-linked starch-coated iron oxide nanoparticles for enhanced magnetic tumor targeting," *Biomaterials*, vol. 32, no. 8, pp. 2183–2193, 2010.
[72] A. Figuerola, R. Di Corato, L. Manna, and T. Pellegrino, "From iron oxide nanoparticles towards advanced iron-based inorganic materials designed for biomedical applications," *Pharmacol. Res.*, vol. 62, no. 2, pp. 126–143, 2010.
[73] M. W. Wilson, R. K. Kerlan, N. A. Fidelman, A. P. Venook, J. M. LaBerge, J. Koda, and R. L. Gordon, "Hepatocellular carcinoma: Regional therapy with a magnetic targeted carrier bound to doxorubicin in a dual MR imaging/conventional angiography suite-initial experience with four patients," *Radiology*, vol. 230, no. 1, pp. 287–293, 2004.
[74] M. Johannsen, U. Gneveckow, L. Eckelt, A. Feussner, N. Waldofner, R. Scholz, S. Deger, P. Wust, S. A. Loening, and A. Jordan, "Clinical hyperthermia of prostate cancer using magnetic nanoparticles: Presentation of a new interstitial technique," *Int. J. Hypertherm.*, vol. 21, pp. 637–647, Nov. 2005.
[75] T. Sato and R. Ruch, *Stabilization of Colloidal Dispersions by Polymer Adsorption*, vol. 9. New York: Dekker, 1980.
[76] J. Park, G. von Maltzahn, L. Zhang, M. P. Schwartz, E. Ruoslahti, S. N. Bhatia, and M. J. Sailor, "Magnetic iron oxide nanoworms for tumor targeting and imaging," *Adv. Mater.*, vol. 20, pp. 1630–1635, May 2008.
[77] V. P. Torchilin, "Recent advances with liposomes as pharmaceutical carriers," *Nat. Rev. Drug Discov.*, vol. 4, pp. 145–160, Feb. 2005.
[78] N. Nasongkla, E. Bey, J. Ren, H. Ai, C. Khemtong, J. S. Guthi, S. F. Chin, A. D. Sherry, D. A. Boothman, and J. Gao, "Multifunctional polymeric micelles as cancer-targeted, MRI-ultrasensitive drug delivery systems," *Nano Lett.*, vol. 6, no. 11, pp. 2427–2430, 2006.
[79] S. Lecommandoux, O. Sandre, F. Checot, and R. Perzynski, "Smart hybrid magnetic self-assembled micelles and hollow capsules," *Progr. Solid-State Chem.*, vol. 34, pp. 171–179, July 2006.
[80] P. G. Kyrtatos, P. Lehtolainen, M. Junemann-Ramirez, A. Garcia-Prieto, A. N. Price, J. F. Martin, D. G. Gadian, Q. A. Pankhurst, and M. F. Lythgoe,

"Magnetic tagging increases delivery of circulating progenitors in vascular injury," *JACC Interv.*, vol. 2, no. 8, pp. 794–802, 2009.
[81] Z. Y. Huang, N. Pei, Y. Y. Wang, X. X. Xie, A. J. Sun, L. Shen, S. N. Zhang, X. B. Liu, Y. Z. Zou, J. Y. Qian, and J. B. Ge, "Deep magnetic capture of magnetically loaded cells for spatially targeted therapeutics," *Biomaterials*, vol. 31, no. 8, pp. 2130–2140, 2010.
[82] B. Bonnemain, "Superparamagnetic agents in magnetic resonance imaging: physicochemical characteristics and clinical applications. A review," *J. Drug Target.*, vol. 6, no. 3, pp. 167–174, 1998.
[83] M. G. Harisinghani, J. Barentsz, P. F. Hahn, W. M. Deserno, S. Tabatabaei, C. H. van de Kaa, J. de la Rosette, and R. Weissleder, "Noninvasive detection of clinically occult lymph-node metastases in prostate cancer," *New Engl. J. Med.*, vol. 348, pp. 2491–2499, June 2003.
[84] A. Singh, T. Patel, J. Hertel, M. Bernardo, A. Kausz, and L. Brenner, "Safety of ferumoxytol in patients with anemia and CKD," *Amer. J. Kidney Diseases: Official J. Nat. Kidney Foundat.*, vol. 52, pp. 907–915, Nov. 2008.
[85] Y. X. Wang, S. M. Hussain, and G. P. Krestin, "Superparamagnetic iron oxide contrast agents: Physicochemical characteristics and applications in MR imaging," *Eur. Radiol.*, vol. 11, no. 11, pp. 2319–2331, 2001.
[86] A. S. Lubbe, C. Bergemann, W. Huhnt, T. Fricke, H. Riess, J. W. Brock, and D. Huhn, "Preclinical experiences with magnetic drug targeting: Tolerance and efficacy," *Cancer Res.*, vol. 56, no. 20, pp. 4694–4701, 1996.
[87] A. Lemke, B. Sander, A. Luebbe, H. Riess, N. Hosten, and R. Felix, "MR imaging after magnetic drug targeting in patients with soft-tissue tumors," *Radiology*, vol. 201, pp. 1421–1421, 1996.
[88] A. Nacev, C. Beni, O. Bruno, and B. Shapiro, "The behaviors of ferromagnetic nano-particles in and around blood vessels under applied magnetic fields," *J. Magn. Magn. Mater.*, vol. 323, no. 6, pp. 651–668, 2011.
[89] A. D. Grief and G. Richardson, "Mathematical modeling of magnetically targeted drug delivery," *J. Magn. Magn. Mater.*, vol. 293, no. 1, pp. 455–463, 2005.
[90] A. Nacev, C. Beni, O. Bruno, and B. Shapiro, "Magnetic nanoparticle transport within flowing blood and into surrounding tissue," *Nanomedicine*, vol. 5, no. 9, pp. 1459–1466, 2010.
[91] A. Nacev, S. H. Kim, J. Rodiguez-Canales, M. A. Tangrea, B. Shapiro, and M. R. Emmert-Buck, "A dynamic magnetic shift method to increase nanoparticle concentration in cancer metastases: A feasibility study using simulations on autopsy specimens," *Int. J. Nanomed.*, vol. 6, no. 1, pp. 2907–2923, 2011.
[92] A. E. David, A. J. Cole, B. Chertok, Y. S. Park, and V. C. Yang, "A combined theoretical and in vitro modeling approach for predicting the magnetic capture and retention of magnetic nanoparticles in vivo," *J. Control. Release*, vol. 152, no. 1, pp. 67–75, 2011.
[93] S. K. Hobbs, W. L. Monsky, F. Yuan, W. G. Roberts, L. Griffith, V. P. Torchilin, and R. K. Jain, "Regulation of transport pathways in tumor vessels: Role of tumor type and microenvironment," *Proc. Nat. Acad. Sci.*, vol. 95, no. 8, pp. 4607–4612, 1998.
[94] D. B. Montgomery, *Solenoid Magnet Design*. New York: Wiley, 1969.
[95] H. Xu, S. M. Conolly, G. C. Scott, and A. Macovski, "Homogeneous magnet design using linear programming," *IEEE Trans. Magn.*, vol. 36, no. 2, pp. 476–483, 2000.
[96] K. Preis, O. Biro, M. Friedrich, A. Gottvald, and C. Magele, "Comparison of different optimization strategies in the design of electromagnetic devices," *IEEE Trans. Magn.*, vol. 27, no. 5, pp. 4154–4157, 1991.
[97] S. Martel, C. C. Tremblay, S. Ngakeng, and G. Langlois, "Controlled manipulation and actuation of micro-objects with magnetotactic bacteria," *Appl. Phys. Lett.*, vol. 89, no. 23, pp. 233904–233904-3, 2006.
[98] S. Martel, J. Mathieu, O. Felfoul, A. Chanu, E. Aboussouan, S. Tamaz, P. Pouponneau, L. Yahia, G. Beaudoin, G. Soulez, and M. Mankiewicz, "Medical and technical protocol for automatic navigation of a wireless device in the carotid artery of a living swine using a standard clinical MRI system," *Med. Image Comput. Comput.-Assist. Interv.*, 2007, pp. 144–152.
[99] S. Martel, M. Mohammadi, O. Felfoul, Z. Lu, and P. Pouponneau, "Flagellated magnetotactic bacteria as controlled MRI-trackable propulsion and steering systems for medical nanorobots operating in the human microvasculature," *Int. J. Robot. Res.*, vol. 28, no. 4, pp. 571–582, 2009.
[100] A. Komaee and B. Shapiro, "Steering a ferromagnetic particle by optimal magnetic feedback control," *IEEE Trans. Contr. Syst. Technol.*, June 2011, pp. 6543–6548.
[101] B. Shapiro, R. Probst, H. E. Potts, D. A. Diver, and A. Lubbe, "Control to concentrate drug-coated magnetic particles to deep-tissue tumors for targeted cancer chemotherapy," in *Proc. 46th IEEE Conf. Decision and Control*, New Orleans, LA, 2007, pp. 3901–3906.
[102] B. Shapiro, "Towards dynamic control of magnetic fields to focus magnetic carriers to targets deep inside the body," *J. Magn. Magn. Mater.*, vol. 321, no. 10, pp. 1594–1599, 2009.
[103] U. O. Hafeli, M. A. Lobedann, J. Steingroewer, L. R. Moore, and J. Riffle, "Optical method for measurement of magnetophoretic mobility of individual magnetic microspheres in defined magnetic field," *J. Magn. Magn. Mater.*, vol. 293, no. 1, pp. 224–239, 2005.
[104] E. B. Denkba, E. Kilicay, C. Birlikseven, and E. Ozturk, "Magnetic chitosan microspheres: Preparation and characterization," *React. Funct. Polymers*, vol. 50, no. 3, pp. 225–232, 2002.
[105] K. J. Widder, R. M. Morris, G. Poore, D. P. Howard, and A. E. Senyei, "Tumor remission in Yoshida sarcoma-bearing rats by selective targeting of magnetic albumin microspheres containing doxorubicin," *Proc. Nat. Acad. Sci.*, vol. 78, no. 1, pp. 579–581, 1981.
[106] A. Senyei, K. Widder, and G. Czerlinski, "Magnetic guidance of drug carrying microspheres," *J. Appl. Phys.*, vol. 49, no. 6, pp. 3578–3583, 1978.
[107] H. Xu, T. Song, X. Bao, and L. Hu, "Site-directed research of magnetic nanoparticles in magnetic drug targeting," *J. Magn. Magn. Mater.*, vol. 293, no. 1, pp. 514–519, 2005.
[108] R. E. Rosensweig, *Ferrohydrodynamics*. Mineola, NY: Dover, 1985.
[109] Y. Okuhata, "Delivery of diagnostic agents for magnetic resonance imaging," *Adv. Drug Deliv. Rev.*, vol. 37, no. 1–3, pp. 121–137, 1999.
[110] R. L. Fournier, *Basic Transport Phenomena in Biomedical Engineering*. New York: Taylor & Francis, 2007.
[111] W. M. Saltzman, *Drug Delivery: Engineering Principles for Drug Therapy*. New York: Oxford Univ. Press, 2001.
[112] F. Yuan, M. Dellian, D. Fukumura, M. Leunig, D. A. Berk, V. P. Torchilin, and R. K. Jain, "Vascular permeability in a human tumor xenograft: Molecular size dependence and cutoff size," *Cancer Res.*, vol. 55, no. 17, pp. 3752–3756, 1995.
[113] C. Zhang, M. Jugold, E. C. Woenne, T. Lammers, B. Morgenstern, M. M. Mueller, H. Zentgraf, M. Bock, M. Eisenhut, and W. Semmler, "Specific targeting of tumor angiogenesis by RGD-conjugated ultrasmall superparamagnetic iron oxide particles using a clinical 1.5-T magnetic resonance scanner," *Cancer Res.*, vol. 67, no. 4, pp. 1555–1562, 2007.
[114] A. Natarajan, C. Gruettner, R. Ivkov, G. L. DeNardo, G. Mirick, A. Yuan, A. Foreman, and S. J. DeNardo, "NanoFerrite particle based radioimmunonanoparticles: Binding affinity and in vivo pharmacokinetics," *Bioconjug. Chem*, vol. 19, no. 6, pp. 1211–1218, 2008.
[115] L. Josephson, M. F. Kircher, U. Mahmood, Y. Tang, and R. Weissleder, "Near-infrared fluorescent nanoparticles as combined MR/optical imaging probes," *Bioconjug. Chem.*, vol. 13, no. 3, pp. 554–560, 2002.
[116] C. Alexiou, D. Diehl, P. Henninger, H. Iro, R. Rockelein, W. Schmidt, and H. Weber, "A high field gradient magnet for magnetic drug targeting," *IEEE Trans. Appl. Superconduct.*, vol. 16, no. 2, pp. 1527–1530, 2006.
[117] J. Ally, B. Martin, M. B. Khamesee, W. Roa, and A. Amirfazli, "Magnetic targeting of aerosol particles for cancer therapy," *J. Magn. Magn. Mater.*, vol. 293, no. 1, pp. 442–449, 2005.
[118] P. Dames, B. Gleich, A. Flemmer, K. Hajek, N. Seidl, F. Wiekhorst, D. Eberbeck, I. Bittmann, C. Bergemann, T. Weyh, L. Trahms, J. Rosenecker, and C. Rudolph, "Targeted delivery of magnetic aerosol droplets to the lung," *Nat. Nano*, vol. 2, no. 8, pp. 495–499, 2007.
[119] K. Magnetics. (2011). K&J magnetics—Neodymium magnet specifications. [Online]. Available: http://www.kjmagnetics.com/specs.asp
[120] M. Sagawa, S. Fujimura, N. Togawa, H. Yamamoto, and Y. Matsuura, "New material for permanent magnets on a base of Nd and Fe," *J. Appl. Phys.*, vol. 55, no. 6, pp. 2083–2087, 1984.
[121] S. Goodwin, C. Peterson, C. Hoh, and C. Bittner, "Targeting and retention of magnetic targeted carriers (MTCs) enhancing intra-arterial chemotherapy," *J. Magn. Magn. Mater.*, vol. 194, no. 1–3, pp. 132–139, 1999.
[122] M. Lohakan, P. Junchaichanakun, S. Boonsang, and C. Pintavirooj, "A computational model of magnetic drug targeting in blood vessel using finite element method," in *Proc. 2nd IEEE Conf. Industrial Electronics and Applications*, 2007, pp. 231–234.
[123] Y. Yang, J. Jiang, B. Du, Z. Gan, M. Qian, and P. Zhang, "Preparation and properties of a novel drug delivery system with both magnetic and biomolecular targeting," *J. Mater. Sci.: Mater. Med.*, vol. 20, no. 1, pp. 301–307, 2009.
[124] I. Slabu, A. Roth, T. Schmitz-Rode, and M. Baumann, "Optimization of magnetic drug targeting by mathematical modeling and simulation of

magnetic fields," in *Proc. 4th European Conf. Int. Federation for Medical and Biological Engineering*, 2009, pp. 2309–2312.
[125] A. Sarwar, A. Nemirovski, and B. Shapiro, "Optimal halbach permanent magnet designs for maximally pulling and pushing nanoparticles," *J. Magn. Magn. Mater*, vol. 324, no. 5, pp. 742–754.
[126] D. C. Meeker, E. H. Maslen, R. C. Ritter, and F. M. Creighton, "Optimal realization of arbitrary forces in a magnetic stereotaxis system," *IEEE Trans. Magn.*, vol. 32, no. 2, pp. 320–328, 1996.
[127] M. S. Grady, M. A. Howard, III, R. G. Dacey, Jr, W. Blume, M. Lawson, P. Werp, and R. C. Ritter, "Experimental study of the magnetic stereotaxis system for catheter manipulation within the brain," *J. Neurosurg.*, vol. 93, no. 2, pp. 282–288, 2000.
[128] F. M. Creighton, "Control of magnetomotive actuators for an implanted object in brain and phantom materials," Ph.D. dissertation, Univ. Virginia, 1991.
[129] M. S. Grady, M. A. Howard, III, J. A. Molloy, R. C. Ritter, E. G. Quate, and G. T. Gillies, "Nonlinear magnetic stereotaxis: Three-dimensional, in vivo remote magnetic manipulation of a small object in canine brain," *Med. Phys.*, vol. 17, no. 3, pp. 405–415, 1990.
[130] M. A. Howard, III, R. C. Ritter, and M. S. Grady, "Video tumor fighting system," U.S. Patent 4869247, 1989.
[131] R. C. Ritter, "Open field system for magnetic surgery," U.S. Patent 6241671, 2001.
[132] P. R. Werp, "Methods and apparatus for magnetically controlling motion direction of a mechanically pushed catheter," U.S. Patent 6015414, 2002.
[133] F. J. Bova and W. A. Friedman, "Computer controlled guidance of a biopsy needle," U.S. Patent 6546279, 2003.
[134] Y. M. Eyssa, "Apparatus and methods for controlling movement of an object through a medium using a magnetic field," U.S. Patent 6842324, 2005.
[135] T. Bauernfeind, F. Akca, B. Schwagten, N. de Groot, Y. Van Belle, S. Valk, B. Ujvari, L. Jordaens, and T. Szili-Torok, "The magnetic navigation system allows safety and high efficacy for ablation of arrhythmias," *Europace*, vol. 13, no. 7, pp. 1015–1021, 2011.
[136] G. Ciuti, P. Valdastri, A. Menciassi, and P. Dario, "Robotic magnetic steering and locomotion of capsule endoscope for diagnostic and surgical endoluminal procedures," *Robotica*, vol. 28, no. 2, pp. 199–207, 2010.
[137] S. Tamaz, R. Gourdeau, A. Chanu, J. Mathieu, and S. Martel, "Real-time MRI-based control of a ferromagnetic core for endovascular navigation," *IEEE Trans. Biomed. Eng.*, vol. 55, no. 7, pp. 1854–1863, 2008.
[138] S. Yim and M. Sitti, "Design and analysis of a magnetically actuated and compliant capsule endoscopic robot," in *Proc. 2011 IEEE Int. Conf. Robotics and Automation*, pp. 4810–4815.
[139] X. Wang and M. Q. Meng, "A fast algorithm for field computation in magnetic guidance," in *Proc. Int. Conf. Information and Automation*, 2008, pp. 1608–1613.
[140] O. Ergeneman, G. Dogangil, M. P. Kummer, J. J. Abbott, M. K. Nazeeruddin, and B. J. Nelson, "A magnetically controlled wireless optical oxygen sensor for intraocular measurements," *IEEE Sensors J.*, vol. 8, no. 1, pp. 29–37, 2008.
[141] S. Jeon, G. Jang, H. Choi, and S. Park, "Magnetic navigation system with gradient and uniform saddle coils for the wireless manipulation of micro-robots in human blood vessels," *IEEE Trans. Magn.*, vol. 46, no. 6, pp. 1943–1946, 2010.
[142] S. Martel, J. B. Mathieu, O. Felfoul, A. Chanu, E. Aboussouan, S. Tamaz, P. Pouponneau, L. H. Yahia, G. Beaudoin, and G. Soulez, "A computer-assisted protocol for endovascular target interventions using a clinical MRI system for controlling untethered microdevices and future nanorobots," *Comput. Aided Surg.*, vol. 13, no. 6, pp. 340–352, 2008.
[143] P. Vartholomeos, C. Mavroidis, and N. Hata, "Magnetic targeting of aggregated nanoparticles for advanced lung therapies: A robotics approach," in *Proc. 2010 3rd IEEE RAS and EMBS Int. Conf. Biomedical Robotics and Biomechatronics*, pp. 861–868.
[144] K. B. Yesin, K. Vollmers, and B. J. Nelson, "Analysis and design of wireless magnetically guided microrobots in body fluids," in *Proc. IEEE Int. Conf. Robotics and Automation*, 2004, vol. 2, pp. 1333–1338.
[145] K. B. Yesin, K. Vollmers, and B. J. Nelson, "Modeling and control of untethered biomicrorobots in a fluidic environment using electromagnetic fields," *Int. J. Robot. Res.*, vol. 25, no. 5–6, pp. 527–536, 2006.
[146] J. B. Mathieu and S. Martel, "In vivo validation of a propulsion method for untethered medical microrobots using a clinical magnetic resonance imaging system," in *Proc. IEEE/RSJ Int. Conf. Intelligent Robots and Systems*, San Diego, CA, 2007, pp. 502–508.
[147] I. Fleming, M. Balicki, J. Koo, I. Iordachita, B. Mitchell, J. Handa, G. Hager, and R. Taylor, "Cooperative robot assistant for retinal microsurgery," *Med. Image Comput. Comput.-Assist. Interv., MICCAI 2008*, Berlin/Heidelberg: Springer, vol. 5242, pp. 543–550, 2008.
[148] J. Mathieu, G. Beaudoin, and S. Martel, "Method of propulsion of a ferromagnetic core in the cardivascular system through magnetic gradients generated by an MRI system," *IEEE Trans. Biomed. Eng.*, vol. 53, no. 2, pp. 292–299, 2006.
[149] S. Martel, J. Mathieu, O. Felfoul, A. Chanu, E. Aboussouan, S. Tamaz, P. Pouponneau, L. Yahia, G. Beaudoin, G. Soulez, and M. Mankiewicz, "Automatic navigation of an untethered device in the artery of a living animal using a conventional clinical magnetic resonance imaging system," *Appl. Phys. Lett.*, vol. 90, no. 11, pp. 114105–1–114105–3, 2007.
[150] K. Belharet, D. Folio, and A. Ferreira, "MRI-based microrobotic system for the propulsion and navigation of ferromagnetic microcapsules," *Minimal. Invas. Ther. Allied Technol.*, vol. 19, no. 3, pp. 157–169, 2010.
[151] L. Arcese, M. Fruchard, and A. Ferreira, "Nonlinear modeling and robust controller-observer for a magnetic microrobot in a fluidic environment using MRI gradients," in *Proc. IEEE/RSJ Int. Conf. Intelligent Robots and Systems*, 2009, pp. 534–539.
[152] P. Pouponneau, J. C. Leroux, G. Soulez, L. Gaboury, and S. Martel, "Co-encapsulation of magnetic nanoparticles and doxorubicin into biodegradable microcarriers for deep tissue targeting by vascular MRI navigation," *Biomaterials*, vol. 32, no. 13, pp. 3481–3486, 2011.
[153] S. Martel, O. Felfoul, and M. Mohammadi, "Flagellated bacterial nanorobots for medical interventions in the human body," in *Proc. 2nd IEEE RAS and EMBS Int. Conf. Biomedical Robotics and Biomechatronics*, 2008, pp. 264–269.
[154] A. Luciani, C. Wilhelm, P. Bruneval, P. Cunin, G. Autret, A. Rahmouni, O. Clement, and F. Gazeau, "Magnetic targeting of iron-oxide-labeled fluorescent hepatoma cells to the liver," *Eur. Radiol.*, vol. 19, no. 5, pp. 1087–1096, 2009.
[155] J. Riegler, J. A. Wells, P. G. Kyrtatos, A. N. Price, Q. A. Pankhurst, and M. F. Lythgoe, "Targeted magnetic delivery and tracking of cells using a magnetic resonance imaging system," *Biomaterials*, vol. 31, no. 20, pp. 5366–5371, 2010.
[156] J. Dobson, C. Lewis, and H. Byrne, "Targeted therapy," U.S. Patent 12/293452, 2007.
[157] M. Muthana, S. D. Scott, N. Farrow, F. Morrow, C. Murdoch, S. Grubb, N. Brown, J. Dobson, and C. E. Lewis, "A novel magnetic approach to enhance the efficacy of cell-based gene therapies," *Gene Ther.*, vol. 15, no. 12, pp. 902–910, 2008.
[158] P. Pouponneau, J. C. Leroux, and S. Martel, "Magnetic nanoparticles encapsulated into biodegradable microparticles steered with an upgraded magnetic resonance imaging system for tumor chemoembolization," *Biomaterials*, vol. 30, no. 31, pp. 6327–6332, 2009.
[159] N. Olamaei, F. Cheriet, G. Beaudoin, and S. Martel, "MRI visualization of a single 15 um navigable imaging agent and future microrobot," in *Proc. 2010 Annu. Int. Conf. IEEE Engineering in Medicine and Biology Society (EMBC)*, pp. 4355–4358.
[160] S. Martel, "Microrobotic navigable entities for magnetic resonance targeting," in *Proc. 2010 Annu. Int. Conf. IEEE Engineering in Medicine and Biology Society*, pp. 1942–1945.
[161] M. P. Kummer, J. J. Abbott, B. E. Kratochvil, R. Borer, A. Sengul, and B. J. Nelson, "OctoMag: An electromagnetic system for 5-DOF wireless micromanipulation," *IEEE Trans. Robot.* , vol. 26, pp. 1006–1017, Dec. 2010.
[162] L. Arcese, A. Cherry, M. Fruchard, and A. Ferreira, "Dynamic behavior investigation for trajectory control of a microrobot in blood vessels," in *Proc. 2010 IEEE/RSJ Int. Conf. Intelligent Robots and Systems*, pp. 5774–5779.
[163] K. Belharet, D. Folio, and A. Ferreira, "Three-dimensional controlled motion of a microrobot using magnetic gradients," *Adv. Robot.*, vol. 25, no. 8, pp. 1069–1083, 2011.
[164] K. Schulze, A. Koch, B. Schopf, A. Petri, B. Steitz, M. Chastellain, M. Hofmann, H. Hofmann, and B. Von Rechenberg, "Intraarticular application of superparamagnetic nanoparticles and their uptake by synovial membrane—An experimental study in sheep," *J. Magn. Magn. Mater.*, vol. 293, no. 1, pp. 419–432, 2005.
[165] S. C. Goodwin, C. A. Bittner, C. L. Peterson, and G. Wong, "Single-dose toxicity study of hepatic intra-arterial infusion of doxorubicin coupled to a novel magnetically targeted drug carrier," *Toxicologic. Sci.*, vol. 60, no. 1, pp. 177–183, 2001.
[166] C. Alexiou, R. Jurgons, C. Seliger, S. Kolb, B. Heubeck, and H. Iro, "Distribution of mitoxantrone after magnetic drug targeting: Fluorescence

microscopic investigations on VX2 squamous cell carcinoma cells," *Int. J. Res. Phys. Chem. Chem. Phys.*, vol. 220, no. 2, pp. 235–240, 2006.
[167] C. Alexiou, W. Arnold, R. J. Klein, F. G. Parak, P. Hulin, C. Bergemann, W. Erhardt, S. Wagenpfeil, and A. S. Lubbe, "Locoregional cancer treatment with magnetic drug targeting," *Cancer Res.*, vol. 60, no. 23, pp. 6641–6648, 2000.
[168] C. Alexiou, R. Jurgons, R. Schmid, A. Hilpert, C. Bergemann, F. Parak, and H. Iro, "In vitro and in vivo investigations of targeted chemotherapy with magnetic nanoparticles," *J. Magn. Magn. Mater.*, vol. 293, no. 1, pp. 389–393, 2005.
[169] S. K. Pulfer and J. M. Gallo, "Enhanced brain tumor selectivity of cationic magnetic polysaccharide microspheres," *J. Drug Target.*, vol. 6, no. 3, pp. 215–227, 1998.
[170] S. K. Pulfer, S. L. Ciccotto, and J. M. Gallo, "Distribution of small magnetic particles in brain tumor-bearing rats," *J. Neuro-Oncol.*, vol. 41, no. 2, pp. 99–105, 1999.
[171] R. Tietze, R. Jurgons, S. Lyer, E. Schreiber, F. Wiekhorst, D. Eberbeck, H. Richter, U. Steinhoff, L. Trahms, and C. Alexiou, "Quantification of drug-loaded magnetic nanoparticles in rabbit liver and tumor after in vivo administration," *J. Magn. Magn. Mater.*, vol. 321, pp. 1465–1468, May 2009.
[172] O. Mykhaylyk, A. Cherchenko, A. Ilkin, N. Dudchenko, V. Ruditsa, M. Novoseletz, and Y. Zozulya, "Glial brain tumor targeting of magnetite nanoparticles in rats," *J. Magn. Magn. Mater.*, vol. 225, no. 1–2, pp. 241–247, 2001.
[173] Y. Sun, Z. Chen, X. Yang, P. Huang, X. Zhou, and X. Du, "Magnetic chitosan nanoparticles as a drug delivery system for targeting photodynamic therapy," *Nanotechnology*, vol. 20, no. 13, pp. 135102–135109, 2009.
[174] S. L. Raut, B. Kirthivasan, M. M. Bommana, E. Squillante, and M. Sadoqi, "The formulation, characterization and in vivo evaluation of a magnetic carrier for brain delivery of NIR dye," *Nanotechnology*, vol. 21, no. 39, pp. 395102–395111, 2010.
[175] B. Chertok, B. A. Moffat, A. E. David, F. Yu, C. Bergemann, B. D. Ross, and V. C. Yang, "Iron oxide nanoparticles as a drug delivery vehicle for MRI monitored magnetic targeting of brain tumors," *Biomaterials*, vol. 29, no. 4, pp. 487–496, 2008.
[176] B. Chertok, A. E. David, and V. C. Yang, "Delivery of functional proteins to brain tumor using MRI-monitored, magnetically-targeted nanoparticles," *J. Control. Release*, vol. 132, no. 3, pp. e61–e62, 2008.
[177] H. L. Liu, M. Y. Hua, H. W. Yang, C. Y. Huang, P. C. Chu, J. S. Wu, and I. Tseng, "Magnetic resonance monitoring of focused ultrasound/magnetic nanoparticle targeting delivery of therapeutic agents to the brain," *Proc. Nat. Acad. Sci.*, vol. 107, no. 34, pp. 15205–15210, 2010.
[178] Z. G. Forbes, B. B. Yellen, K. A. Barbee, and G. Friedman, "An approach to targeted drug delivery based on uniform magnetic fields," *IEEE Trans. Magn.*, vol. 39, no. 5, pp. 3372–3377, 2003.
[179] B. B. Yellen, Z. G. Forbes, K. A. Barbee, and G. Friedman, "Model of an approach to targeted drug delivery based on uniform magnetic fields," in *Proc. IEEE Int. Magnetics Conf.*, 2003, pp. EC–06.
[180] B. B. Yellen, Z. G. Forbes, D. S. Halverson, G. Fridman, K. A. Barbee, M. Chorny, R. Levy, and G. Friedman, "Targeted drug delivery to magnetic implants for therapeutic applications," *J. Magn. Magn. Mater.*, vol. 293, no. 1, pp. 647–654, 2005.
[181] B. Polyak, I. Fishbein, M. Chorny, I. Alferiev, D. Williams, B. Yellen, G. Friedman, and R. J. Levy, "High field gradient targeting of magnetic nanoparticle-loaded endothelial cells to the surfaces of steel stents," *Proc. Nat. Acad. Sci.*, vol. 105, no. 2, pp. 698–703, 2008.
[182] M. O. Aviles, A. D. Ebner, and J. A. Ritter, "Implant assisted-magnetic drug targeting: Comparison of in vitro experiments with theory," *J. Magn. Magn. Mater.*, vol. 320, no. 21, pp. 2704–2713, 2008.
[183] G. H. Iacoba, O. Rotariub, N. J. Strachanband, and U. O. Hafelic, "Magnetizable needles and wires-modeling: An efficient way to target magnetic microspheres in vivo," *Biorheology*, vol. 41, pp. 599–612, 2004.
[184] M. E. Hayden and U. O. Hafeli, "'Magnetic bandages' for targeted delivery of therapeutic agents," *J. Phys.: Condens. Matter*, vol. 18, no. 38, pp. S2877–S2891, 2006.
[185] U. O. Hafeli, K. Gilmour, A. Zhou, S. Lee, and M. E. Hayden, "Modeling of magnetic bandages for drug targeting: Button vs. Halbach arrays," *J. Magn. Magn. Mater.*, vol. 311, no. 1, pp. 323–329, 2007.
[186] A. J. Rosengart, M. D. Kaminski, H. T. Chen, P. L. Caviness, A. D. Ebner, and J. A. Ritter, "Magnetizable implants and functionalized magnetic carriers: A novel approach for noninvasive yet targeted drug delivery," *J. Magn. Magn. Mater.*, vol. 293, no. 1, pp. 633–638, 2005.
[187] Z. G. Forbes, B. B. Yellen, D. S. Halverson, G. Fridman, K. A. Barbee, and G. Friedman, "Validation of high gradient magnetic field based drug delivery to magnetizable implants under flow," *IEEE Trans. Biomed. Eng.*, vol. 55, no. 2. pt. 1, pp. 643–649, 2008.
[188] P. J. Cregg, K. Murphy, and A. Mardinoglu, "Calculation of nanoparticle capture efficiency in magnetic drug targeting," *J. Magn. Magn. Mater.*, vol. 320, no. 23, pp. 3272–3275, 2008.
[189] T. Kubo, T. Sugita, S. Shimose, Y. Nitta, Y. Ikuta, and T. Murakami, "Targeted delivery of anticancer drugs with intravenously administered magnetic liposomes in osteosarcoma-bearing hamsters.," *Int. J. Oncol.*, vol. 17, no. 2, pp. 309–315, 2000.
[190] Z. G. Forbes, B. B. Yellen, K. A. Barbee, and G. Friedman, "Magnetically controllable delivery system for therapeutic agents," U.S. Patent Application 20060041182, Aug. 2005.
[191] B. Shapiro, K. Dormer, and I. B. Rutel, "A two-magnet system to push therapeutic nanoparticles," in *Proc. American Institute of Physics, Conf. Series*, *Rostock*, Germany, May 2010, vol. 1311, pp. 77–88.
[192] A. Komaee, R. Lee, A. Nacev, R. Probst, A. Sarwar, I. Rutel, D. Depireux, K. Dormer, and B. Shapiro, "Putting therapeutic nanoparticles where they need to go by magnet systems design and control," in *Magnetic Nanoparticles: From Fabrication to Biomedical and Clinical Applications*, N. K. Thanh, Ed. Boca Raton, FL: CRC Press, Apr. 2011.
[193] R. Probst, J. Lin, A. Komaee, A. Nacev, Z. Cummins, and B. Shapiro, "Planar steering of a single ferrofluid drop by optimal minimum power dynamic feedback control of four electromagnets at a distance," *J. Magn. Magn. Mater.*, vol. 323, no. 7, pp. 885–896, 2011.
[194] R. Ganguly, A. P. Gaind, S. Sen, and I. K. Puri, "Analyzing ferrofluid transport for magnetic drug targeting," *J. Magn. Magn. Mater.*, vol. 289, no. 11, pp. 331–334, 2005.
[195] A. Komaee and B. Shapiro, "Magnetic steering of a distributed ferrofluid towards a deep target with minimal spreading," in *Proc. 50th IEEE Conf. Decision and Control and European Control Conference*, Orlando, FL, Dec. 2011, pp. 7950–7955.
[196] R. P. Feynman, R. B. Leighton, and M. Sands, *The Feynman Lectures on Physics*. Reading, MA: Addison-Wesley, 1964.
[197] J. F. Schenck, "The role of magnetic susceptibility in magnetic resonance imaging," *Med. Phys.*, vol. 23, no. 6, pp. 815–850, 1996.
[198] A. Vignaud, X. Maitre, G. Guillot, E. Durand, L. de Rochefort, P. Robert, V. Vives, R. Santus, and L. Darrasse, "Magnetic susceptibility matching at the air-tissue interface in rat lung by using a superparamagnetic intravascular contrast agent: Influence on transverse relaxation time of hyperpolarized helium-3," *Magn. Reson. Med.*, vol. 54, no. 1, pp. 28–33, 2005.
[199] V. Skumryev, H. J. Blythe, J. Cullen, and J. M. D. Coey, "AC susceptibility of a magnetite crystal," *J. Magn. Magn. Mater.*, vol. 196, no. 1, pp. 515–517, 1999.
[200] Y. S. Kang, S. Risbud, J. F. Rabolt, and P. Stroeve, "Synthesis and characterization of nanometer-size Fe_3O_4 and y-Fe_2O_3 particles," *Chem. Mater.*, vol. 8, no. 9, pp. 2209–2211, 1996.
[201] D. A. Fleisch, *A Student's Guide to Maxwell's Equations*. Cambridge, U.K.; New York: Cambridge Univ. Press, 2008.
[202] G. H. Iacob, O. Rotariu, and H. Chiriac, "A possibility for local targeting of magnetic carriers," *J. Optoelectron. Adv. Mater.*, vol. 6, no. 2, pp. 713–717, 2004.
[203] C. S. Lee, H. Lee, and R. M. Westervelt, "Microelectromagnets for the control of magnetic nanoparticles," *Appl. Phys. Lett.*, vol. 79, no. 20, pp. 3308–3310, 2001.
[204] C. I. Mikkelsen, "Magnetic separation and hydrodynamic interactions in microfluidic systems," Ph.D. dissertation, Tech. Univ. Denmark, 2005.
[205] C. Thirion, W. Wernsdorfer, and D. Mailly, "Switching of magnetization by non-linear resonance studied in single nanoparticles," vol. 2, no. 8, pp. 524–527, 2003.
[206] E. P. Furlani and K. C. Ng, "Analytical model of magnetic nanoparticle transport and capture in the microvasculature," *Phys. Rev. E*, vol. 73, no. 6, pp. 61919–61928, 2006.
[207] O. Rotariu and N. J. C. Strachan, "Modeling magnetic carrier particle targeting in the tumor microvasculature for cancer treatment," *J. Magn. Magn. Mater.*, vol. 293, no. 1, pp. 639–646, 2005.
[208] M. V. Goycoolea and L. Lundman, "Round window membrane. structure function and permeability: A review," *Microsc. Res. Tech.*, vol. 36, no. 3, pp. 201–211, 1997.
[209] E. M. Renkin, "Filtration, diffusion, and molecular sieving through porous cellulose membranes," *J. General Physiol.*, vol. 38, no. 2, pp. 225–243, 1954.

[210] J. Weizenecker, B. Gleich, J. Rahmer, H. Dahnke, and J. Borgert, "Three-dimensional real-time in vivo magnetic particle imaging," *Phys. Med. Biol.*, vol. 54, no. 5, pp. L1–L10, 2009.
[211] W. F. Ganong, *Review of Medical Physiology*, 20th ed. New York: Lange, 2001.
[212] E. E. Swan, M. J. Mescher, W. F. Sewell, S. L. Tao, and J. T. Borenstein, "Inner ear drug delivery for auditory applications," *Adv. Drug Deliv. Rev.*, vol. 60, no. 15, pp. 1583–1599, 2008.
[213] M. D. Seidman, B. G. Shivapuja, and W. S. Quirk, "The protective effects of allopurinol and superoxide dismutase on noise-induced cochlear damage," *Otolaryngol. Head Neck Surg.*, vol. 109, no. 6, pp. 1052–1056, 1993.
[214] R. W. Baloh, V. Honrubia, and K. Jacobson, "Benign positional vertigo," *Neurology*, vol. 37, no. 3, pp. 371–378, 1987.
[215] D. McFadden, *Tinnitus: Facts, Theories, and Treatments.* Washington D.C.: National Academies Press, 1982.
[216] J. P. Harris and A. F. Ryan, "Fundamental immune mechanisms of the brain and inner ear," *Otolaryngol. Head Neck Surg.*, vol. 112, no. 6, pp. 639–653, 1995.
[217] R. D. Kopke, R. A. Wassel, F. Mondalek, B. Grady, K. Chen, J. Liu, D. Gibson, and K. J. Dormer, "Magnetic nanoparticles: Inner ear targeted molecule delivery and middle ear implant," *Audiol. Neurotol.*, vol. 11, no. 2, pp. 123–133, 2008.
[218] F. G. Shellock, *Magnetic Resonance Procedures: Health Effects and Safety.* New York: Taylor & Francis, 2001.
[219] H. Silverstein, J. E. Isaacson, M. J. Olds, P. T. Rowan, and S. Rosenberg, "Dexamethasone inner ear perfusion for the treatment of meniere's disease: A prospective, randomized, double-blind, crossover trial," *Otology Neurotol.*, vol. 19, no. 2, pp. 196–201, 1998.
[220] L. J. Hood, *Clinical Applications of the Auditory Brainstem Response.* San Diego, CA: Singular Pub. Group, 1998.
[221] O. Tredan, C. M. Galmarini, K. Patel, and I. F. Tannock, "Drug resistance and the solid tumor microenvironment," *J. Nat. Cancer Inst.*, vol. 99, pp. 1441–1454, Oct. 2007.
[222] C. A. Desoer and E. S. Kuh, *Basic Circuit Theory*, New York: McGraw-Hill, 1969, ch. 1–10.
[223] A. Ashkin, "History of optical trapping and manipulation of small-neutral particle, atoms, and molecules," *IEEE J. Select. Topics Quantum Electron.*, vol. 6, no. 6, pp. 841–856, 2000.
[224] C. Ropp, R. Probst, Z. Cummins, R. Kumar, A. J. Bergland, S. R. Raghavan, E. Waks, and B. Shapiro, "Manipulating quantum dots to nanometer precision by control of flow," *Nano Letters*, vol. 10, no. 7, pp. 2525–2530, 2010.
[225] S. G. Kim and S. Ogawa, "Insights into new techniques for high resolution functional MRI," *Curr. Opin. Neurobiol.*, vol. 12, no. 5, pp. 607–615, 2002.
[226] J. W. Barry, J. J. Bookstein, and J. F. Alksne, "Ferromagnetic embolization. experimental evaluation," *Radiology*, vol. 138, no. 2, pp. 341–349, 1981.
[227] P. Moroz, S. K. Jones, J. Winter, and B. N. Gray, "Targeting liver tumors with hyperthermia: ferromagnetic embolization in a rabbit liver tumor model," *J. Surg. Oncol.*, vol. 78, no. 1, pp. 22–29, 2001.
[228] U. Talit, S. Braun, H. Halkin, B. Shargorodsky, and S. Laniado, "Pharmacokinetic differences between peripheral and central drug administration during cardiopulmonary resuscitation," *J. Amer. College Cardiol.*, vol. 6, no. 5, pp. 1073–1077, 1985.
[229] S. M. Moghimi, A. C. Hunter, and J. C. Murray, "Long-circulating and target-specific nanoparticles: Theory to practice," *Pharmacol. Rev.*, vol. 53, no. 2, pp. 283–318, 2001.
[230] L. J. Nugent and R. K. Jain, "Extravascular diffusion in normal and neoplastic tissues," *Cancer Res.*, vol. 44, no. 1, pp. 238–244, 1984.
[231] R. K. Jain, "Determinants of tumor blood flow: A review," *Cancer Res.*, vol. 48, no. 10, pp. 2641–2658, 1988.
[232] R. F. Probstein, *Physicochemical Hydrodynamics: An Introduction*, 2nd ed. New York: Wiley, 1994.
[233] M. A. Clauss and R. K. Jain, "Interstitial transport of rabbit and sheep antibodies in normal and neoplastic tissues," *Cancer Res.*, vol. 50, no. 12, pp. 3487–3492, 1990.
[234] R. L. Panton, *Incompressible Flow*, 2nd ed. New York: Wiley, 1996.
[235] F. P. Incropera, *Fundamentals of Heat and Mass Transfer.* Hoboken, NJ: Wiley, 2007.
[236] R. M. Berne and M. N. Levy, *Cardiovascular Physiology.* St. Louis, MO: Mosby, 1967.
[237] K. J. Widder, A. E. Senyei, and D. F. Ranney, "Magnetically responsive microspheres and other carriers for the biophysical targeting of antitumor agents," *Adv. Pharmacol. Chemother.*, New York, NY: Academic Press, vol. 16, pp. 213–271, 1979.
[238] A. Lubbe, "Treatment of cancer patients," private communication, 2006.
[239] B. Alberts, A. Johnson, J. Lewis, M. Raff, K. Roberts, and P. Walter, *Molecular Biology of the Cell*, 5th ed. New York, NY: Garland Science, 2008.
[240] Y. Rojanasakul, L. Y. Wang, M. Bhat, D. D. Glover, C. J. Malanga, and J. K. Ma, "The transport barrier of epithelia: A comparative study on membrane permeability and charge selectivity in the rabbit," *Pharmaceut. Res.*, vol. 9, no. 8, pp. 1029–1034, 1992.
[241] J. S. Patton and R. M. Platz, "Pulmonary delivery of peptides and proteins for systemic action," *Adv. Drug Deliv. Rev.*, vol. 8, no. 2–3, pp. 179–196, 1992.
[242] G. Antoch, F. M. Vogt, L. S. Freudenberg, F. Nazaradeh, S. C. Goehde, J. Barkhausen, G. Dahmen, A. Bockisch, J. F. Debatin, and S. G. Ruehm, "Whole-body dual-modality PET/CT and whole-body MRI for tumor staging in oncology," *JAMA*, vol. 290, no. 24, pp. 3199–3206, 2003.
[243] H. Nomori, K. Watanabe, T. Ohtsuka, T. Naruke, K. Suemasu, and K. Uno, "The size of metastatic foci and lymph nodes yielding false-negative and false-positive lymph node staging with positron emission tomography in patients with lung cancer," *J. Thorac. Cardiovasc. Surg.*, vol. 127, no. 4, pp. 1087–1092, 2004.
[244] A. L. Schechter, D. F. Stern, L. Vaidyanathan, S. J. Decker, J. A. Drebin, M. I. Greene, and R. A. Weinberg, "The neu oncogene: An erb-B-related gene encoding a 185,000-Mr tumour antigen," *Nature*, vol. 312, no. 6, pp. 513–516, 1984.
[245] C. C. Badger, C. Anasetti, J. Davis, and I. D. Bernstein, "Treatment of malignancy with unmodified antibody.," *Pathol. Immunopathol. Res.*, vol. 6, no. 5–6, pp. 419–434, 1987.
[246] M. A. Olayioye, R. M. Neve, H. A. Lane, and N. E. Hynes, "New EMBO members' review: The ErbB signaling network: Receptor heterodimerization in development and cancer," *EMBO J.*, vol. 19, no. 13, pp. 3159–3167, 2000.
[247] J. Baselga, D. Tripathy, J. Mendelsohn, S. Baughman, C. C. Benz, L. Dantis, N. T. Sklarin, A. D. Seidman, C. A. Hudis, and J. Moore, "Phase II study of weekly intravenous recombinant humanized anti-p185HER2 monoclonal antibody in patients with HER2/neu-overexpressing metastatic breast cancer," *J. Clin. Oncol.*, vol. 14, no. 3, pp. 737–744, 1996.
[248] M. A. Cobleigh, C. L. Vogel, D. Tripathy, N. J. Robert, S. Scholl, L. Fehrenbacher, J. M. Wolter, V. Paton, S. Shak, and G. Lieberman, "Multinational study of the efficacy and safety of humanized anti-HER2 monoclonal antibody in women who have HER2-overexpressing metastatic breast cancer that has progressed after chemotherapy for metastatic disease," *J. Clin. Oncol.*, vol. 17, no. 9, p. 2639, 1999.
[249] J. M. Reichert, C. J. Rosensweig, L. B. Faden, and M. C. Dewitz, "Monoclonal antibody successes in the clinic," *Nat. Biotechnol.*, vol. 23, no. 9, pp. 1073–1078, 2005.
[250] P. R. Pohlmann, I. A. Mayer, and R. Mernaugh, "Resistance to trastuzumab in breast cancer," *Clin. Cancer Res.*, vol. 15, no. 24, pp. 7479–7491, 2009.
[251] R. Nahta and F. J. Esteva, "HER-2-targeted therapy," *Clin. Cancer Res.*, vol. 9, no. 14, pp. 5078–5084, 2003.
[252] J. Christiansen and A. K. Rajasekaran, "Biological impediments to monoclonal antibody-based cancer immunotherapy," *Mol. Cancer Therapeut.*, vol. 3, no. 11, pp. 1493–1501, 2004.
[253] M. Campoli, R. Ferris, S. Ferrone, and X. Wang, "Immunotherapy of malignant disease with tumor antigen-specific monoclonal antibodies," *Clin. Cancer Res.*, vol. 16, no. 1, pp. 11–20, 2010.
[254] H. Sakahara, T. Saga, H. Onodera, Z. Yao, Y. Nakamoto, M. Zhang, N. Sato, H. Nakada, I. Yamashina, and K. Endo, "Anti murine antibody response to mouse monoclonal antibodies in cancer patients," *Cancer Sci.*, vol. 88, no. 9, pp. 895–899, 1997.
[255] M. B. Khazaeli, R. M. Conry, and A. F. LoBuglio, "Human immune response to monoclonal antibodies," *J. Immunother.*, vol. 15, no. 1, pp. 42–52, 1994.
[256] P. Carter, L. Presta, C. M. Gorman, J. B. Ridgway, D. Henner, W. L. Wong, A. M. Rowland, C. Kotts, M. E. Carver, and H. M. Shepard, "Humanization of an anti-p185HER2 antibody for human cancer therapy," *Proc. Nat. Acad. Sci.*, vol. 89, no. 10, pp. 4285–4289, 1992.
[257] B. M. Fendly, M. Winget, R. M. Hudziak, M. T. Lipari, M. A. Napier, and A. Ullrich, "Characterization of murine monoclonal antibodies reactive to either the human epidermal growth factor receptor or HER2/neu gene product," *Cancer Res.*, vol. 50, no. 5, pp. 1550–1558, 1990.

[258] P. Carter, "Improving the efficacy of antibody-based cancer therapies," *Nat. Rev. Cancer*, vol. 1, no. 2, pp. 118–129, 2001.
[259] M. Little, S. M. Kipriyanov, F. Le Gall, and G. Moldenhauer, "Of mice and men: Hybridoma and recombinant antibodies," *Immunol. Today*, vol. 21, no. 8, pp. 364–370, 2000.
[260] L. A. Khawli, G. K. Miller, and A. L. Epstein, "Effect of seven new vasoactive immunoconjugates on the enhancement of monoclonal antibody uptake in tumors," *Cancer*, vol. 73, no. S3, pp. 824–831, 1994.
[261] D. M. Goldenberg, S. M. Larson, R. A. Reisfeld, and J. Schlom, "Targeting cancer with radiolabeled antibodies," *Immunol. Today*, vol. 16, no. 6, pp. 261–264, 1995.
[262] A. A. Epenetos, D. Snook, H. Durbin, P. M. Johnson, and J. Taylor-Papadimitriou, "Limitations of radiolabeled monoclonal antibodies for localization of human neoplasms," *Cancer Res.*, vol. 46, no. 6, pp. 3183–3191, 1986.
[263] U. S. FDA. (2011). U.S. food and drug administration fundamentals. [Online]. Available: http://www.fda.gov/AboutFDA/Transparency/Basics/ucm192695.htm
[264] U. S. FDA, "Design control guidance for medical device manufacturers," Mar. 11, 1997, p. 5.
[265] A. F. Chambers, A. C. Groom, and I. C. MacDonald, "Dissemination and growth of cancer cells in metastatic sites," *Nat. Rev. Cancer*, vol. 2, no. 8, pp. 563–571, 2002.
[266] K. Marusina, "Accelerator MS is a powerful new tool," *Genet. Eng. Biotechnol. News*, vol. 27, Sept. 2007.
[267] O. Pagani, E. Senkus, W. Wood, M. Colleoni, T. Cufer, S. Kyriakides, A. Costa, E. P. Winer, and F. Cardoso, "International guidelines for management of metastatic breast cancer: Can metastatic breast cancer be cured?," *JNCI J. Nat. Cancer Inst.*, vol. 102, no. 7, pp. 456–463, 2010.
[268] R. K. Jain, "Normalization of tumor vasculature: An emerging concept in antiangiogenic therapy," *Science*, vol. 307, no. 5706, pp. 58–62, 2005.
[269] K. P. Pruessmann, M. Weiger, M. B. Scheidegger, and P. Boesiger, "SENSE: Sensitivity encoding for fast MRI," *Magn. Reson. Med.*, vol. 42, no. 5, pp. 952–962, 1999.
[270] M. M. Ter-Pogossian, M. E. Phelps, E. J. Hoffman, and N. A. Mullani, "Positron-emission transaxial tomograph for nuclear imaging (PETT)," *Radiology*, vol. 114, no. 1, pp. 89–98, 1975.
[271] F. Sanchez, J. M. Benlloch, B. Escat, N. Pavon, E. Porras, D. Kadi-Hanifi, J. A. Ruiz, F. J. Mora, and A. Sebastia, "Design and tests of a portable mini gamma camera," *Med. Phys.*, vol. 31, no. 6, pp. 1384–1397, 2004.
[272] F. J. Beekman and G. A. de Vree, "Photon-counting versus an integrating CCD-based gamma camera: Important consequences for spatial resolution," *Phys. Med. Biol.*, vol. 50, no. 12, pp. 109–119, 2005.
[273] S. Earnshaw, "On the nature of the molecular forces which regulate the constitution of the luminiferous ether," *Trans. Cambridge Philos. Soc.*, vol. 7, no. 1, pp. 97–112, 1842.
[274] I. Hilger, R. Hergt, and W. A. Kaiser, "Use of magnetic nanoparticle heating in the treatment of breast cancer," *IEE Proc. Nanobiotechnol.*, vol. 152, no. 1, pp. 33–39, 2005.
[275] C. L. Dennis, A. J. Jackson, J. A. Borchers, P. J. Hoopes, R. Strawbridge, A. R. Foreman, J. Van Lierop, C. Gruttner, and R. Ivkov, "Nearly complete regression of tumors via collective behavior of magnetic nanoparticles in hyperthermia," *Nanotechnology*, vol. 20, no. 35, p. 395103, 2009.
[276] E. S. Handy, R. Ivkov, D. Ellis-Busby, and A. Foreman, "Thermotherapy via targeted delivery of nanoscale magnetic particles," No. 10/176,950, 2006.
[277] P. M. Pardalos, "Global optimization algorithms for linearly constrained indefinite quadratic problems," *Comput. Math. Applicat.*, vol. 21, no. 6–7, pp. 87–97, 1991.
[278] R. Horst and P. M. Pardalos, *Handbook of Global Optimization*, vol. 1. Norwell, MA: Kluwer, 1995.
[279] D. Price, I. Delakis, C. Renaud, and R. Dickinson. (2008). MRI scanners: A buyer's guide [Online]. *The Buyer's Guide to Respiratory Care Products*. Available: http://www.ersbuyersguide.org/
[280] W. R. Adey, "Biological effects of electromagnetic fields," *J. Cell. Biochem.*, vol. 51, no. 4, pp. 410–410, 1993.
[281] G. A. Mesyats, *Pulsed Power*. New York: Springer Science+ Business Media, 2005.
[282] S. K. Imam, "Molecular nuclear imaging: The radiopharmaceuticals (review)," *Cancer Biother. Radiopharmaceut.*, vol. 20, no. 2, pp. 163–172, 2005.
[283] E. C. Frey, Z. W. Ju, and B. M. W. Tsui, "A fast projector-backprojector pair modeling the asymmetric, spatially varying scatter response function for scatter compensation in SPECT imaging," *IEEE Trans. Nuclear Sci.*, vol. 40, no. 4, pp. 1192–1197, 1993.
[284] S. Staelens, T. de Wit, and F. Beekman, "Fast hybrid SPECT simulation including efficient septal penetration modelling (SP-PSF)," *Phys. Med. Biol.*, vol. 52, no. 11, pp. 3027–3043, 2007.
[285] H. Zaidi, "Scatter modelling and correction strategies in fully 3-D PET," *Nuclear Med. Commun.*, vol. 22, no. 11, pp. 1181–1184, 2001.
[286] I. R. Young, A. S. Hall, C. A. Pallis, G. M. Bydder, N. J. Legg, and R. E. Steiner, "Nuclear magnetic resonance imaging of the brain in multiple sclerosis," *Lancet*, vol. 318, no. 8255, pp. 1063–1066, 1981.
[287] B. H. Hasegawa, "The physics of medical X-ray imaging," Madison, WI: Medical Physics Pub. Co., 1990.
[288] S. Webb, *The Physics of Medical Imaging*. New York: Taylor & Francis, 1988.
[289] M. A. Hahn, A. K. Singh, P. Sharma, S. C. Brown, and B. M. Moudgil, "Nanoparticles as contrast agents for in-vivo bioimaging: Current status and future perspectives," *Anal. Bioanal. Chem.*, vol. 399, no. 1, pp. 1–25, 2010.
[290] O. Brunke, S. Odenbach, R. Jurgons, C. Alexiou, I. Hilger, and F. Beckmann, "Determination of the magnetic particle distribution in tumour tissue by means of X-ray tomography," *J. Phys. Condens. Matter*, vol. 18, no. 38, pp. S2903–S2917, 2006.
[291] D. L. Bailey, *Positron Emission Tomography: Basic Sciences*. Berlin: Springer-Verlag, 2005.
[292] E. L. Bradley, J. Cella, S. Majewski, V. Popov, J. Qian, M. S. Saha, M. F. Smith, A. G. Weisenberger, and R. E. Welsh, "A compact gamma camera for biological imaging," *IEEE Trans. Nuclear Sci.*, vol. 53, no. 1, pp. 59–65, 2006.
[293] J. A. Sorenson, M. E. Phelps, and S. R. Cherry, *Physics in Nuclear Medicine*. Orlando, FL: Grune & Stratton, 1987.
[294] A. S. Arbab, K. Koizumi, K. Toyama, and T. Araki, "Uptake of technetium-99m-tetrofosmin, technetium-99m-MIBI and thallium-201 in tumor cell lines," *J. Nuclear Med.*, vol. 37, no. 9, pp. 1551–1556, 1996.
[295] B. Caner, M. Kitapcl, M. Unlu, G. Erbengi, T. Calikolu, T. Gou, and C. Bekdik, "Technetium-99m-MIBI uptake in benign and malignant bone lesions: A comparative study with technetium-99m-MDP," *J. Nuclear Med.*, vol. 33, no. 3, pp. 319–324, 1992.
[296] M. Rodrigues, F. Chehne, W. Kalinowska, C. Zielinski, and H. Sinzinger, "Comparative 99m Tc-MIBI, 99m tc-tetrofosmin and 99m tc-furifosmin uptake in human soft tissue sarcoma cell lines," *Eur. J. Nuclear Med. Mol. Imag.*, vol. 27, no. 12, pp. 1839–1843, 2000.
[297] T. F. Massoud and S. S. Gambhir, "Molecular imaging in living subjects: Seeing fundamental biological processes in a new light," *Genes Dev.*, vol. 17, no. 5, pp. 545–580, 2003.
[298] P. Debbage and W. Jaschke, "Molecular imaging with nanoparticles: Giant roles for dwarf actors," *Histochem. Cell Biol.*, vol. 130, no. 5, pp. 845–875, 2008.
[299] P. H. Jarritt and P. D. Acton, "PET imaging using gamma camera systems: A review," *Nuclear Med. Commun.*, vol. 17, no. 9, pp. 758–766, 1996.
[300] T. K. Lewellen, R. S. Miyaoka, and W. L. Swan, "PET imaging using dual-headed gamma cameras: An update," *Nuclear Med. Commun.*, vol. 20, no. 1, pp. 5–12, 1999.
[301] J. T. Kuikka, A. Sohlberg, and M. Husso-Saastamoinen, "PET imaging using a triple-head gamma camera," *Clin. Physiol. Funct. Imag.*, vol. 22, no. 5, pp. 328–331, 2002.
[302] A. Leschhorn, J. P. Embs, and M. Lucke, "Magnetization of rotating ferrofluids: The effect of polydispersity," *J. Phys.: Condens. Matter*, vol. 18, no. 38, pp. S2633–S2642, 2006.
[303] R. Muller, R. Hergt, S. Dutz, M. Zeisberger, and W. Gawalek, "Nanocrystalline iron oxide and Ba ferrite particles in the superparamagnetism-ferromagnetism transition range with ferrofluid applications," *J. Phys.: Condens. Matter*, vol. 18, no. 38, pp. S2527–S2542, 2006.
[304] T. Neuberger, B. Schopf, H. Hofmann, M. Hofmann, and B. von Rechenberg, "Superparamagnetic nanoparticles for biomedical applications: Possibilities and limitations of a new drug delivery system," *J. Magn. Magn. Mater.*, vol. 293, no. 1, pp. 483–496, 2005.
[305] F. K. Wacker, K. Reither, W. Ebert, M. Wendt, J. S. Lewin, and K. J. Wolf, "MR image-guided endovascular procedures with the ultrasmall superparamagnetic iron oxide SH u 555 c as an intravascular contrast agent: Study in pigs," *Radiology*, vol. 226, no. 2, pp. 459–464, 2003.
[306] H. Benveniste and S. Blackband, "MR microscopy and high resolution small animal MRI: Applications in neuroscience research," *Progr. Neurobiol.*, vol. 67, pp. 393–420, Aug. 2002.